β DECAY AND ISOMERIC STUDIES OF PROTON RICH NUCLEI NEAR THE ENDPOINT OF THE RP-PROCESS

By

Ana Delia Becerril Reyes

A DISSERTATION

Submitted to
Michigan State University
in partial fulfillment of the requirements
for the degree of

DOCTOR OF PHILOSOPHY

Physics

2011

ABSTRACT

β DECAY AND ISOMERIC STUDIES OF PROTON RICH NUCLEI NEAR THE ENDPOINT OF THE RP-PROCESS

By

Ana Delia Becerril Reyes

Neutron-deficient nuclei in the vicinity of the $N = Z = 50$ doubly-magic shell closure were produced at the National Superconducting Cyclotron Laboratory to study their structure and their relevance in the astrophysical rp-process. The ^{100}Sn nucleus is the heaviest particle-stable $N = Z$ nucleus, and it is also thought to be doubly magic. Additionally, ^{100}Sn and its closest neighbors lie in the path of rp-process, therefore, the production and study of the decay properties of these nuclei are of great interest for the experimental and theoretical nuclear physics and astrophysics community. Previous attempts to produce these nuclei were hampered by large amounts of contaminants produced with higher abundances than those of the nuclides of interst. The Radio Frequency Fragment Separator was designed and built at the NSCL in order to purify rare neutron-deficient secondary beams. The implementation of this device has made a number of β-decay experiments feasible at the NSCL. The experiment described in this work (NSCL Experiment 07034) was the second one to utilize the RFFS to successfully determine β-decay half-lives, β-delay proton emission branching ratios and β-delayed gamma spectroscopy.

The nuclei of interest were produced at NSCL via fragmentation of a ^{112}Sn primary beam accelerated to 120 MeV/nucleon, impinging on a ^{9}Be target. The secondary beam was first selected by the A1900 Fragment Separator and purified further with the RFFS. The $N = Z$ nuclei ^{100}Sn, ^{98}In and ^{96}Cd were produced and their β decay was studied. The observed production cross sections of these nuclei are lower than predicted by factors of 10-30. Their β-decay half-lives were found to be $0.55^{+0.70}_{-0.31}$ s for

^{100}Sn, 0.66(40)s for an isomeric state in ^{98}In, and 47(13) ms for its ground state, and $1.03^{+0.24}_{-0.21}$s for ^{96}Cd. The experimental determination of the half-life of ^{96}Cd was of special interest as it was the last rp-process waiting point to be measured. The effect of the half-life of ^{96}Cd on the nuclear abundances produced by an rp-process and the origin of the light-p nucleus ^{96}Ru was explored.

Other exotic nuclei produced in Experiment 07034 include $^{102-101}$Sn, ^{100,99}In, ^{98,97}Cd, $^{96-94}$Ag, $^{94-92}$Pd, ^{92,91}Rh and ^{90,91}Ru. For the cases with sufficiently high statistics their β-decay half-lives were determined and compared with previous measurements and theoretical predictions. Several isomeric states were found and their decay modes analyzed. In particular, a new microsecond isomer decaying by a γ cascade was observed in ^{96}Ag for the first time and the level scheme of this nucleus is presented, together with the results of two shell-model calculations performed within the $(p_{1/2}g_{9/2})$ and $(p_{3/2}p_{1/2}f_{5/2}g_{9/2})$ model spaces, respectively. It was found that the shell model calculation with the larger model space reproduced level energies and isomeric decay half-lives reasonably well.

Para mi familia.

ACKNOWLEDGMENTS

as many other practical and impractical questions almost every day. I thank him for being a great friend and guide.

I want to acknowledge the help and guidance provided by everyone in the Nuclear Astrophysics group at the NSCL. Past and present members of the group that I am specially thankful to are Jorge Pereira for useful discussions, advise and an interesting sense of humor, Marcelo Del Santo, Sebastian George, Zach Meisel and Karl Smith. Two characters that (for me, at least) defined an era in the group are Alfredo Estrade and Giuseppe Lorusso. I am glad we had the chance to attend conferences and schools together, as well as delightful operas. I am glad we became friends and shared many good times.

I want to acknowledge the encouragement and support from Sean McDaniel throughout our years in grad school. For all the good and bad times shared, for all the late nights studying for the subject exams, for all the discussions about physics, life and non-sense that we had, for making sure I ate lunch most days: thank you Sean!

Many other grad students in the lab were also supportive, helpful and friendly, specially my office mates, who maintained a nice and quiet atmosphere at our workplace. Hui Wang was particularly good at keeping me sane and happy by listening to me every time I needed to talk, and also by keeping a good supply of cookies at hand.

I want to thank all the amazing people that I found in East Lansing and that made my life in grad school so happy. I have the fortune to say that these are so many people that I cannot list them all here, but there are a few ones that will actually read this page, and so I should make sure to write their names: thanks very much to my dinner club friends Kim, Erin, Carol, Neil and Catherine for wonderful dinners and great times. Thanks to Ileana Marquez for being so helpful, loving and caring, particularly when I arrived to East Lansing. Thanks to my family in Michigan: Zenaida, Edith, Cecilia, Itza and Lourdes. To Lupi specially for making me realize how hillarious it can be to discuss nuclear astrophysics with a social scientist. To Steve, thank you for

your support, patience and love. Thank you for having faith in me.

With all my heart I want to thank my family and friends in Mexico who always supported me, loved me and pushed me to work hard and get done (finally) with school. Thanks to Arturo Menchaca and Ruben Alfaro for guiding me through my first research projects. Special thanks also go to Claudia, Karin and Yox for always being there for me. To Vicky, Vale, Hugo, Aldo and Delia for believing in me, and loving me so much, thank you.

A mis padres y a mis hermanos les debo todo, y les dedico mi esfuerzo. Los amo. Muchisimas gracias!

Contents

List of Figures

List of Tables

Chapter 1

Introduction

The origin of the heavy elements and the nature of explosive events in the cosmos are two of the most exciting open questions in science. These are two closely related puzzles. The field of Nuclear Astrophysics is concerned with finding answers to these and other questions by taking a multidisciplinary approach to the problem: it brings together observational astronomers, nuclear experimenters and theorists to develop models of the various astrophysical scenarios based on reliable nuclear physics; and conversely, uses astrophysical observations to understand the behavior of nuclear matter at extremely high densities.

It is now understood that most elements up to iron are synthesized by fusion reactions in stars. When stars run out of nuclear fuel they eject their metal-enriched envelopes into the interstellar medium. Neutron capture processes create most of the heavy elements beyond iron. These processes occur during hydrostatic burning in massive stars and possibly in explosive events that provide temperature and densities high enough to induce nuclear reactions that would otherwise be unfeasible. The ashes of a variety of nucleosynthesis events enriches the interstellar medium with material of high metallicity (anything beyond H and He), thus providing material for new stars to form. Such nucleosynthetic cycling in our galaxy resulted in the abundance distribution currently observed in the solar system. Detailed understanding of the

nucleosynthesis of elements beyond iron is still far from complete. New observations of explosive events in the universe have reached unprecedented quality and they must be interpreted in terms of the underlying physics of the nuclear reactions responsible for the energy generation.

Many experimental programs at rare isotope facilities worldwide are currently dedicated to the production and study of the exotic nuclei that play key roles in the different astrophysical scenarios thought to contribute to the origin of the heavy elements. At the National Superconducting Cyclotron Laboratory (NSCL), the question of the creation of the heavy elements is addressed through experiments dedicated to investigate the nuclear structure, half-lives and masses of the relevant isotopes, as well as the nuclear reactions in which they participate.

The work presented here describes a β-decay experiment performed at the NSCL with a twofold motivation: one was to gather experimental data on the structure of neutron-deficient nuclei along the path of the astrophysical rapid proton capture process (rp-process). The aim of this chapter is to provide an overview of the astrophysics motivation of our study of heavy $N \approx Z$ nuclei. Of particular interest for us was the determination of the β-decay half-life of ^{96}Cd, a waiting point in the rp-process and a proposed progenitor of ^{96}Ru via β^+ decay.

β-decay spectroscopy measurements close to the proton drip-line are needed not only to determine the last unknown β-decay half-lives in the rp-process, but also to clarify the detailed structure of the decays. This is necessary to calculate corrections for the lifetimes of these nuclei in the astrophysical environment. For instance, isomeric states occurring along the process path may have a significant impact on the time scale and final abundances. If an isomer is populated in sufficient quantities it could create a non-thermal population of states, and therefore, their separate identities must be considered in nuclear reaction networks. A β-decaying spin-gap isomer with a half-life of 0.5 seconds was predicted in ^{96}Cd by Ogawa in [1]. Details on the shell model predictions for ^{96}Cd will be given in Chapter 2. It is important to realize

that if this isomeric state exists and if it is populated significantly in the fragmentation reaction of our experiment, then a mixed half-life from ground and isomeric states would be measured. Since ^{96}Cd β-decays into ^{96}Ag, we searched for isomeric states in this nucleus too, which could potentially also affect the production of $A = 96$ mass in the rp-process.

The second motivation for the present study was to gain understanding of the shell evolution close to the predicted doubly magic nucleus ^{100}Sn. An interesting phenomenon in this region of the chart of nuclides is the ocurrence of high-spin isomeric states, which exhibit various decay modes (e.g. β, β-delayed proton, γ). With over 20 different neutron-deficient species produced in in their ground and isomeric states in our experiment, various decay modes were observed and their half-lives were determined, ranging from a few hundred nanoseconds to several seconds. A brief theoretical framework on the nuclear structure in the region studied will be presented in Chapter 2.

Details of the experiment are provided in Chapter 3, together with a brief description of the devices utilized. Particular attention is given to the Radio Frequency Fragment Separator, a velocity filter that improved the purity of the rare isotope beam to a level adequate for decay studies. This device was built at the NSCL especifically to purify neutron-deficient beams that cannot be separated by the A1900 Fragment Separator alone.

In Chapter 4 a detailed description of the data analysis is presented, and the results are discussed in Chapter 5. Finally, the effect of our measurements on the abundances produced by an rp-process reaching the Sn region is explored by incorporating the experimental results into a reaction network calculation. This will be the subject of Chapter 6.

1.1   Origin of the light p-nuclei

Most of the nuclides heavier than iron are synthesized through a series of neutron captures and β^- decays in the so-called slow and rapid (s- and r-, respectively) neutron capture processes. Exotic neutron-rich nuclei are created through succcesive neutron captures, and stable isotopes are formed when the newly formed neutron-rich nucleus β^- decays. However, the stable isotopes on the proton-rich side of the valley of stability cannot be reached through such processes as they are shielded by more neutron-rich stable isotopes. These proton-rich nuclei are referred to as p-nuclei, of which ^{74}Se is the lightest and ^{196}Hg the heaviest [2]. The solar system abundances of the p-nuclei is one to three orders of magnitude lower than their more neutron-rich isotopes, and any model attempting to describe their synthesis must account for this fact. A long standing question in nuclear astrophysics has been the origin of the light p-nuclei ^{92}Mo, ^{94}Mo, ^{96}Ru, and ^{98}Ru (see Fig. 1.1) found in the solar system with rather large isotopic abundances of 14.84%, 9.25%, 5.52% and 1.88%, respectively [3, 4].

The p-nuclei can be made in nature, in principle, via the p-process, which consists of γ-induced photodisintegration of heavy nuclei previously created by neutron capture processes. The p-process is thought to occur in the shock front of Type II supernovae, or in the deflagration flame of a Type I supernova detonation [3, 4], or alternatively in pre-explosive or explosive O/Ne burning [2]. While the p-process can reproduce the synthesis of the majority of the proton rich stable isotopes found nature, it fails to account for the large abundances of nuclei in the $92 \leq A \leq 98$ mass range (e.g. [2, 4, 5]).

Another possible mechanism to create p-nuclei could be a series of proton captures on lighter nuclei. High Coulomb barriers would have to be overcome for the (p, γ) reactions to proceed on high Z nuclei, therefore, high temperature and density environments with a high proton flux are required. The rp-process in X-ray bursts was proposed as a possible source of the p-nuclei [5, 6]. This scenario provides the required
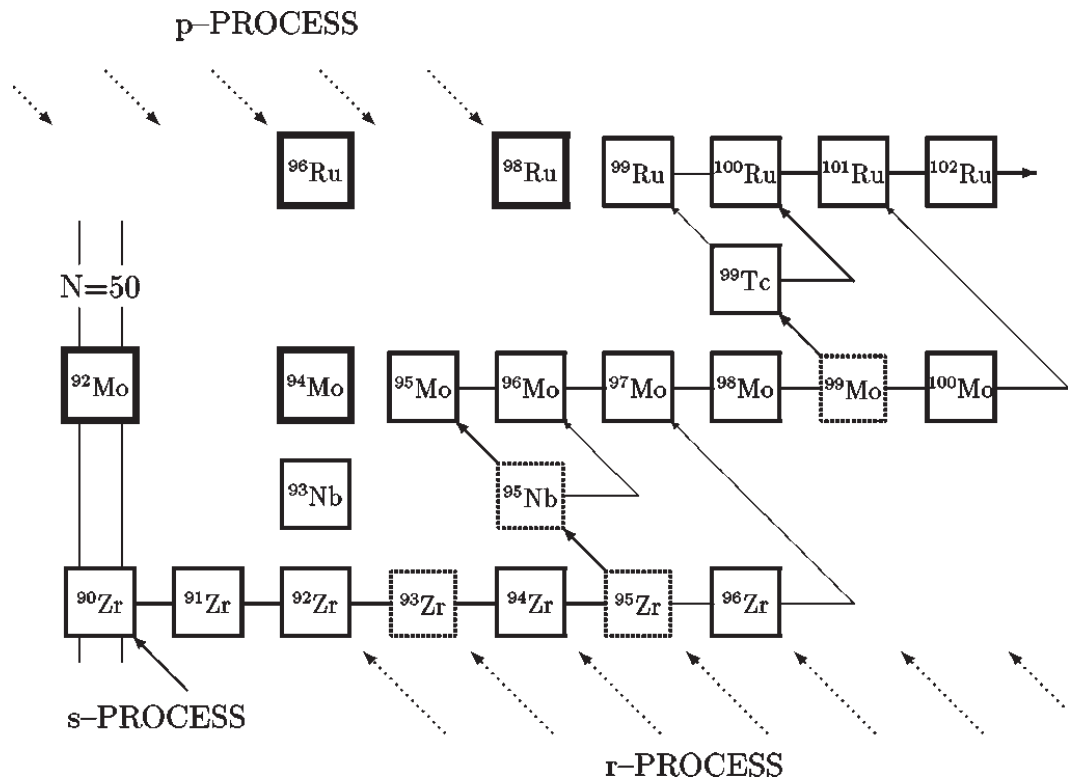
Figure 1.1: Section of the chart of nuclides indicating the light p-nuclei ^{92}Mo, ^{94}Mo, ^{96}Ru, and ^{98}Ru. These nuclei cannot be created through neutron capture nucleosynthesis mechanisms. Figure adapted from [3].

proton-rich environment, as well as the high temperature needed to compensate for Coulomb repulsion during proton captures. However, an argument against significant contribution of X-ray bursts to the synthesis of p-nuclides in the Mo-Ru region is the presence of live ^{92}Nb in the early solar system [7]. This nucleus cannot be produced by the rp-process because it is shielded against β^+ decay by ^{92}Mo, which is stable. Thus, ^{92}Nb must be produced by Type II supernovae. Based on Galatic Chemical Evolution models, Dauphas *et al.* concluded that if X-ray bursts produced most of the p-nuclides then the ^{92}Nb/^{92}Mo ratio in the interestellar medium would have been lowered by a factor of 10 relative to supernovae because X-ray bursts do not produce ^{92}Nb.

The so-called νp-process [8–10] may also contribute to the creation of light p-nuclei. The proposed site of the νp-process are the proton-rich ejecta created by a strong neutrino flux in supernovae. In this scenario, neutrons produced by the reaction $\bar{\nu} + p \rightarrow n + e^+$ would be captured by neutron-deficient nuclei. This would allow the flow to bypass the slow β decays via (n,p) reactions, resulting in nucleosynthesis above $A = 64$ [8].

1.2 Type I X-Ray Bursts

Type I X-Ray Bursts were discovered as a sharp rise in the luminosity of an X-ray source followed by a slower cooling phase lasting for tens of seconds to about a minute and repeating on timescales of hours to days [11,12] (see for example [13] for a review). They have been interpreted as the result of thermonuclear explosions on the surface of a neutron star that accretes hydrogen- and helium-rich matter from the outer layers of a low-mass companion. In such binary systems, the neutron star has an average mass of ≈ 1.4 M$_\odot$ (or larger, according to recent photospheric radius expansion burst studies [14]), a radius of about 10-15 km and a density of the order of 10^{14} g/cm^3 [15]. The companion (or donor) star is, typically, a metal poor low mass star ($\lesssim 1.5$ M$_\odot$).
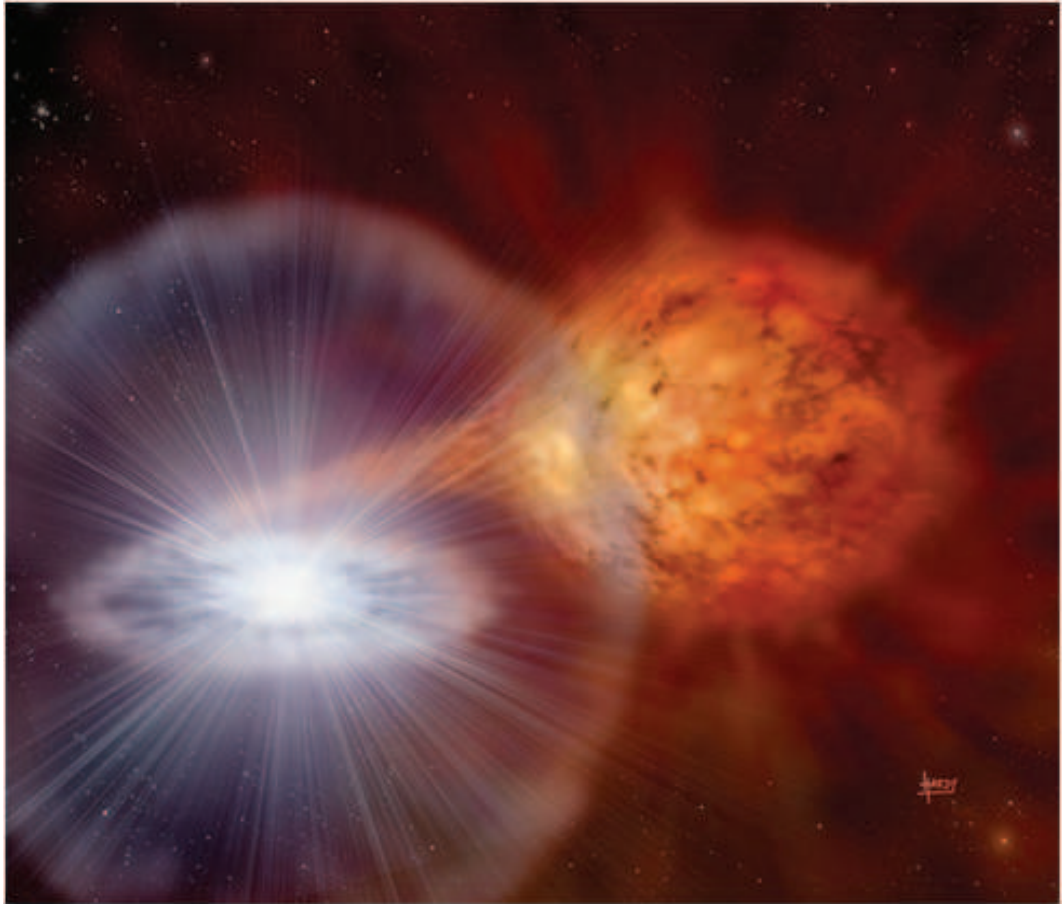
Figure 1.2: For interpretation of the references to color in this and all other figures, the reader is referred to the electronic version of this dissertation. Artist rendition of an X-ray binary system. The neutron star (left) accretes hydrogen- and helium-rich matter from its companion (right), which undergo a thermonuclear runaway in the surface of the neutron star, resulting in the observed Type I X-ray bursts (see text for details). Image credit: David Hardy.

An artistic rendition of an accreting neutron star in a binary system is shown in Fig. 1.2.

Proton-rich matter is transferred to the neutron star via Roche lobe overflow. The Roche lobe is a gravitational equipotential surface around a star that outlines the volume within wich material is gravitationally bound to the star. The location where the two Roche lobes in a binary system touch is called the inner Lagrangian point [15]. When the donor star fills its Roche lobe, matter from its envelope will flow out towards the neutron star though the inner Lagrangian point, creating an accretion disk around the neutron star and spiralling down to its surface.

The falling of mass onto the neutron star releases gravitational energy, heating the surface of the neutron star to temperatures around 10^7K [15]. As a result, a continuous X-ray flux is emitted. At typical accretion rates of $10^{-8} - 10^{-10}$ M$_\odot$/yr, mass accumulation causes an increasing temperature and density until temperature-sensitive fusion reactions ensue. These reactions in turn generate heat that further accelerates the thermonuclear reaction rates, which increase the temperature even further, thus triggering even more reactions and so on. The result is a thermonuclear runaway in which, typically, 10^{39-40} ergs of energy are released. The time rise in the light curve is fast (1 to 10 s), reaching peak temperatures of 1.5 to 2 GK in the nuclear burning zone [16], and it is followed by a slower decline of about 10 to 100 seconds that reflects cooling of the neutron star surface. With recurrence times of the order of hours to days, type I X-ray bursts are the most frequent thermonuclear explosive events observed in nature. To date, more than 3000 bursts have been observed. A large amount of observational data, accumulated during the past few decades, has made possible the discovery and monitoring of various X-ray burst properties with high precision, such as millisecond oscillations [13, 17]. The thermonuclear origin of these phenomena therefore requires detailed understanding of the underlying nuclear physics in order to construct a complete description of the X-ray bursts.

The nuclear processes responsible for the energy generation during X-ray bursts depend upon several parameters of the binary system, such as accretion rate and composition of the accreted material, which in turn are related to distance and rotational period between the two stars and to the nature of the companion [13, 15]. For bursts accreting at rates between 10^{-8} to 10^{-10} M$_\odot$/yr nuclear burning is ignited at densities above $\rho = 10^5$ g/cm^3 mostly via the triple-α process [5]. As a result of these reactions the temperature can reach 3×10^8 K, which in turn triggers the αp and the rp-process. The rp-process determines the light curve of the X-ray burst and sets the initial composition for all subsequent processes occurring deeper in the crust of the neutron star.

1.2.1 The rp-process

The rp-process consists of a sequence of fast (p,γ) reactions competing with photodis-integration and β^+-decays. The reaction path runs mostly along the proton-drip line. Figure 1.3 shows the reaction flow of the rp-process in an X-ray burst. When the Q-value for further proton capture is either too small or negative, photodisintegration or proton decay can occur. At this point, the reaction flow has to wait for the nucleus to β^+ decay (so that proton capture on the daughter nucleus can resume the process), and therefore mass accumulation occurs at the corresponding nuclide. These long-lived nuclei along the reaction path are referred to as waiting points [5] and their β-decay half-lives determine the processing time scale and the final abundances of the rp-process. The even-even $N = Z$ nuclei beyond ^{56}Ni represent the major waiting points, together with a few more stable isotopes, depending on the exact conditions. Among these, ^{96}Cd was the only one with a still unknown β-decay half-life. As mentioned above, the origin of ^{96}Ru in the solar system is not understood, and the isotope could at least in principle, be produced in the rp-process. The produced amount of ^{96}Ru in the burst ashes scales with the half-life of ^{96}Cd. Additionally, a long ^{96}Cd half-life would reduce the amount of heavier nuclei produced in the rp-process.

Abundance pattern

The long lived waiting point nuclei along the rp-process reaction path store most of the material until the burning ends, therefore, their half-lives determine the resulting isotopic abundances. The effective lifetimes of the rp-process waiting points are a crucial ingredient in abundance calculations. One needs to take into account the possibility of population of excited states in the astrophysical environment and use the appropriate half-lives determined experimentally.

The abundance pattern created by an X-ray burst can be calculated through a nuclear reaction network. The isotopic abundances $Y_i = X_i/A_i$, defined as the mass fraction divided by mass number, are modeled as a function of time using set of dif-
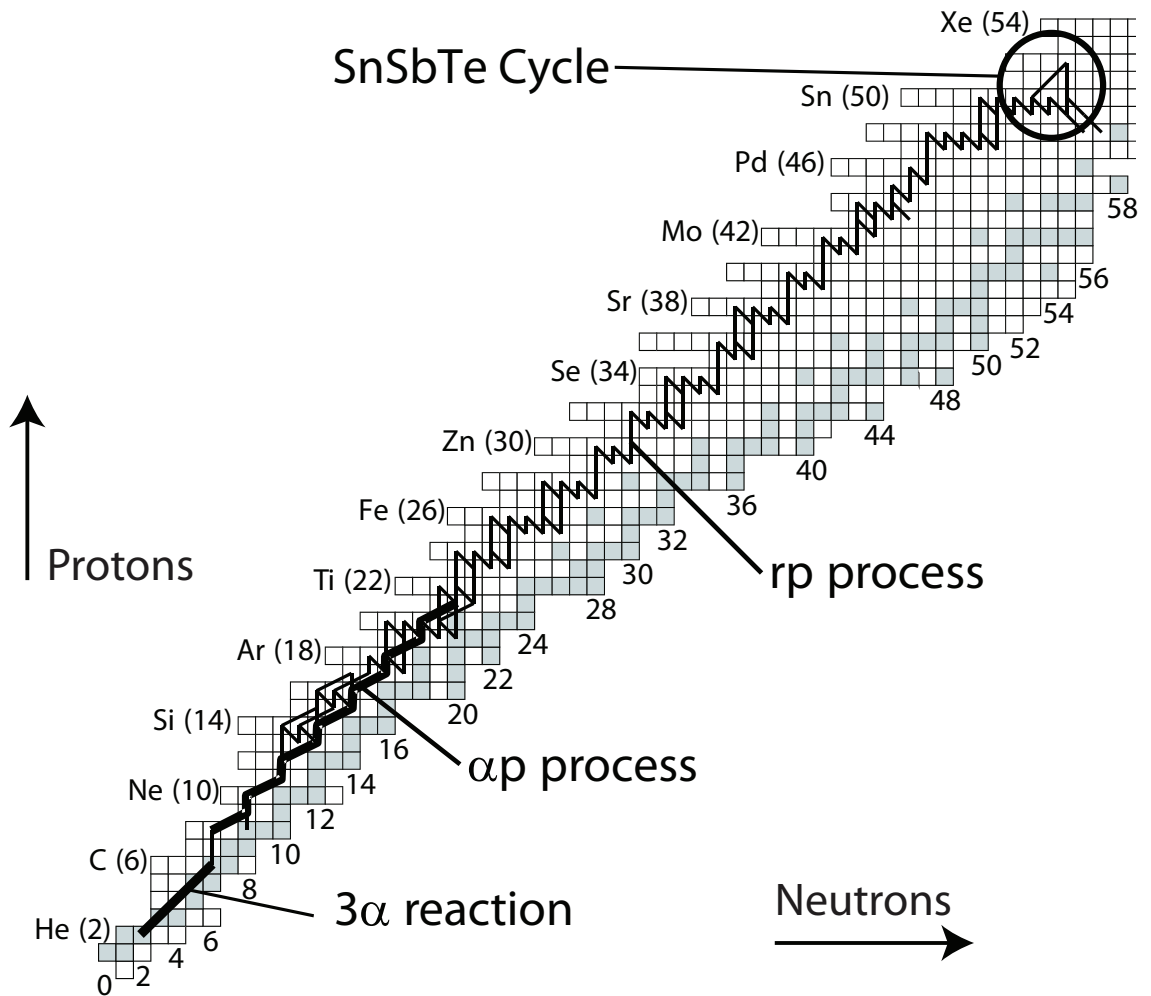
Figure 1.3: Section of the chart of nuclides indicating the path followed by the rp-process in an X-ray burst. Figure adapted from [18].

ferential equations in order to determine the reaction path of the process and the amount of energy released [5]. Crucial input for these reaction networks, besides parameters of the astrophysical environment, are proton-capture reaction rates, proton separation energies and half-lives of all the nuclei involved.

The rp-process could produce light p-nuclei through the β^+ decay of the unstable proton-rich isobars created by proton captures. Using a nuclear reaction network that included all proton rich nuclei from hydrogen to xenon, Schatz *et al.* [19] found large overproduction factors (produced abundance normalized to solar abundance $\approx 10^9$) for the p-nuclei ^{98}Ru, ^{102}Pd and ^{106}Cd. However, in order for X-ray bursts to contribute to galactic nucleosynthesis, it is required that the processed material escapes the neutron star and enriches the interstellar medium [20].

Characterization of the final abundance pattern of X-ray bursts is not only important for nucleosynthesis considerations, but also for probing the properties of neutron stars. Most of the ashes of the rp-process will become part of the neutron star crust, and will set the initial conditions for all subsequent crust processes, some of which could be directly linked to observables [13, 15].

Endpoint

Determination of the endpoint of the rp-process is crucial in order to estimate the abundance pattern, as well as the amount of hydrogen left after burning is over.

The endpoint of a particular X-ray burst depends on system parameters and initial ignition conditions.Several rp-process simulations for X-ray bursts showed that the reaction path reached the end of their respective reaction networks, in the Kr-Y region [21–25], or up to Cd [26] and Sn [5]. When a large amount of hydrogen is present in the accreted matter the rp-process can extend into the $A \sim 92 - 110$ mass region, where the SnSbTe cycle represents a natural endpoint [19]. Schatz *et al.* [19] showed that nucleosynthesis in the rp-process is limited to nuclei with $Z \leq 54$ under all rp-process conditions as a consequence of the low α separation energies of the

$^{106-109}$Te isotopes.

The SnSbTe cycle is schematically shown in Figure 1.4. Once the reaction flow reaches the light tin nuclei, further processing will occur if the corresponding Sb isotone is sufficiently proton bound for the (γ, p) photodissintegration to be small [19]. The β^+-decays of $^{99-104}$Sn followed by proton captures on the corresponding indium isotopes drive the flow towards greater stability. When ^{105}Sn is reached, proton capture can proceed towards ^{106}Sb and then to ^{107}Te. At this point, however, the (γ, α) photodisintegration rate will dominate and the flow will return to ^{103}Sb, forming a cycle that forbids processing towards heavier nuclei. ^{105}Sn is a branching point, that sends part of the reaction flow towards ^{105}In via β^+-decay, thus forming the weaker cycle shown in Figure 1.4.

New experimental data on reaction rates and masses of rp-process nuclei have lead to a better estimate of the final abundances. A recent one-dimensional X-ray burst model calculation with updated reaction rates showed that significantly less material is processed toward the end of the rp-process, resulting in accordingly reduced abundances beyond $A = 80$ [27].

New and improved mass measurements of $^{104-108}$Sn and $^{106-110}$Sb and determination of their respective one-proton separation energies lead Elomaa *et al.* [28] to suggest an earlier termination of the rp-process. The new, low proton separation energy (S_p=424(8) keV, in contrast to the previously adopted value of 930(210) keV) determined for ^{106}Sb implies that the branching into the SnSbTe cycle is weaker. Therefore, cycling is almost absent in current X-ray burst calculations and the reaction path runs closer to stability. This affects the final abundances, in particular, it reduces the late-time ^{4}He production by the SnSbTe cycle.

The remaining uncertainties in the determination of the endpoint are the proton-capture rates on ^{105,106}Sb. Larger rates could potentially increase the amount of cycling in the SnSbTe cycles [28].
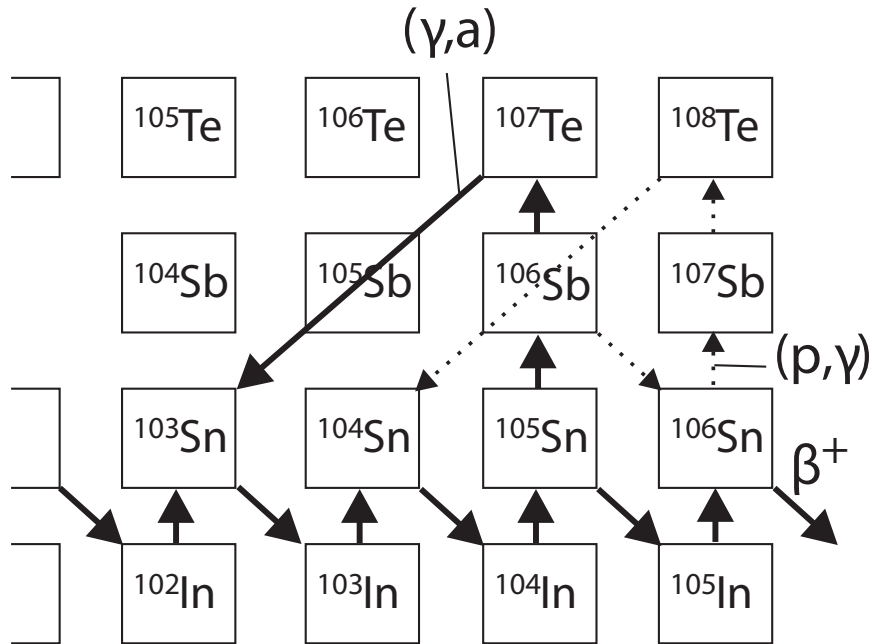
Figure 1.4: Schematic view of the SnSbTe cycle. The solid line represents flow of more than 10% and the dashed line corresponds to 1%-10%. Figure adapted from [19].

Consequences on crust composition

The rp-process, besides powering the light curve of X-ray bursts, sets the composition of the liquid ocean and solid crust of the underlying neutron star. As the mass transfer continues in the binary system, the reaction products of the rp-process are pushed deeper in the crust of the neutron star. Therefore, the ashes of previous bursts determine the initial composition for subsequent bursts or even superbursts. Superbursts are extremely powerful X-ray bursts in which the energy release is $\sim 10^3$ times that of a regular burst, and are thought to be the result of carbon burning. They occur with less frequency but have longer cooling timescales [13].

When ashes of the rp-process are compressed even further the electron chemical potential rises with increasing density, switching on electron capture reactions. These reactions produce very neutron-rich unstable nuclei and their energy generation contributes to the heating of the crust. Gupta *et al.* [29] showed that the exact composition of the ashes needs to be known to determine heating processes in the crust and ocean of the neutron star that directly influence observables such as su-

perbursts ignition depth. In addition, knowledge of the composition of the crust is essential for models to determine the thermal and electrical conductivities, as well as evolution of magnetic fields in the neutron star (e.g. [7, 30] and references therein). Also, cooling of the crust determines the quiescent luminosity in transients (neutron stars with intermittent periods of rapid accretion) [31].

On the other hand, observables from nuclear processes in the crust and envelope of the neutron star can be used to constrain its mass and radius, thus providing valuable information to determine the equation of state of nuclear matter at high densities and low temperatures ([14, 32, 33] and references therein).

Ejection of ashes

Whether the rp-process in X-ray bursts contribute or not to nucleosynthesis of heavy proton-rich isotopes is still a matter of debate. Identifying an ejection mechanism of the rp-process ashes, given the strong gravity on the surface of a neutron star, is a challenging task. It is estimated that at most a few percent of the synthesized matter can escape the gravitational potential of the neutron star ($E_{gravitational}/E_{nuclear} \gtrsim 40$ [7]).

Weinberg *et al.* [20] demonstrated that such an ejection mechanism in principle exists. Their calculations showed that heavy-element ashes of nuclear burning can be transported via convection to the surface of the neutron star, where they could be ejected in the strong radiative winds of photospheric radius expansion (PRE) bursts and produce strong spectral absorption features. Later, in 't Zand and Weinberg [34] showed observational evidence of the exposure of ashes of nuclear burning in superexpansion bursts.

Accurate determination of the burst ashes, together with a better understanding of the possible ejection mechanisms will help identify abundance signatures for future X-ray observational explorations.

Chapter 2

Nuclear Physics

The importance of the nuclear physics of the stable and radioactive isotopes participating in the rp-process was established in the preceding chapter. The following sections provide an overview of the theoretical framework of the physics of neutron deficient nuclei in the region around ^{100}Sn. Also, an introduction will be given to some of the observables that allow us to probe the structure of these exotic neutron-deficient nuclei.

The atomic nucleus is a quantum many-body system, and analyzing the interactions among its constituents in order to understand its behaviour as a whole is a daunting mathematical task. Approximations are therefore requiered to describe all but the lightest nuclei. The shell model of the nucleus, in analogy to the atomic shell model, describes the motion of a single nucleon as governed by the average potential created by all other nucleons. Solving the Schrödinger equation for a suitable single-particle potential (consisting, for example, of a central Woods-Saxon potential plus a strong spin-orbit coupling term) one gets bound single-particle states characterized by a quantum number n, orbital angular momentum l, and total angular momentum $j = l + s$ (with $s = 1/2$ for both protons and neutrons). The resulting energy levels are arranged in a structure that resembles that of the atomic shell model, the filling of shells proceeds in accordance with the Pauli exclusion principle, and the maximum

number of particles in a given level is equal to $(2j+1)$. Full shells correspond to an energetically favorable configuration and therefore to enhanced stability of the nucleus. Particles left out of a closed shell (valence nucleons) will, as in the case of the atomic shell model, determine the properties of the nucleus, such as its spin, parity (equal to $(-1)^l$), excitation energy and possible decay modes. The single-particle energy levels predicted by a shell model are illustrated in Figure 2.1. The relative positions inside a major shell as well as gaps between the shells are different in various versions of the shell model. A shell-model calculation is based upon a subset of single-particle states together with their interaction via an effective two (or more) body hamiltonian [35].

One of the main successes of the shell model is its ability to predict the occurrence of the so-called magic numbers, which correspond to the filling of major shells. Such magic numbers of proton and neutrons are 2, 8, 20, 28, 50, 82 and 126. Nuclei with a magic N or Z number exhibit extra stability and correspond to major gaps in the spacings of the single-particle energies. When a nucleus has both, a magic number of neutrons and a magic number of protons, it is called doubly-magic. With $N = Z = 50$, ^{100}Sn is believed to be a doubly magic nucleus, and it is therefore of great interest for both experimental and theoretical studies.

2.1 Nuclear Structure around ^{100}Sn

Neutron deficient nuclei in the neighborhood of the expected doubly magic ^{100}Sn are an important testing ground for shell model calculations. The low-energy structure of these nuclei is of great importance to confirm the closure of shells at $N = Z = 50$. Shell-model calculations rely on the closed-shell property of the doubly-magic nuclei, which provides a good zeroth-order wave function that can be systematically improved using perturbation theory [36]. Additionally, the equal number of protons and neutrons provides excellent conditions for the study of the residual proton-neutron interaction in identical orbits ($\pi - \nu$ pairing) and the role of core excitations [37]. One
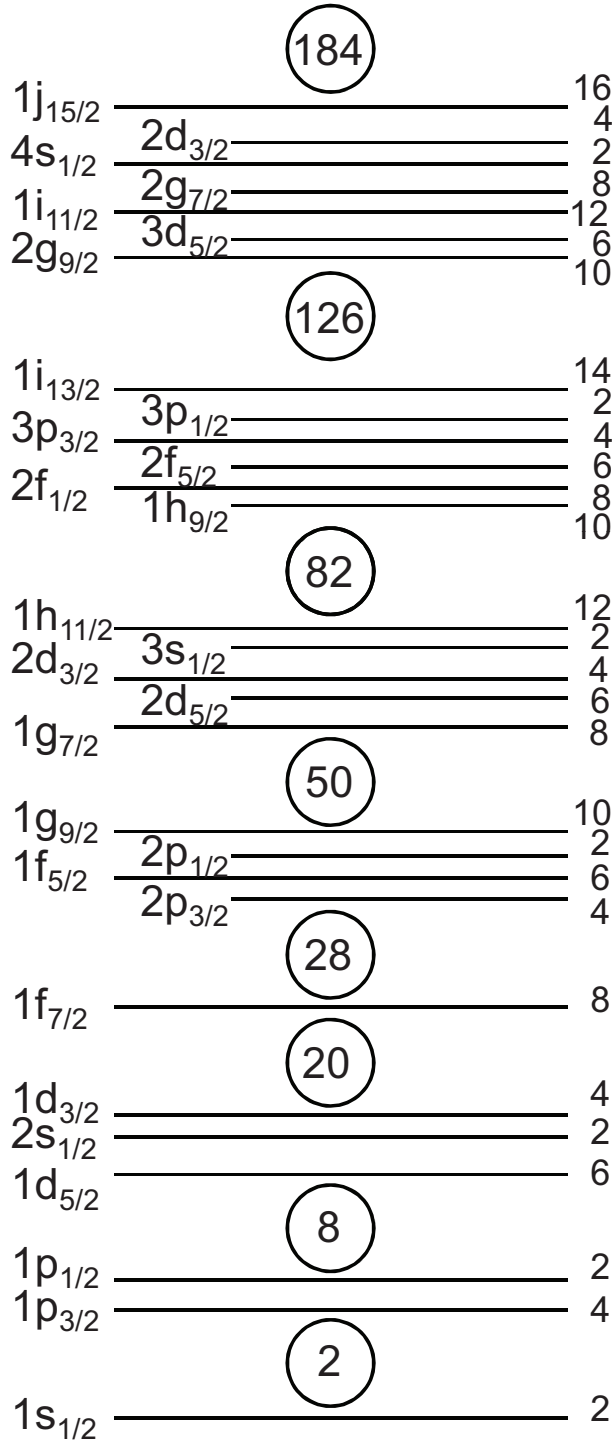
Figure 2.1: Schematic representation of single-particle energy levels calculated by the nuclear shell model. Neutrons and protons are counted separately. Spectroscopic notation (nlj) is used to label the states, where n is used to number the various states of given l and j. The magic numbers are indicated. The number of identical nucleons allowed at a given level is indicated on the right.
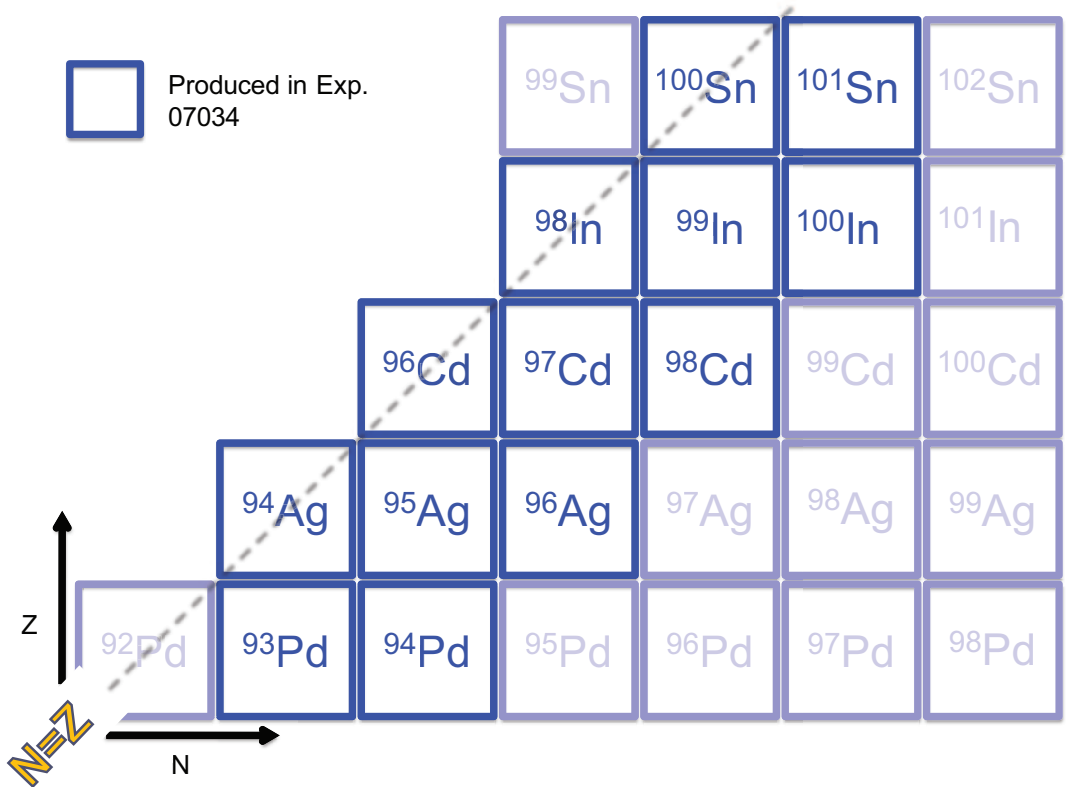
Figure 2.2: Section of the chart of nuclides of interest in the present study. The $N = Z$ line is indicated, and the nuclei produced in Experiment 07034 are highlighted in dark blue.

of the current challenges for nuclear physics is to explore the limits of prediction for the existing models and to develop extrapolations for those nuclei which are not yet within reach of experimental facilities but that are relevant for models of nucleosynthesis in astrophysical scenarios.

Numerous experiments in recent years have been dedicated to the production and study of $N \sim Z$ nuclei in the vicinity of ^{100}Sn. β decays with large Q-values, β-delayed proton emission, and spin-gap isomers can observed in this mass region, and the results have challenged shell model calculations (e.g. [?, 38–41]). Shown in Fig. 2.2 is the portion of the chart of nuclides of interest in this study, the nuclei produced in our experiment are highlighted.

A variety of model spaces and effective interactions have been used by shell model calculations to explain observed properties of $N \sim Z$ nuclei that were previously

not predicted, such as some of the recently observed high-spin isomers. To cite an example, the observed 21^+ state in ^{94}Ag has been reported to decay by a variety of channels and raised much discussion about its nature ([42] and references therein).

A shell model with a minimum model space comprising $p_{1/2}$ and $g_{9/2}$ protons and neutrons generally provided a good description of the structure of these nuclei. It successfully reproduced observed energy levels and half-lives in ^{95}Ag, ^{95}Pd, and ^{94}Pd, but it failed to predict the isomerism of the 21^+ state in ^{94}Ag [43, 44]. Use of a larger model space is therefore required to explain some of the new observations. Shell model calculations including the $p_{3/2}$, $f_{5/2}$ and $g_{7/2}$ orbitals and using realistic interactions were developed for this purpose [45].

Shell model calculations with larger model spaces have investigated the role of deformation and shape coexistence in the isomers observed in this region of the chart of nuclides. Also, core excitations have been found to be necessary to explain some high-spin isomeric states, such as those occurring in ^{98}Cd [41], ^{94}Ag [43] and ^{94}Pd [46] (See section 2.4 below).

2.2 Beta Decay

Nuclei sufficiently far on the neutron-deficient side of the valley of stability may undergo β^+ decay. Through β^+ decay a proton within the nucleus is transformed into a neutron via the following process:

$$^A_Z X \rightarrow^A_{Z-1} X'_{N+1} + e^+ + \nu$$
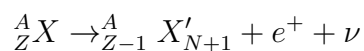
As the mass number A remains constant, β^+ decay provides a means for the nucleus to approach the stable isobar of the chain. The Q value of the decay can be calculated as [47]:

$$Q_\beta^+ = [m(^A X) - m(^A X') - 2m_e]c^2 \tag{2.1}$$

Table 2.1: β decay angular momentum and parity selection rules. $\Delta J = |J_i - J_f|$ $\Delta \pi$ represents the change in parity between initial and final states, equal to $(-1)^l$. Adapted from [48]

Transition type	ΔJ	$\Delta \pi$	$\log_{10} ft_{1/2}$
Superallowed	$0^+ \to 0^+$	no	3.1 - 3.6
Allowed	0,1	no	2.9 - 10
First forbidden	0,1,2	yes	5 - 19
Second forbidden	1,2,3	no	10 - 18
Third forbidden	2,3,4	yes	17 - 22
Fourth forbidden	3,4,5	no	22 - 24

where $m(^A X)$ denote neutral atomic masses:

$$m(^A X)c^2 = m_N(^A X)c^2 + Z m_e c^2 - \sum_{i=1}^{Z} B_i \tag{2.2}$$

with m_N the nuclear mass, m_e the mass of the electron and B_i the binding energy of the ith electron. β^+ decay is energetically possible when the atomic mass energy difference is at least $2m_e c^2$=1.022 MeV. The sum of the kinetic energies of the positron and the neutrino is equal to the β-endpoint energy, ignoring the recoil of the residual nucleus. Measuring the energy spectrum of the positrons emitted in β^+ decay therefore provides a measurement of the Q value, which in turn yields information about the energy difference between initial and final nuclear states.

Several final states can be populated in the daughter nucleus following β decay. Angular momentum and parity selection rules for β decay dictate which nuclear states can be populated. These rules are summarized in Table 2.1. The listed $\log ft$-values, also known as comparative half-lives, represent standard measures of the strength of a given β-decay transition. As the range of half-lives in β decay is large, $\log_{10} ft$ values (with t given in seconds) are quoted for convenience. They are useful in comparing β decay probabilities in various nuclei as the differences in ft values must be due to differences in the nuclear wave function and therefore to differences in nuclear matrix elements [47].

Measurements of branching ratios can therefore constrain the spins and parities

of the nuclear states involved. Furthermore, some nuclei studied in this work were created in excited states, which exhibited competing decay modes (see Section 2.4). Detailed nuclear structure is therefore elucidated from the detection of the different decay products and from the corresponding half-life measurements. Besides nuclear masses, β-decay half-lives are among the most important nuclear physics ingredients in the prediction of the rp-process path, energy generation rate and final composition. The half-life measurements performed in our experiment are reported in Chapter 5, and their incorporation into an rp-process reaction network is presented in Chapter 6.

2.3   Gamma Decay

Most of the nuclear excited states populated through β^+ decay in our experiment decayed by emission of γ-rays. As the energy of a γ transition corresponds to the energy difference between initial and final nuclear states, one can obtain information on the excitation energy of the states populated in the β decay by performing β-delayed γ spectroscopy. Additionally, as the lifetimes characteristic of γ de-excitation are usually very rapid compared to β decay, β-delayed γ emission occurs with a half-life characteristic of the β decay, and γ transitions can then be used to obtain a virtually background-free β-decay curve of the parent nucleus, which helps disentangle the various decay components (see Chapter 5).

Also, some of the nuclei produced by fragmentation were created in long-lived excited states (isomers) that decayed by γ-ray emission within a few microseconds of reaching the experimental endstation. In the cases where the statistics were sufficient, we were able to obtain $\gamma\gamma$ coincidences, that is, two or more γ transitions were detected simultaneously, indicating that they correspond to the consecutive de-excitation of states in a given nucleus (i.e. a γ cascade). This information, combined with that from β decay, allowed us to extract information on the level scheme of the parent nucleus.

The emitted electromagnetic radiation during γ de-excitation is generated by a reconfiguration of the protons and neutrons in the nucleus. The resulting electromagnetic radiation field is of multipole order 2^L, where L corresponds to the angular momentum carried away by the emitted photon. The γ transitions can be of electric (E) or magnetic (M) nature depending on the relative parity of the initial and final levels. The angular momentum and parity selection rules for electromagnetic transitions are:

$$|I_f - I_i| \le L \le I_f - I_i \qquad (\text{no } L = 0)$$

$$\Delta\pi = no: \qquad \text{even electric, odd magnetic}$$

$$\Delta\pi = yes: \qquad \text{odd electric, even magnetic}$$

When $I_i = I_f$ the lowest possible γ-ray multipole order is dipole, and therefore $L = 1$. In the case of $I_f - I_i = 0$ the state can only decay by internal conversion, or if the energy is sufficiently high, by pair emission. In the electron conversion process the nucleus transfers its excitation energy directly to an orbital electron without emission of a γ-ray. The atomic electron is therefore ejected with a kinetic energy

$$T_e = \Delta E - B_e$$

which is equal to the transition energy minus the binding energy of the electron. The vacancy left by the emitted electron is quickly occupied by another electron from a higher shell, followed by the emission of a characteristic X-ray (with energy equal to the difference between initial and final electronic orbits).

Internal conversion is an electromagnetic process that competes with γ decay. The ratio of the two decay modes is defined as the internal conversion coefficient α

Table 2.2: Weisskopf single-particle estimates for the lowest electric ($E\lambda$) and magnetic ($B\lambda$) transition probabilities (in units of s^{-1}). E is the energy of the γ transition in MeV. Values from Ref. [48]

Electric transitions	Magnetic transitions
$\lambda(E1) = 1.02 \times 10^{14} A^{2/3} E^3$	$\lambda(M1) = 3.15 \times 10^{13} E^3$
$\lambda(E2) = 7.28 \times 10^{7} A^{4/3} E^5$	$\lambda(M2) = 2.24 \times 10^{7} A^{2/3} E^5$
$\lambda(E3) = 3.39 \times 10 A^{2} E^7$	$\lambda(M3) = 1.04 \times 10 A^{4/3} E^7$
$\lambda(E4) = 1.07 \times 10^{-5} A^{8/3} E^9$	$\lambda(M4) = 3.27 \times 10^{-6} A^{2} E^9$

$$\alpha = \frac{\lambda_e}{\lambda_\gamma}$$

The total decay probability will therefore have two components: $\lambda_t = \lambda_\gamma + \lambda_e$, or

$$\lambda_t = \lambda_\gamma(1 + \alpha) \tag{2.3}$$

In a simplified model of the γ decay we can regard the electromagnetic transition as the result of a single proton changing from one state to another. Then, the probability per unit time (λ_γ) for photon emission can be calculated using perturbation theory, and the result is known as the Weisskopf single-particle estimate for the λth multipole. These estimates can be used to compare measured decay rates and to infer their multipolarities. The Weisskopf estimates for the first four multipole orders are listed in Table 2.2.

2.4 Isomeric States

As mentioned in the previous chapter, characterization of isomers along the rp-process path is necessary to calculate corrections for the lifetimes of these nuclei in the astrophysical environment. The role of an isomer in the rp-process will depend on the amount of isomer produced, the time scale for thermalization, and on how different proton capture and β-decay rates of ground and isomeric states are. The half-lives of isomeric states and of the ground state of a nucleus must therefore be disentangled

for astrophysical calculations.

Nuclear isomers can be caused by either deformation (shape isomers), or by a large change in spin required for decay (spin-gap isomers), or by a large difference in spin orientation relative to an axis of symmetry (K-isomers) [49]. These excited states decay often by electromagnetic processes (γ decay or internal conversion). Also α, β, electron capture, proton, neutron or even nuclear fission are possible decay modes [50].

One reason for the appearance of high-spin isomers in the ^{100}Sn region is an extra binding energy due to the large attractive proton-neutron (pn) interaction in the maximally aligned particle-particle or hole-hole configurations. The residual interaction between a proton and a neutron in the $g_{9/2}$ shell produces states with large spin differences, which are very close in energy [42, 50]. A number of isomers have been predicted to exist in the region around ^{100}Sn (e.g. [1]), and several have been experimentally confirmed. Some remarkable examples of high-spin γ-decaying isomers are the $23/2^+$ and $37/2^+$ states in ^{95}Ag [40,51], 14^+ in ^{94}Pd [43,51], and 12^+ in ^{98}Cd [41]. β- and β- delayed proton (βp)-decaying isomers have also been found in the region, examples of which are the 21^+ level in ^{94}Ag [43,44,52] and the $25/2^+$ level in ^{97}Cd [53].

A β-decaying 16^+ spin-gap isomer was predicted at an excitation energy of 5.30 MeV in ^{96}Cd [1,42], with a half-life of 0.5 seconds. The predicted level scheme of ^{96}Cd is shown in Fig. 2.3. One of the goals of Experiment 07034 was to search for this isomer.

An additional goal of our experiment was the search for isomers in isotopes with previously measured half-lives as it is possible that experiments with limited statistics measured mixed half-lives of ground and isomeric states. For instance, the half-life of ^{97}Cd was measured in a low statistics experiment [50] in which it was not possible to dissentangle different decay components.
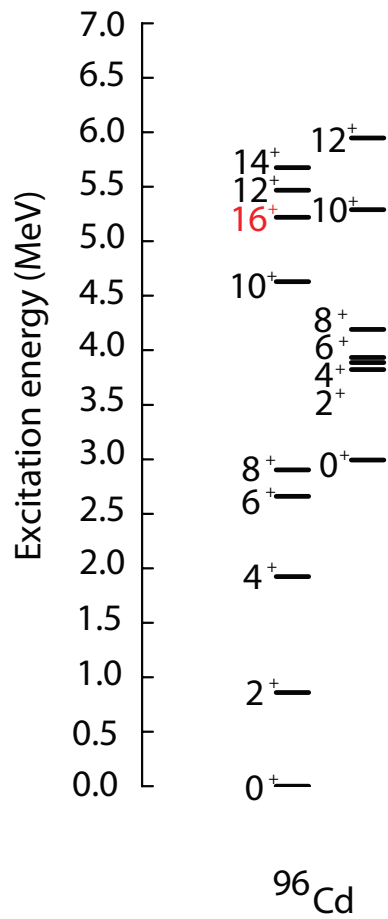
Figure 2.3: Calculated level scheme of ^{96}Cd. A 16^+ β-decaying spin-gap isomer is predicted at an excitation energy of about 5.3 MeV. Figure adapted from [42].

Chapter 3

Experimental Setup

The experiment described in this work, Experiment 07034 "Study of the β-decay of ^{100}Sn", was performed at the National Superconducting Cyclotron Laboratory at Michigan State University. The NSCL is a rare-isotope facility where radioactive ion beams are produced by fragmentation of a primary beam impinging upon a light target. Two superconducting cyclotrons coupled together accelerate the primary beam up to 40% of the speed of light, and the fragments resulting from the collision with the target are identified and separated by the A1900 Fragment Separator [54] through the $B\rho$-ΔE-$B\rho$ selection technique, and, in the case of proton-rich nuclei, through an additional velocity selection provided by the Radio Frequency Fragment Separator [55]. The purified secondary beam is then sent to an experimental station for its detailed study. Figure 3.1 shows a schematic layout of the laboratory, indicating the areas associated with the production, separation and study of rare ion beams. In the following sections the experimental setup and techinques used in our study will be described in detail.
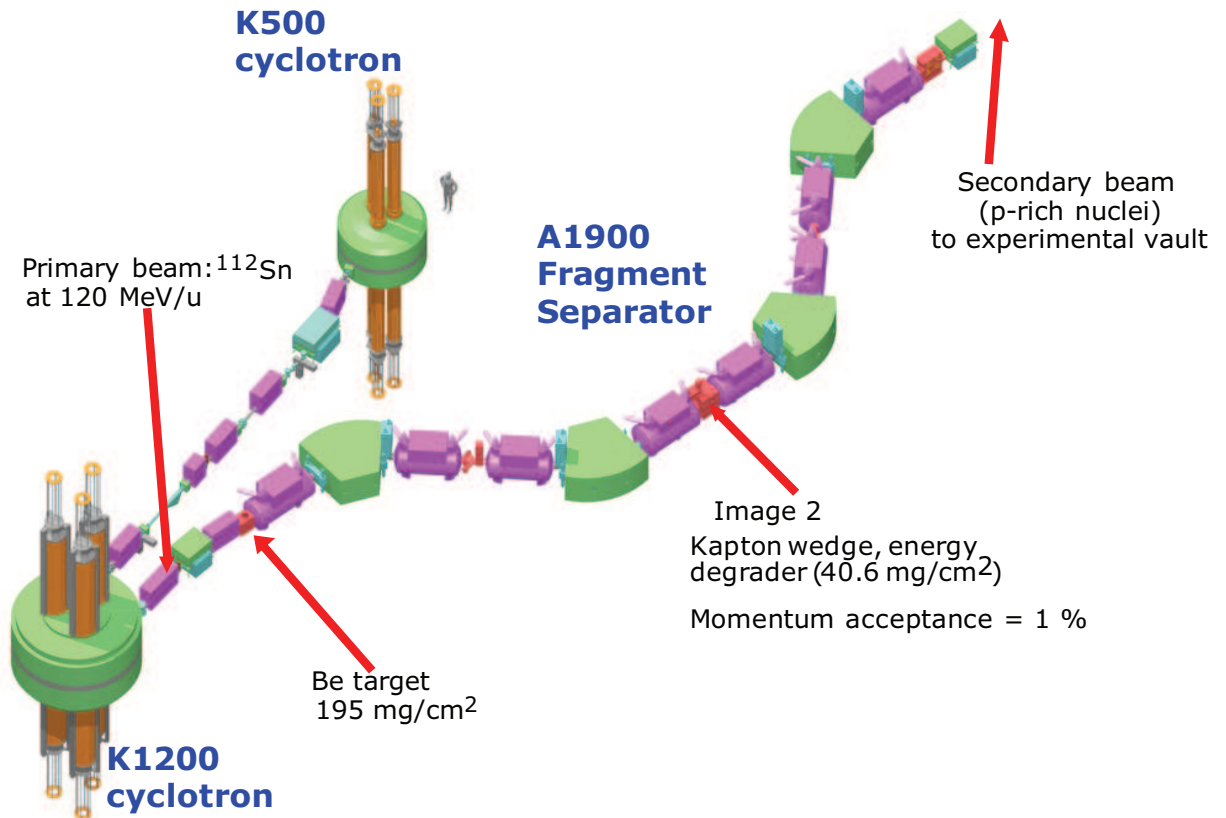
Figure 3.1: Ion beam production and delivery to the experimental station at NSCL. A primary beam of stable ions is accelerated in the coupled cyclotrons and impinged upon a Be target. Exotic fragments of interest are separated with the A1900 Fragment Separator in conjunction with the RFFS to be delivered to the experimental station.

3.1 Projectile Fragmentation at NSCL

In projectile fragmentation high-energy nuclei are broken into smaller residue nuclei that retain most of the vector momenta of the beam [56]. The process can be understood in terms of the so-called abrasion-ablation model, which consists of two basic steps. In the abrasion step, the overlapping portions of projectile and target nuclei are sheared away by the collision, and the remaining projectile, also called prefragment, continues to travel forward with a minor decrease of velocity [57]. The projectile is left, however, with a region of extra surface area exposed by the collision, which translates into an excitation energy according to the semiempirical mass equation of about 1 MeV per excess fm^2 of surface area [58]. In the ablation step, the excess surface energy becomes available as excitation energy and the prefragment subsequently

decays by emission of γ radiation and/or nucleons, leading to a secondary product, or nuclear fragment whose properties are then studied.

The secondary beam is initially composed of a variety of fragments, which must be separated in order to obtain a sufficiently pure radioactive nuclear beam. At the NSCL this separation is done by the A1900 Fragment Separator, which uses a separation method based on magnetic rigidity analysis and energy loss in degrader materials [59]. The A1900 Fragment Separator uses four superconducting dipole magnets to bend the ions for momentum-to-charge ratio selection, according to:

$$B\rho = p/q = \gamma mv/q \tag{3.1}$$

The first half of the device selects the secondary fragments with magnetic rigidities $B\rho$ within a given acceptance. The momentum acceptance can be adjusted by slits placed at the dispersive planes. Further selection is achieved by inserting an energy degrader at the intermediate image (Image 2 in Fig. 3.1), in which the ions lose different energies depending on their atomic number, and emerge with different magnetic rigidities. At Image 2, a thin plastic scintillator can be used for fragment tracking. The second half of the device provides elemental separation by an additional bend after the rigidity change in the wedge and provides an achromatic image of the target spot that results in a small beam that can be transported through the beamline. At the final focal plane, prior to sending the purified beam to the experimental vault, unambiguous particle identification is perfomed. Diagnostic detectors are inserted during the setup of the separator and then removed to send the beam to the experimental vault. A thin plastic scintillator (XFP scintillator) is used to provide a time signal for Time-of-Flight (TOF) determination. A pair of Parallel Plate Avalanche Counters (PPACs) can be used to measure the position and angle of the fragments, which are then stopped in a stack of silicon PIN detectors in front of a HPGe detector. This method is used to tag ions in isomeric states with half-lives in the microsecond range,

which decay by emission of γ-rays. The detection of known isomers is then used to verify the particle identification of the rest of the fragments (See section 4.1.2).

Two key characteristics of the projectile fragmentation mechanism that determine the properties of the radioactive beam are the cross sections and the fragment momentum distributions. The cross-sections are largest for fragments close in mass to the projectile, and decrease within an isotopic chain for higher and lower mass number [56]. The momentum distributions are characterized by a small decrease in velocity compared to the incident beam and a nearly Gaussian spreading, which is larger than the velocity decrease. However, the momentum distributions of neutron-deficient fragments produced by primary beams in the energy regime between 50 and 200 MeV, as is the case at NSCL, are asymmetric, exhibiting long tails on the low momentum side due to additional dissipative processes during the collision.

The momentum distributions of neutron-deficient isotopes are peaked at lower magnetic rigidities than that of their more stable isotopes upon exiting the A1900 Fragment Separator. The low momentum tails of these more abundant contaminants therefore overlap with the peak of the momentum distribution of the fragments of interest for a given magnetic rigidity setting of the separator, thus creating a serious problem of contamination for decay studies. Figure 3.2 illustrates this contamination problem for the case of production and separation of ^{100}Sn, as calculated with the program LISE++ [60]. Successful decay studies under these conditions would not be possible due to an overwhelming number of random ion-decay correlations (See Section 4.2). Therefore, further purification of the secondary beam is necessary.

However, one can see from equation 3.1 that, for a constant Bρ, the different mass to charge ratios m/q correspond to different velocities. That is, particles in the low momentum tails of the contaminants (i.e. with higher m/q than the neutron-deficient fragments of interest) have lower velocities compared to the particles of interest that are selected at the maximum of their momentum distribution.

These differences in velocity can thus be used as an additional mechanism to
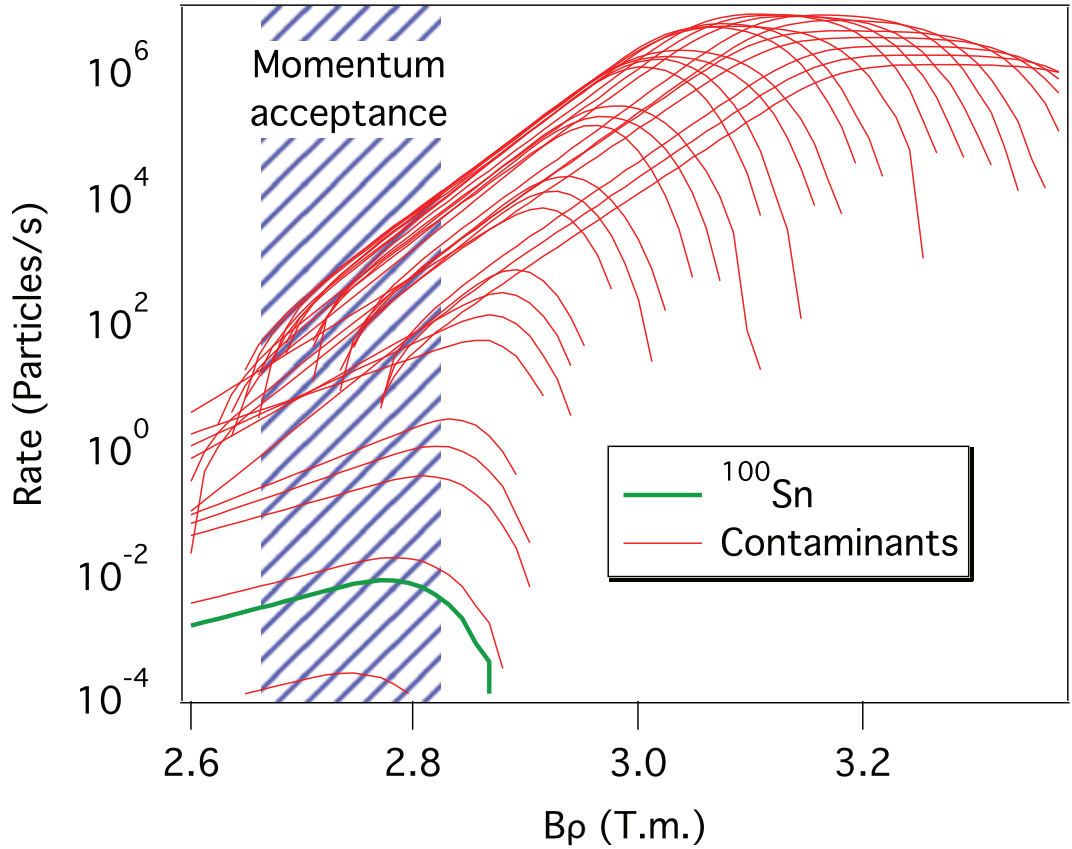
Figure 3.2: Production rates of ^{100}Sn and closest neighbors as a function of Bρ at the exit of the A1900 Fragment Separator, as calculated with LISE++ [60]. More stable fragments are produced orders of magnitude more abundantly, and their low momentum tails leak into the momentum acceptance of the fragment separator, thus causing an overwhelming background and making decay studies unfeasible. Figure adapted from [55]

select the desired isotopes in the secondary beam and separate them from the more stable low momentum contaminants. At the NSCL, the Radio Frequency Fragment Separator (RFFS) (described in section 3.2) provides this additional purification by applying a transverse electric field to the secondary beam, which causes a vertical deflection of the fragments according to their velocity. A slit downstream of the device eliminates unwanted fragments, leading to beams sufficiently pure for decay studies [55].
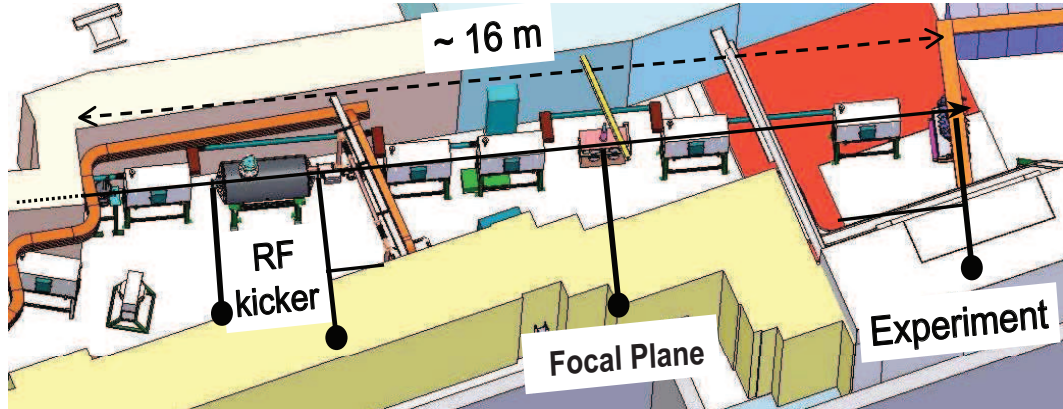
Figure 3.3: The incoming beam enters the RFFS from the left and after filtering it is delivered to the experimental station. All white boxes represent quadrupoles. The collimation slits and diagnostics detectors are located at the RFFS focal plane. Figure adapted from [62].

3.2 Radio Frequency Fragment Separator

As discussed in Section 3.1, a velocity filtering of the mixed rare isotope beam is necessary to improve beam purity for decay experiments. The Radio Frequency Fragment Separator (RFFS) was proposed, designed and built at the NSCL in order to achieve this velocity filtering [55]. The principle of operation of the RFFS is based on the fact that after some distance from the production target, where all ions are produced simultaneously with the primary beam pulses from the K1200 cyclotron, velocity differences between the various ion species translate into a phase difference relative to the cyclotron frequency. Therefore, a transverse radio frequency electric field can be used to cause a phase-dependent deflection, which leads to an effective velocity filtering. The proof of principle had been demonstrated before at RIKEN, where a similar device was constructed and is now operational albeit with a lower purification performance compared to what is required for decay experiments at NSCL [61].

Figure 3.4: Photograph of the RF-kicker, installed in the S1/S2 vaults. The vacuum vessel is a cylindere made of copper-plated steel with an inner diameter of 0.9 m. The beam enters the cavity from the left. The end of the RF guide connected to the RF coupler is visible at the top right. Figure reproduced from [55].

3.2.1 Design

The study of the β-decay of ^{100}Sn was the primary motivation for the construction of the RFFS at the NSCL. Therefore, its performance requirements were aimed at enabling this experiment. Proper correlation of implanted ions and decays requires that an implanted fragment β-decays before another implantation occurs in the same pixel of the implantation detector (see section 3.3.1 for details). To measure half-lives of the order of 1 second and smaller, the average time between implantations should be greater than 10 s. With a detector pixelation of about 1000, this can be achieved by keeping the average implantation rate below about 10 Hz.

Figure 3.3 shows a schematic diagram of the RFFS, installed in the combined S1/S2 vault of the NSCL. The RF-kicker is the most important component of the RFFS. A photograph of the RF-kicker is presented in Fig. **??**, and Fig. 3.5 depicts

RF coupler

Electrodes
(parallel deflecting plates)
1.5m long, 5 cm gap

beam

Fine tuner
(60 kHz of tuning
range)

Capacitive (coarse) tuners: their
distance to the deflecting plates is
adjusted in order to match the RF
frequency of the cyclotrons.

RF electric field:
Maximum peak voltage of 100 kV
Frequency range: 17MHz to 27MHz.
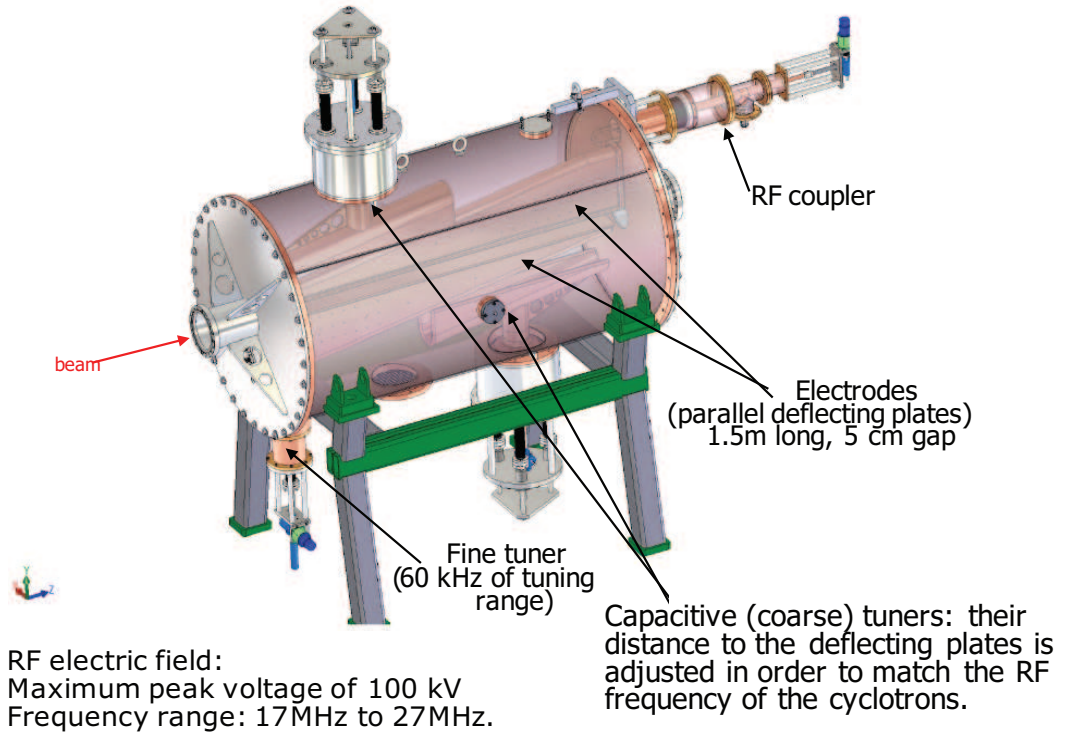
Figure 3.5: Drawing of the RFFS cavity. The interior parts are made of solid copper and steel, and employ a water cooling system. The coarse tuners are adjusted prior to the experiment to match the RF frequency of the cyclotrons, while the fine tuner is used for frequency regulation necessary due to temperature fluctuations while operating the cavity at different voltages.

the inside of the device, which consists of a cylindrical cavity that contains a pair of parallel plates that act as electrodes, in between which a uniform RF vertical electric field is created. The dimensions of the electrode plates are critical parameters in order to obtain the best filtering performance, they are 1.5 m in length, 10 cm wide, and are separated by a 5 cm gap. When a particle of mass m and charge q moving with a velocity v (or alternatively, having a magnetic rigidity $B\rho$) travels through a transverse RF field, it is deflected by an angle Δb given by

$$\Delta b = \frac{V}{B\rho g\omega}(\cos(\phi) - \cos(\omega T + \phi)) \tag{3.2}$$

where V is the sinusoidal voltage across the electrodes, g the gap in between, ω the RF frequency, ϕ the phase difference between the particle and the cavity, and T the time it takes the particle to traverse the field region. Clearly, the maximum

deflection is attained when the particle arrives in phase with the RF field ($\phi = 0$) and it traverses the full cavity in a time T $= \pi/\omega$. The RF-kicker is located 54 m away from the production target, and it is operated at the K1200 Superconducting Cyclotron frequency, which for our experiment was 21.81 MHz, for a primary beam energy of 120 MeV per nucleon. The RFFS was operated at its maximum peak voltage of 100 kV. After traversing the cavity, the beam is transported to the focal plane box, located 5.3 m downstream of the RF-kicker, where a set of vertical slits is used to block out unwanted species. The slit gap and center position settings are adjusted to optimize beam purity and transmission. Once the secondary beam is selected, it is transported further to the experimental endstation. The RFFS focal plane box also contains detectors for beam diagnostics that allow proper tuning of the device. A pair of Parallel Plate Avalanche Counters, one on either side of the selection slits, is used to determine the position of the beam species before and after filtering. The PPACs are followed by a thin plastic scintillator that provides a signal for time-of-flight measurements, and a stack of Si detectors that is used for particle identification. In addition, a re-entry port allows the insertion of a high efficiency Ge detector in order to identify γ-rays emitted by short lived isomers that aid in the particle identification process (see section 4.1).

3.2.2   Performance

The effect the RF-kicker has on the secondary beam is illustrated in Figure 3.6, where the vertical position of the fragments is plotted as a function of the time-of-flight, as calculated with the program LISE++. The positions of the fragments follow the periodic function described by equation 3.2. The phase of the RFFS can be adjusted so as to cause a maximum deflection for the nuclei of interest, while keeping most of the contaminants in a region where they will be blocked by a single slit (represented by the yellow area in the figure), thus limiting the total implantation rate at the experimental endstation. These settings have the additional advantage that, in case
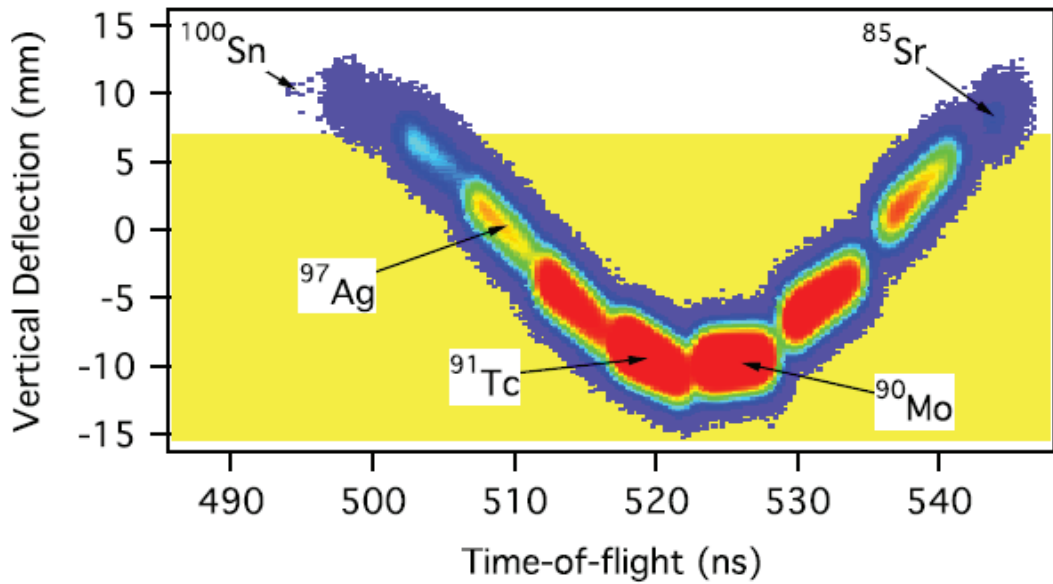
Figure 3.6: LISE++ calculation of the vertical deflection of the secondary beam caused by the RFFS. The vertical position of fragments in the secondary beam is plotted as a function of their time of flight after passing through the RFFS. The yellow band represents a slit to block unwanted fragments. ^{100}Sn and the ions with

the RFFS fails, the full secondary beam will be blocked at the slit, thus avoiding potential damage to the implantation detectors.

The RFFS was commissioned with beam in May of 2007. A primary beam of ^{124}Xe at 140 MeV/u was initially sent directly to the RFFS in order to test the vertical deflection caused as a function of the RF phase of the cavity. During the commissioning run the rf power available was just 6 kW, which generated a 55 kV maximum deflecting voltage. Figure 3.7 shows the vertical position of the ^{124}Xe beam measured at the slit position, as a function of the RF phase. The two curves correspond to different RF voltages, and it can be observed that the deflection follows a sinusoidal and scales linearly with the magnitude of the applied voltage, as expected. A test of the filtering capability of the device then followed. The primary ^{124}Xe beam was therefore impinged onto a ^{9}Be target in order to produce ^{100}Sn and its closest neighbors by fragmentation. The secondary beam was first filtered with the A1900 Fragment Separator and then sent to the RFFS. A few hours were dedicated to finding the optimum production and filtering settings, which then allowed the removal of a large amount
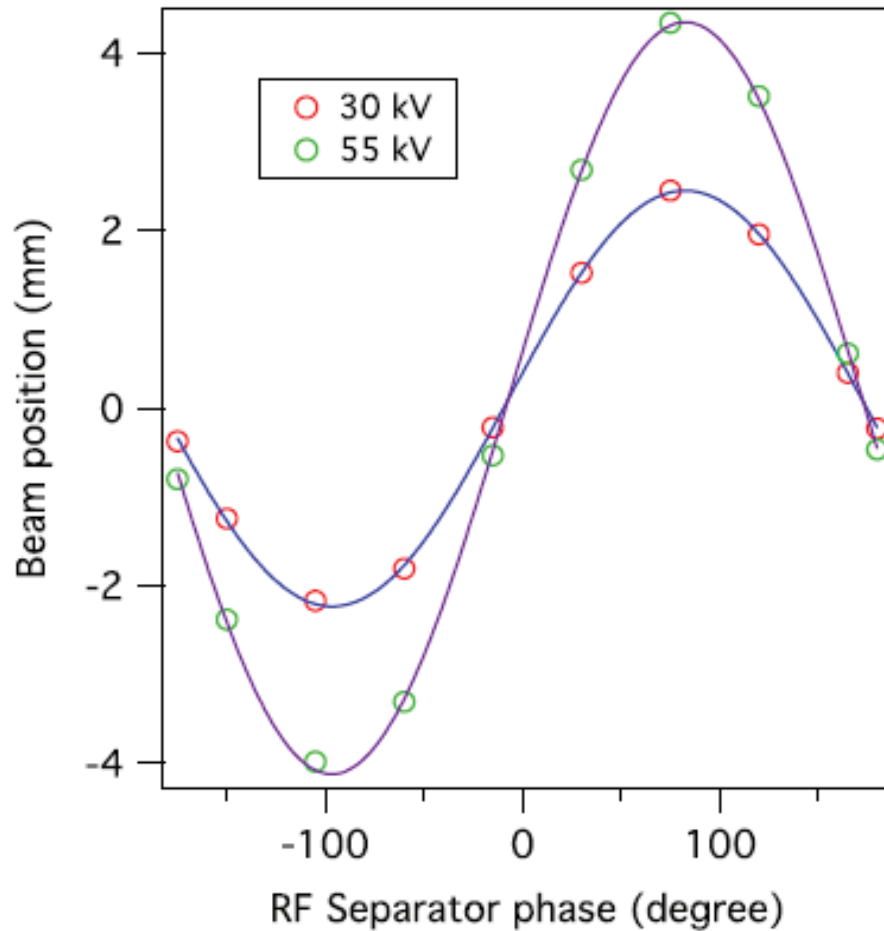
Figure 3.7: Deflection of a primary beam by the RFFS during its commissioning. The vertical position of ^{124}Xe ions is plotted as a function of the RF phase of the cavity. The two curves correspond to different applied voltages. Figure adapted from [55]

of contaminants from the secondary beam (about a factor of 15) and permitted the identification of the exotic $N = Z$ nucleus ^{96}Cd.

Soon after the commissioning run a 50 kW power supply was installed in the RFFS, and the cavity could then operate at its nominal maximum voltage of 100 kV. During EXP07034, the RFFS effectively removed the majority of the most abundant contaminants present in the secondary beam, thus reducing the total rate at the implantation detector by about a factor of 200, to an average of about 50 counts per second. This powerful filtering is evident in Figures 3.8, and 3.9, acquired during preparation runs for ^{100}Sn production. The phase of the RF field was adjusted to let the $N = Z$ heavy ions and closest neighbors pass to the experimental end station.

The left panel of Figure 3.8 shows the particle identification when the slits of the RFFS are completely open. When the slits are closed a large fraction of the undesired species is removed, as shown in the right panel of Figure 3.8, and the overall rate thus becomes acceptable for decay studies. The actual vertical deflection of the fragments is shown in the left panel of Figure 3.9, where the phase was adjusted to push the ions of interest to the lowest position. The majority of the contaminants is then removed from the beam by lowering the upper slit, indicated by a yellow band in Figure 3.9. The contaminants that enter the RFFS cavity in phase with the fragments of interest cannot be removed. They correspond, however, to lower Z isotopes with half-lives of the order of several seconds, which will therefore only contribute to the decay activity as a constant background (see section 4.2 for details). This selective rejection is crucial as it allows us to remove key contaminants while leaving the counting rate of the fragments of interes unaffected.

3.3   Experimental Station

The experimental end station was composed of the NSCL Beta Counting System (BCS) [63] and sixteen detectors from the SeGA array [64]. The BCS included three silicon PIN detectors, used to perform particle identification through energy loss and time of flight measurements. Downstream of the PIN detectors there was a 1 mm thick Double Sided Silicon strip Detector (DSSD) in which the ions were implanted and their decay products (positrons and protons) were detected and correlated with previously implanted ions within time and position windows in order to determine half-lives. Following the DSSD there were six 1 mm-thick Single Sided Silicon strip Detectors (SSSDs) to perform beta calorimetry, and a 1 cm-thick planar germanium detector to veto light particles coming in with the beam. Sixteen high purity Ge detectors from the SeGA array were placed in close geometry around the DSSD in order to measure prompt and β-delayed γ-rays within a predefined time window after

a charged particle triggered the data acquisition.

3.3.1 Beta Counting System

The beta-decay of the fragments of interest was measured with the BCS [63]. The BCS consisted of a stack of three Si PIN detectors (PIN1, PIN2, and PIN3), with thicknesses of 297 μm, 297μm, and 488μm respectively, used to measure energy loss and to provide time signals necessary for particle identification (PID). The thicknesses of the PINs were chosen so as to cause enough energy loss to the nuclei of interest to stop them within the DSSD. The implantation of fragments is predicted by the program LISE++ to occur at a depth between 200 and 300 μm into the DSSD.

The most important component of the BCS was the DSSD, placed downstream of the PIN detectors, a 985 μm-thick Si wafer segmented into 40 1 mm-wide vertical strips on the front, and 40 1 mm-wide horizontal strips on the back, thus effectively creating 1600 individual pixels. The DSSD detects both, implanted ions and their subsequent decays, which are later correlated via software such that half-life information can be extracted. Each of the strips of the DSSD was connected to a dual gain pre-amplifier. The signals amplified with low gain were used to detect implanted ions, which deposit a few GeV of energy. Signals amplified with high gain were used to detect the β particles, which deposit up to a few hundred keV. A master gate signal was generated by a logical OR of the front and back signals of the DSSD, which, together with a computer-not-busy signal provide a master live signal, which in turn starts the data acquisition. Each event is time stamped using a 50 MHz clock and a 32 bit counter providing the capability to determine time differences of events with a resolution of 5.12 μs. Decay times are then determined by subtracting the time of implantation of a fragment from the time of its associated β-decay. Downstream of the DSSD there was a set of six SSSDs, with thicknesses of 975, 981, 977, 989, 988 and 985 μm, respectively, used to perform beta calorimetry and to veto light particles coming in with the beam. The SSSDs are segmented into sixteen strips, and they

were setup so that the orientation of their strips alternated between horizontal and vertical directions. The last element of the BCS was a planar high purity germanium detector used to create a veto for light particles present in the beam. This veto is needed because light particles can be mistakenly identified as beta particles in the DSSD, but as they travel downstream with the beam, they enter the Ge detector, where they deposit much more energy than any beta particle that happens to be emitted towards the downstream direction.

3.3.2 Segmented Germanium Array

Sixteen high purity Ge detectors from the Segmented Germanium Array (SeGA) were used to detect γ rays from the decay of excited states in both implanted fragments and their decay daughter nuclei. Once an implant or a decay event was registered in the BCS, a gate was opened for 20 μs to allow SeGA to detect time and energy of emitted γ-rays. This enabled the detection of microsecond isomeric states in implanted fragments, which aided the particle identification (see section 4.1), and also enabled us to identify new isomers. The detectors were arranged in two rings situated as close as possible to the beamline, and centered around the DSSD. Each detector was read out individually, providing time and energy measurements for each detected transition. The absolute gamma detection efficiency of the array was 6.1% at an energy of 1 MeV, as determined by using calibrated radioactive sources of ^{56}Co, ^{125}Sb, ^{154}Eu, and ^{155}Eu. A picture of the SeGA array around the beamline is shown in Fig. 3.10.

SeGA Energy Calibrations

In order to generate gamma spectra with sufficient statistics for data analysis, the data taken by all SeGA detectors were combined into a single spectrum for each nuclear species. This requires each individual detector to be calibrated in energy, so that all sixteen spectra can be aligned and combined into a single gamma spectrum. With the purpose of monitoring the performance of all SeGA detectors throughout

the experiment, three energy calibrations were performed at different times during the experiment, the first two with a Standard Reference Material source (SRM), which contains ^{125}Sb, ^{152}Eu, ^{154}Eu, and ^{155}Eu, which emit γ-rays in the range of 40 keV to 1500 keV. For the last calibration an additional ^{56}Co source was used to calibrate higher energies. For the calibrations, the data acquisition was triggered with an OR of all SeGA detectors. The peaks in each of the resulting γ spectra were fitted with a Gaussian function using the program Tv [65] and the channel number of each centroid was correlated to the known energy of the emitting source. The energy resolution of all detectors was $\leq$3.5 keV full-width at half-maximum (FWHM) for the 1332 keV transition of ^{60}Co (present as background).

A third order polynomial calibration function relating ADC channel with energy was obtained with this method for each one of the sixteen detectors. Fit residuals were then calculated for all the calibrated spectra as the differences between calibrated and known source energies.

The stability of the energy calibration was monitored using the channel location of the 511 keV peak from positron anihilation that was present in the β-delayed spectra of all Ge detectors. Several such shifts were observed, requiring the use of different calibrations for different detectors and runs. Figure 3.11 illustrates this point and shows the centroid of the 511-keV peak is plotted for detectors 4, 9 and 16 as a function of run number using each one of the three calibrations. For detector 4, for instance, the calibration "4634" works fine througout the entire experiment, yielding the smaller residual. However, that was not the case for detector 9, as can be seen in 3.11b, from run 4190 to around run 4425, the calibration that yielded the smallest deviation of the centroid of the observed 511-keV peak from the actual value was the first one, labeled "4267" in the figure, but starting at run 4425 the best calibration to use is the third one, labeled "4634". The case of detector 16 is also illustrated in Fig. 3.11c, the best calibration for runs 4196 to around 4414 is the first one, labeled "4267", then the "4424" calibration works best, and starting at run 4470 the best

Table 3.1: SeGA energy calibrations implemented in the data analysis of Experiment 07034 according to run number. Detector 2 was excluded from the data analysis due to technical problems.

Det. No.	Cal1 Runs 4196-4414	Cal2 Runs 4415-4424	Cal3 Runs 4425-4469	Cal4 Runs 4470-4659	Cal5 Runs 4600-4632
1	4424	4424	4634	4634	4634
3	4634	4634	4634	4634	4634
4	4634	4634	4634	4634	4634
5	4634	4634	4634	4634	4634
6	4634	4634	4634	4634	4634
7	4634	4634	4634	4634	4634
8	4634	4634	4634	4634	4634
9	4267	4267	4634	4634	4634
10	4267	4267	4267	4267	4267
11	4267	4267	4634	4634	4634
12	4267	4267	4634	4634	4424
13	4634	4634	4634	4634	4634
14	4267	4267	4634	4634	4634
15	4267	4424	4424	4634	4634
16	4267	4424	4424	4634	4634

calibration to use is the third one, labeled "4634". This analysis was done for all 16 SeGA detectors and resulted in five different run-dependent energy calibration files as energy shifts occurred for different detectors at different times. Table 3.1 summarizes the run-dependent SeGA energy calibrations incorporated into our analysis software. It was found that detector 2 showed a poor energy resolution and was therefore not used for data analysis.

SeGA Efficiency Calibrations

The SeGA detectors were calibrated for efficiency using the aforementioned sources prior to the start of the experiment. The calibration sources were placed at the position of the DSSD, and γ-ray spectra were acquired with all detectors for a preset collection time of 3600 seconds. The observed peaks were fitted using the program Tv, and the area, corrected for dead time, was used to determine an observed rate which was then normalized to the known emission rate of the calibration source.

This was done for each individual detector and the results were added to determine the efficiency of the entire array, the errors were added in quadrature. It should be noted here that one of the detectors (Detector number 2 in the electronics) had a bad resolution during many runs, and also shifted in energy too many times, so it was decided not to include it in the total gamma spectrum; therefore the efficiency was determined considering only the other 15 SeGA detectors. The obtained efficiency data as a function of the γ-ray energy, E_γ, were fitted with an empirical formula of the form

$$\epsilon = Ae^{-Bln(E_\gamma - C)}$$

in the energy range of 43 to 3273 keV, and the resulting efficiency curve is shown in Fig. 3.12.

3.4 Rare Isotope Beam Production Settings

The production and separation of doubly magic ^{100}Sn and its closest neighbors has been a major experimental challenge for nuclear physics in the last few decades. However, projectile fragmentation had proven to be a promising production mechanism in previous experiments performed at GSI and GANIL. The first successful identification of ^{100}Sn was achieved at GSI [66], produced from a beryllium target bombarded by a 1095 MeV/u ^{124}Xe beam. Seven events were reported as ^{100}Sn from that experiment. Around the same time, ^{100}Sn was also produced at GANIL [67], from a primary beam of ^{112}Sn accelerated to 63 MeV/u impinging on a nickel target. The production cross section reported from this work was $\sigma \geq 120$(pb). A second attempt at GSI with ^{112}Sn fragmentation on beryllium yielded only one ^{100}Sn identification during 60 hours of beam on target [68].

Low production rates combined with high levels of contamination had hindered detailed decay studies of ^{100}Sn and its closest neighbors at the NSCL. The first attempt

to produce ^{100}Sn at the NSCL (Experiment 01006) utilized a ^{124}Xe primary beam accelerated to 140Mev/u, impinging on a 390 mg/cm^2 ^{9}Be target. Unfortunately, high amounts of contaminants were produced with half-lives of tens of seconds or more, thus preventing attempts to correlate implanted fragments with their subsequent β decays. The measured rate of ^{100}Sn during experiment 01006 was $1.3^{+1.2}_{-0.7} \times 10^{-3}$ pps/pnA for a momentum acceptance of 5%, based on the observation of two ^{100}Sn events.

During the commissioning run of the RFFS (see Section 3.2.2 below), an attempt was made at identifying ^{100}Sn. Two events were identified as ^{100}Sn, but not unambiguously, since only one time-of-flight measurement could be done due to the prohibitively high rate on the A1900 image 2 scintillator. Based on the observed rates for other $N = 50$ isotones (see Fig. 3.13), a production yield of ^{100}Sn was estimated as 7 $\times 10^{-5}$ pps/pnA, derived from the observed maximum rate of ^{99}In, 5×10^{-4} pps/pnA. This estimated rate of ^{100}Sn production was an order of magnitude lower than the one assumed in the proposal for Experiment 07034, of $6.5^{+6.0}_{-3.5} \times 10^{-4}$ pps/pnA for this combination of primary beam (140MeV/u ^{124}Xe at 2 pnA intensity) and target (berillyum).

With an order of magnitude less yield than expected with the ^{124}Xe beam, it was decided to perform the Experiment 07034 with a ^{112}Sn primary beam instead, as it was considered a suitable projectile for ^{100}Sn production according to the 120 pb lower limit established at 63 MeV/u on a nickel target [67].

Targets of both, ^{9}Be and ^{58}Ni (backed with a 47 mg/cm^2-thick ^{9}Be foil) with equivalent energy losses were tested in order to study the effect of the reaction mechanism on the production of $^{101-104}$Sn isotopes and to extrapolate a production rate for ^{100}Sn. This study revealed a higher yield by a constant factor of 5 for the ^{9}Be target [69].

Settings for production and separation of ^{100}Sn, such as Bρ, thicknesses of the wedge and ΔE detectors, as well as RFFS parameters, were calculated with the

program LISE++ [60], and used to set the experiment up. These were chosen to minimize the production of lower charge states without affecting ^{100}Sn production. The very low expected production rate of ^{100}Sn prevented identification of fragments at the A1900 focal plane, due to the long time that would be needed to accumulate sufficient statistics. Therefore, with the purpose of finding the optimum $B\rho$ settings for the production of ^{100}Sn, a momentum distribution scan was done with heavier (and more abundantly produced) Sn isotopes, starting with ^{104}Sn and going step by step down to ^{101}Sn. For each tin isotope setting the beam was implanted in the RFFS focal plane silicon stack, where its rate was measured. The location of the peak of the momentum distribution of each of the $^{104-101}$Sn isotopes was determined by taking five measurements changing the $B\rho$ by 1% each time. The $B\rho$ setting for ^{100}Sn was then extrapolated based on measurements of its heavier siblings, assuming that the production mechanism is similar.

The actual production settings for the neutron-deficient nuclei of our study were therefore: fragmentation of a 120 MeV/u ^{112}Sn primary beam on a 195 mg/cm^2 thick ^{9}Be target, at an average intensity of 10.7 pnA. The secondary beam containing the fragments of interest was selected with the NSCL A1900 Fragment Separator [54], operating in achromatic mode. A 40.6 mg/cm^2 curve-shaped Kapton foil located at the intermediate focal plane acted as an achromatic degrader. The magnetic rigidity $B\rho$ of the first half of the A1900 was set to 2.8802 Tm, and the second half to 2.7701 Tm, past the Kapton wedge. These settings were optimum for centering fully stripped ^{100}Sn fragments, and, in an effort to reduce the intensity of contaminant species, the momentum acceptance of the separator was limited to 1%. The use of this narrow acceptance allowed the separation of neighboring isotopes in the particle identification with a simple time of flight measurement (see Section 4.1). This was convenient in our experiment because the scintillator at the intermediate image of the A1900 Fragment Separator, which is typically used for position measurements, was degraded due to the high intensity of the beam.
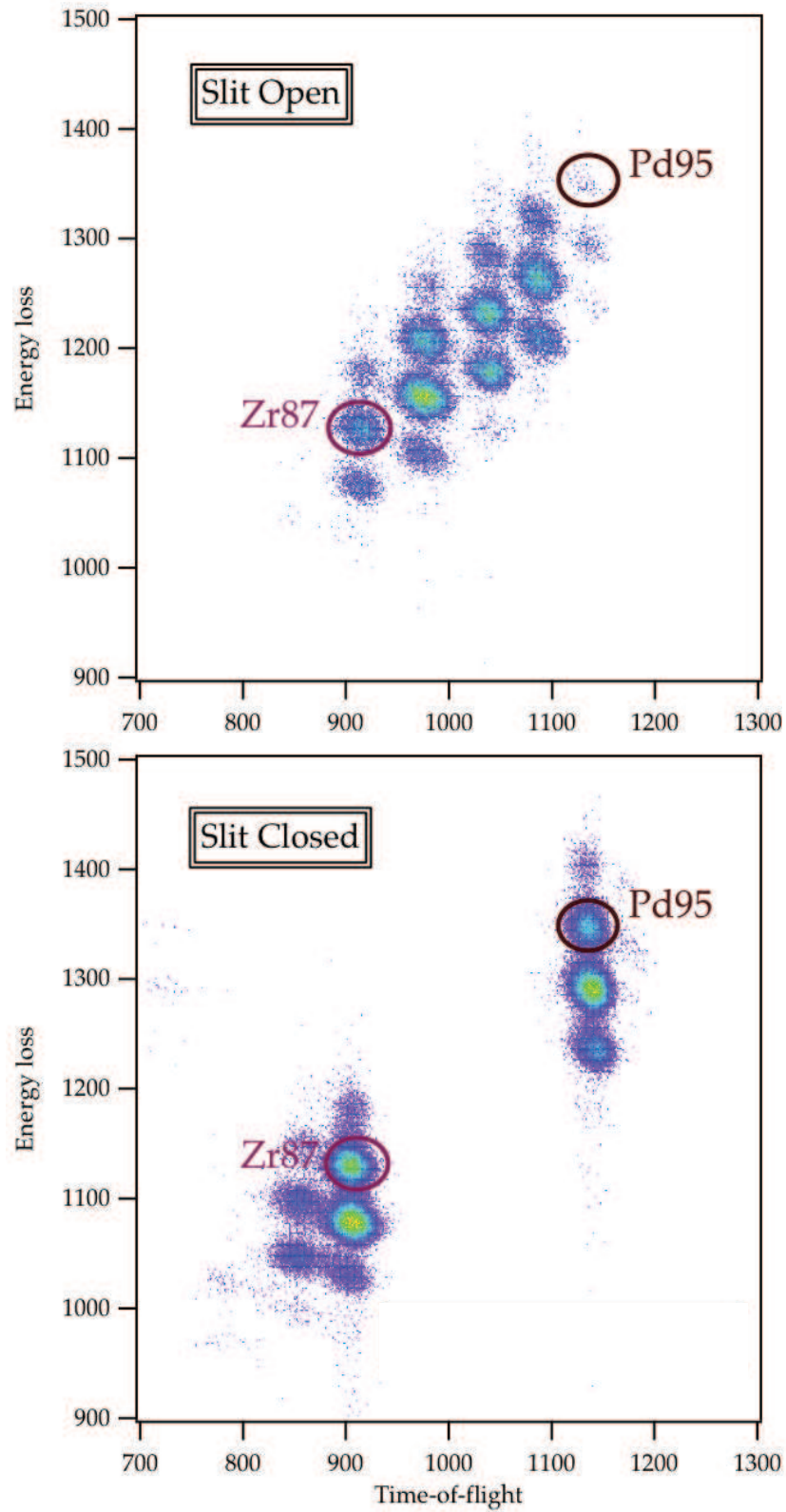
Figure 3.8: Particle identification at the focal plane of the RFFS. In the left panel, the vertical slits used to block out unwanted fragments were open, and in the right panel they were closed. The filtering capabilities of the device are evident, the purification factor achieved was around 200 at the experimental station. Figure adapted from [55]
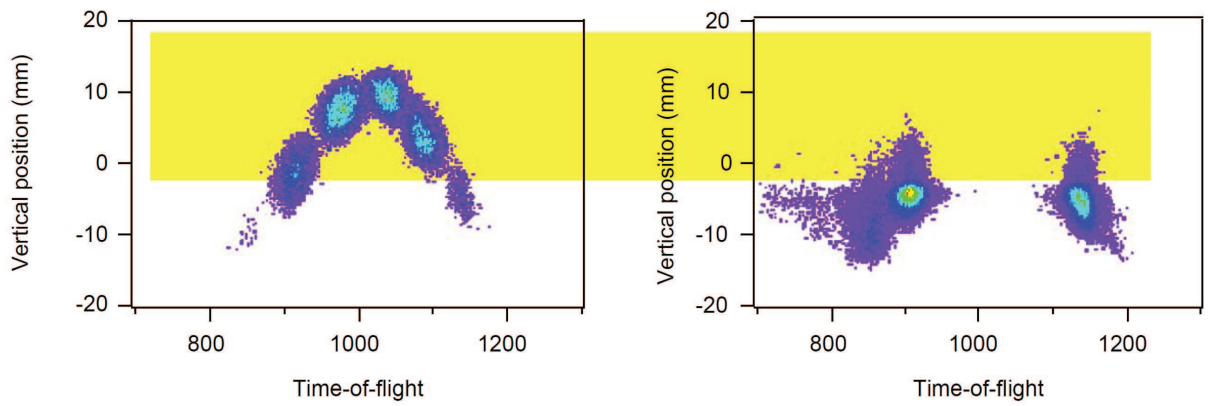
Figure 3.9: Vertical position of neutron-deficient fragments as a function of ToF at the exit of the RFFS. The total number of counts in both spectra are similar, the spectrum on the left was taken with the blocking slits open, and the one on the right was integrated with the slits closed and much more primary beam. Figure adapted from [55]
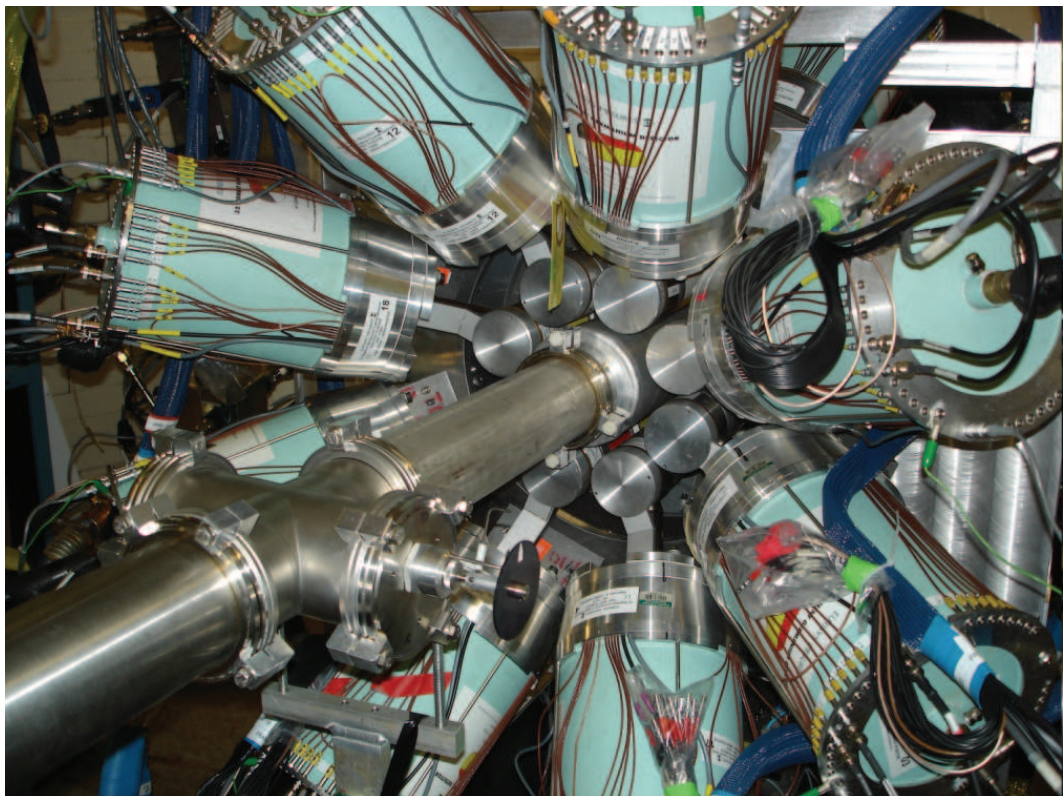
Figure 3.10: Experimental endstation. Sixteen SeGA detectors surrounding the beam line and centered around the DSSD. The beam enters from the left.
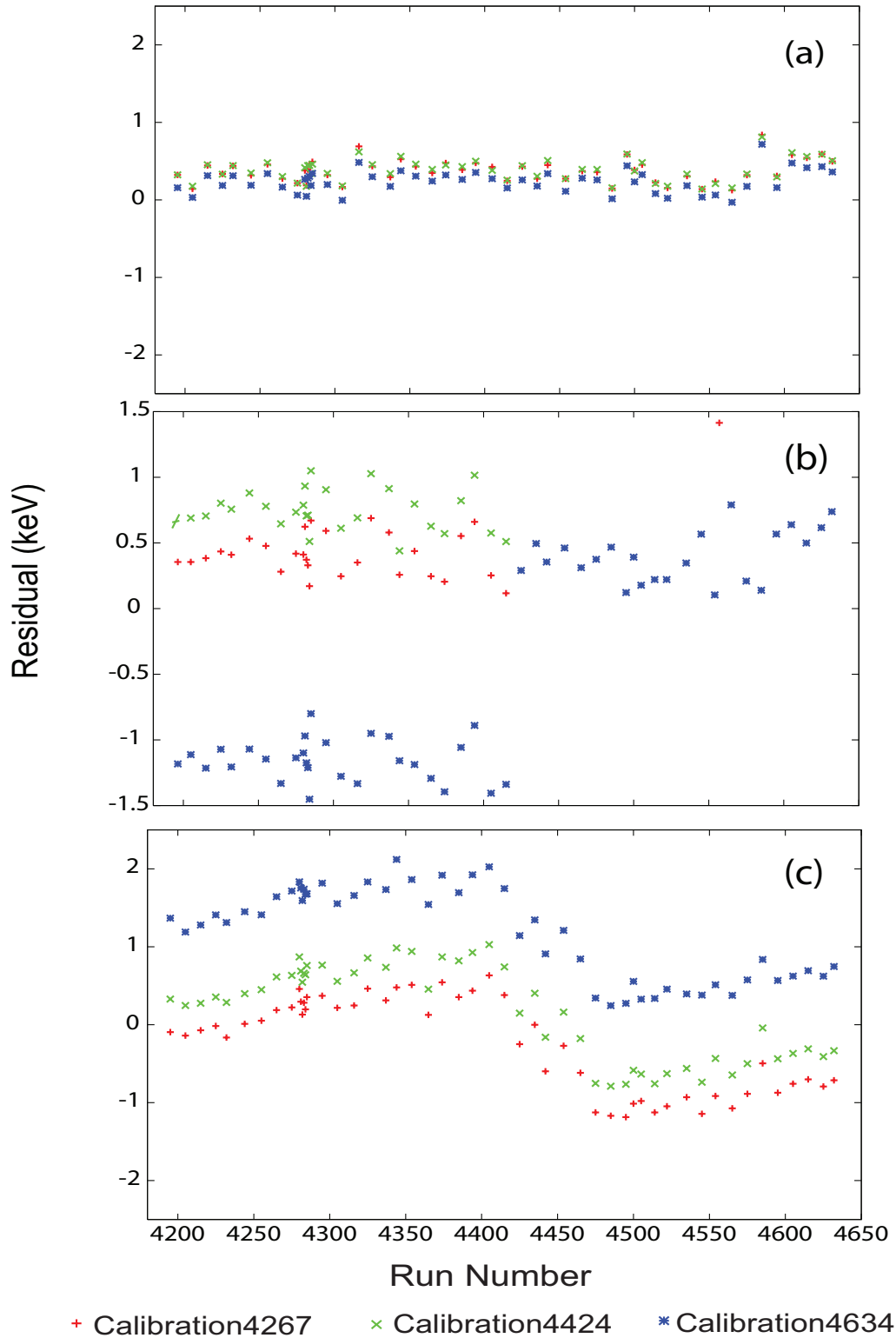
Figure 3.11: Observed energy shifts in SeGA detectors (a) 4, (b) 9 and (c) 16 used in Experiment 07034. The residual from the determination of the centroid of the 511-keV peak is plotted as a function of run number for each of the three energy calibrations performed.
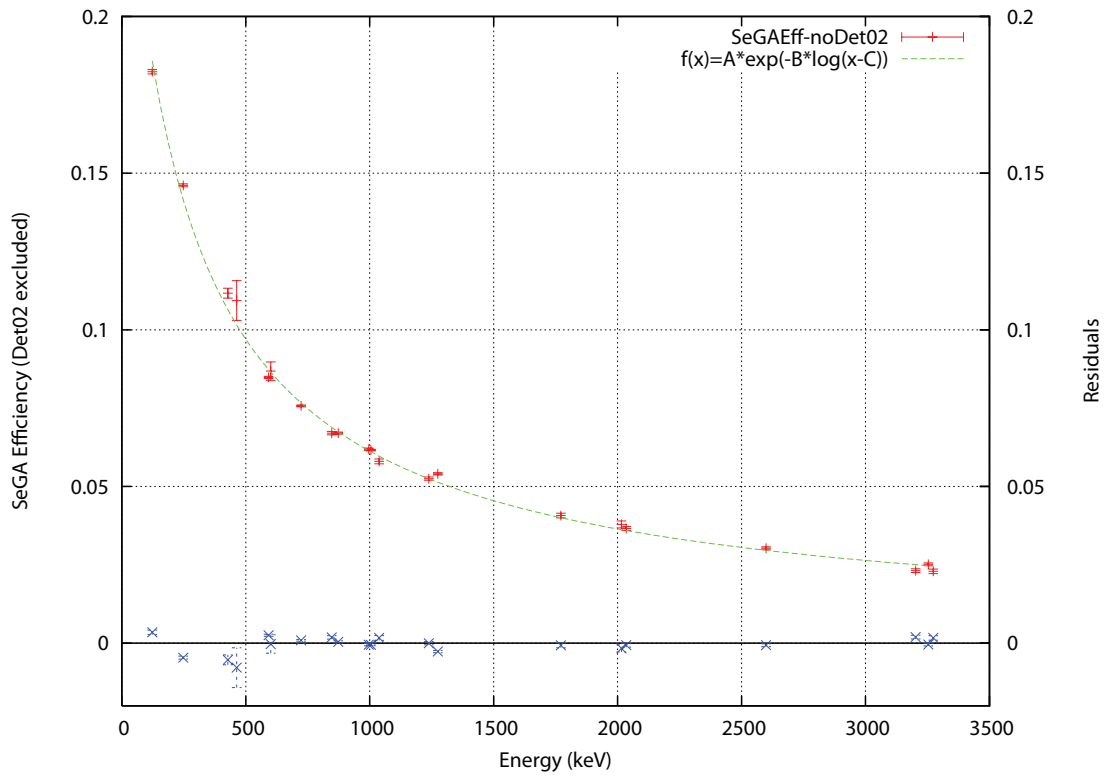
Figure 3.12: γ-detection efficiency for the fifteen SeGA detectors used in the data analysis (Detector No. 2 was excluded because of technical problems). Residuals are shown in bottom panel.
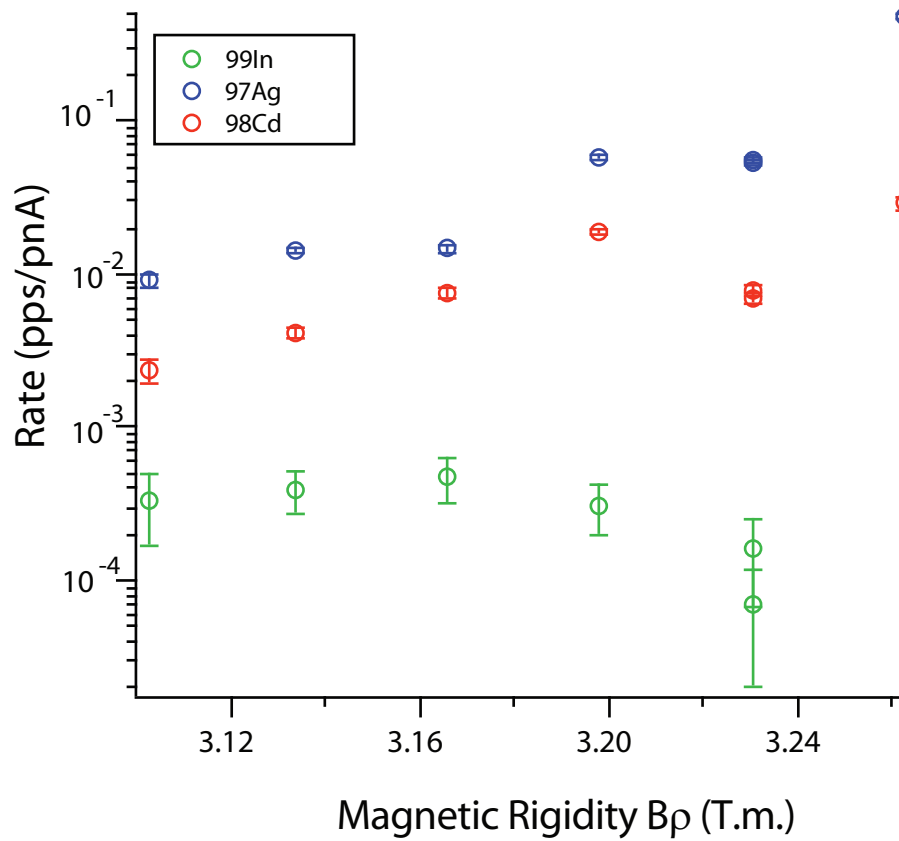
Figure 3.13: Production rates of $N = 50$ isotones obtained from the RFFS commissioning run. The rates (in pps/pnA) are plotted as a function of the magnetic rigidity of the A1900 Fragment Separator. A $B\rho$ scan was performed to find the peak of the momentum distribution of the most neutron-deficient isotopes produced.

Chapter 4

Data Analysis

The present chapter is dedicated to the description of the offline treatment given to the raw data collected during Experiment 07034 in order to extract and interpret structure information about the nuclei of interest. The main goal of this experiment was to investigate the β decay of the doubly magic nucleus ^{100}Sn into ^{100}In. However, as was described in Chapter 3, the beam reaching the experimental station is not 100% pure, rather, it contains a group of nuclear species close in charge and mass to the nucleus of interest, i. e. its neighbors in the chart of nuclei. The following sections describe how these beam impurities are used to our advantage in providing unambiguous particle identification of the most exotic fragments present. Additionally, this gives us the opportunity to obtain new information on the neighboring nuclei that are also of great interest for nuclear physics. These findings are presented and interpreted in Chapter 5.

4.1   Particle Identification

Particle identification was a crucial aspect of our experiment. As described in Chapter 3, detectors installed at suitable points along the beam path are used to measure energy loss and Time-Of-Flight (TOF) of the nuclei present in the secondary beam.

Each nuclear species in the secondary beam is uniquely characterized by its mass and charge. According to the Bethe-Bloch equation, the energy lost by fast ions with charge q and velocity v in matter is given by:

$$-\frac{dE}{dx} = \frac{4\pi q^2 e^2}{m_0 v^2} NB \qquad (4.1)$$

with

$$B \equiv Z_a \left[ln\frac{2m_0 v^2}{I} - ln(1 - \frac{v^2}{c^2}) - \frac{v^2}{c^2} \right]$$

where N and Z_a are the number density and atomic number of the absorbing material, m_0 is the electron rest mass, and e is the electron charge. The parameter I represents the mean excitation energy of atomic electrons in the absorber, and is, in practice, regarded as an empirical constant with a value in eV. Additionally, as $B\rho$ is fixed in the A1900, a measurement of the time-of-flight of the particles over a known distance is a direct way to determine their mass to charge ratio (m/q). Therefore, by independently determining dE/dx and TOF, both the charge and the mass of the ions in the beam can be determined. The fragments produced with the highest yields in our experiment corresponded to fully stripped ions. Charge state contamination, i.e. from lower mass ions with orbital electrons resulting in the same m/q than the fragments of interest, was negligible as such isotopes would be more exotic (i.e. more neutron deficient).

The three Silicon PIN detectors installed at the experimental endstation provided redundant energy loss measurements. Two TOF measurements were made, one was determined from the time difference between a start signal from PIN1 and a stop signal given either by a scintillator placed at the focal plane of the A1900 Fragment Separator (XFP scintillator), or by the cyclotron RF signal. Figures 4.1, 4.3 and **??** show the particle identification spectra obtained with each of the three PIN detectors. As expected, the fragments with the highest atomic numbers had the largest energy loss in each detector. Each blob represents a particular nuclear species, and their

Figure 4.1: Particle identification spectrum obtained with energy loss measurement from the PIN1 detector of the BCS and time-of-flight from XFP scintillator.

widths in time-of-flight are proportional to the momentum acceptance of the A1900 Fragment Separator. The requirement that each implanted particle at the DSSD leaves valid signals in all three PINs is used to clean up the particle identification spectrum at the DSSD. Additionally, the two TOF measurements must be proportioinal to each other, and this proportionality can be used as a cleaning requirement as well.

4.1.1 μs-isomers

Several nuclei in our secondary beam were produced in excited states with half-lives in the microsecond range. A large fraction of them was therefore able to reach the experimental station after about 600 ns of flight path. These long-lived excited states, or isomers, decay mostly by emission of gamma radiation, which we detected with the SeGA array within a few microseconds after their implantation in the DSSD. The decay information from well known isomers was used to confirm the particle

Figure 4.2: Particle identification spectrum obtained with energy loss measurement from the PIN2 detector of the BCS and time-of-flight from XFP scintillator.

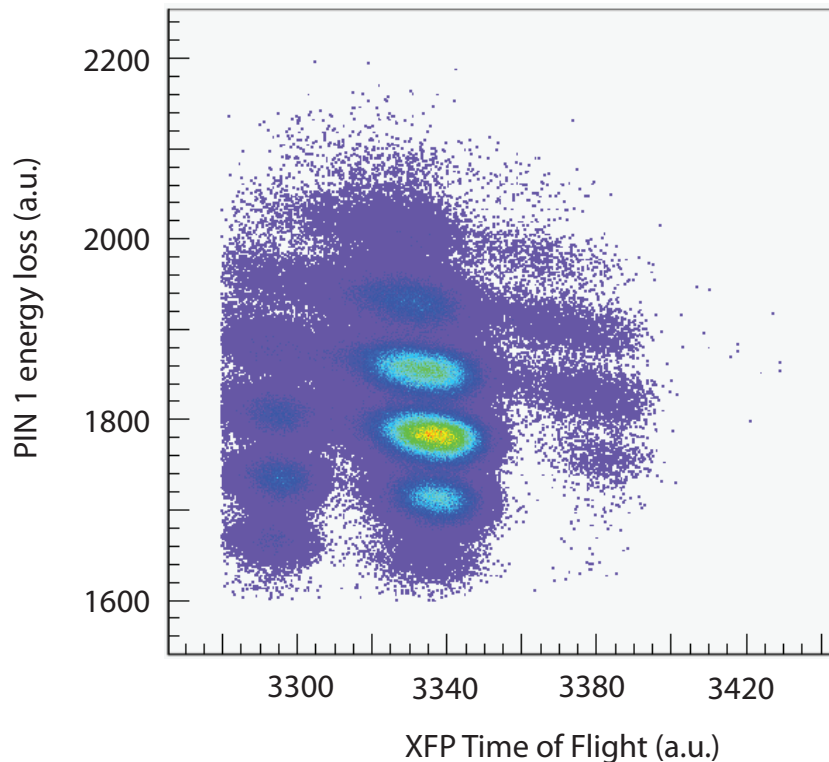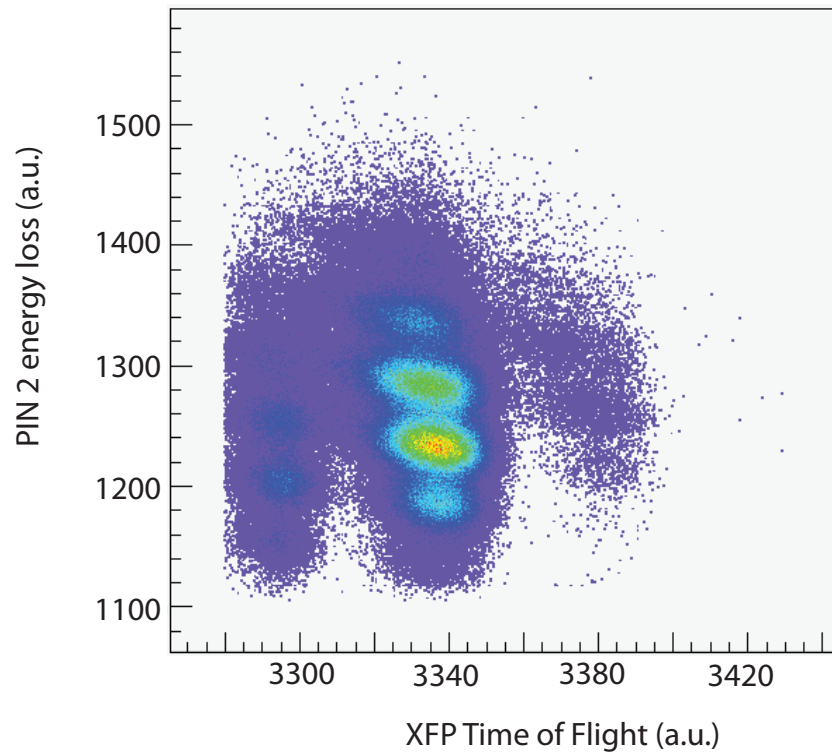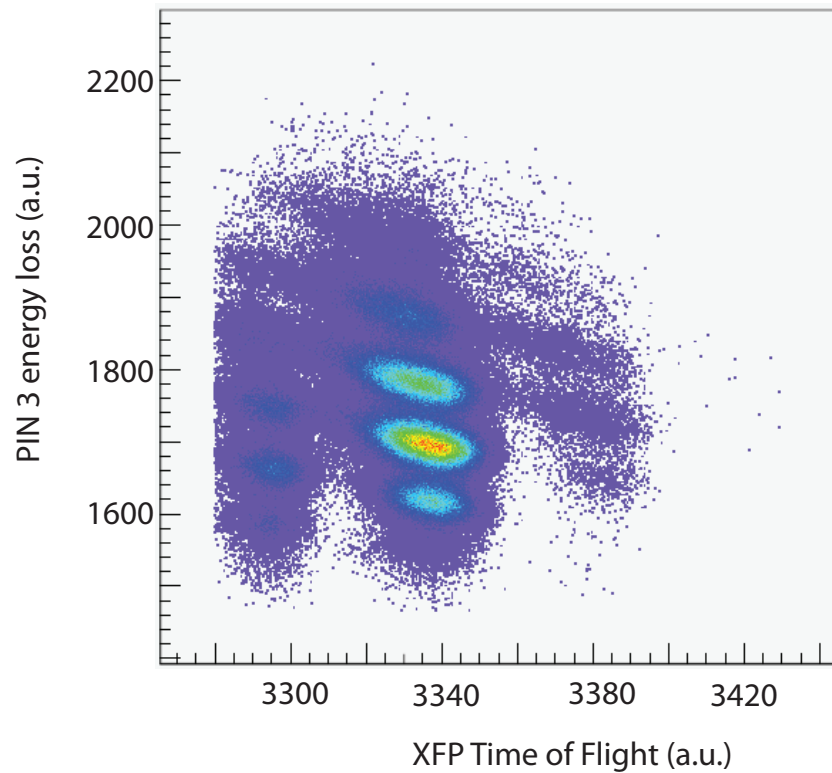Figure 4.3: Particle identification spectrum obtained with energy loss measurement from the PIN3 detector of the BCS and time-of-flight from XFP scintillator.

identification via the γ-ray tagging method [59]. The most abundant isomers detected during runs in which the RFFS slits were open include ^{90}Mo, ^{93}Ru, and ^{96}Pd. When the slits of the RFFS were closed the isomeric decays of ^{88}Zr and ^{94}Pd were used for final particle identification confirmation. A list of the isomeric γ-transitions used for particle identification is provided in table 4.1. Slice gates were made in the SeGA spectrum at the energies of each of the known transitions and were used to gate the ΔE (from PIN1) vs TOF spectrum, and the blob corresponding to the parent nucleus was identified. Then the inverse was done for confirmation, a fragment in the particle identification spectrum was used to gate the SeGA spectrum and the lines corresponding to the correct fragment were clearly observed. The identification of the rest of the isotopes was then done based on their position with respect of the known isomers in the ΔE vs TOF spectrum.

Once the charge and mass of each fragment was unambiguously determined, it was possible to produce the particle identification plot presented in Figure 4.4, with the nuclear charge in the vertical axis, and the mass-to-charge ratio on the horizontal one. This plot does not include the lower Z nuclei which were not eliminated with the RFFS, and that also reached the DSSD. Gates around the centers of each blob were then used to select the data events corresponding to each particular isotope. In the case of the most exotic nuclei of this study, fits applied to the mass spectra were used in an effort to deal with the small contamination from neighboring nuclei. These mass fits were used to determine a probability for the nature of a specific implanted nucleus that was taken into account in the half-life determination in the MLH analysis described below.

Based on the particle identification spectrum of Fig. 4.4, gates drawn around each blob were used to identify each nucleus implanted into the DSSD with its unique time stamp and pixel location. Then, time-stamps files were saved for each isotope so that the analysis could be carried out for each different species independently. The majority of the analysis of this experiment was done using the NSCL data analysis

Table 4.1: Known γ-rays from μs isomers used for particle identification.

Parent nucleus	$T_{1/2}$ (μs)	E_γ (keV)
^{88}Zr	1.320(25)	77.0
		271.8
		671.2
		399.4
		1082.5
		1057.0
^{90}Mo	1.12(5)	809.6
		262.8
		546.7
		1054.1
		948.0
^{93}Ru	2.20(17)	146.3
		544.2
		1392.1
^{94}Pd	0.468(0.019)	95
		324
		659
		814
		905
		994
		1092
^{96}Pd	2.2(3)	106.4
		325.1
		683.8
		1415.4

program SpecTcl, which was modified to read the time-stamp files as input, and then search the corresponding decays in the event files according to the time stamps of interest only.

Isomeric Production Fraction

The isomeric production fraction F is defined as the number of nuclei produced in the isomeric state as a fraction of the total number of nuclei produced for a particular nuclide. Once corrections for decays during the time-of-flight from the production target to the experimental station are taken into account, the isomeric production fraction can be determined from the number of implanted nuclei and the number
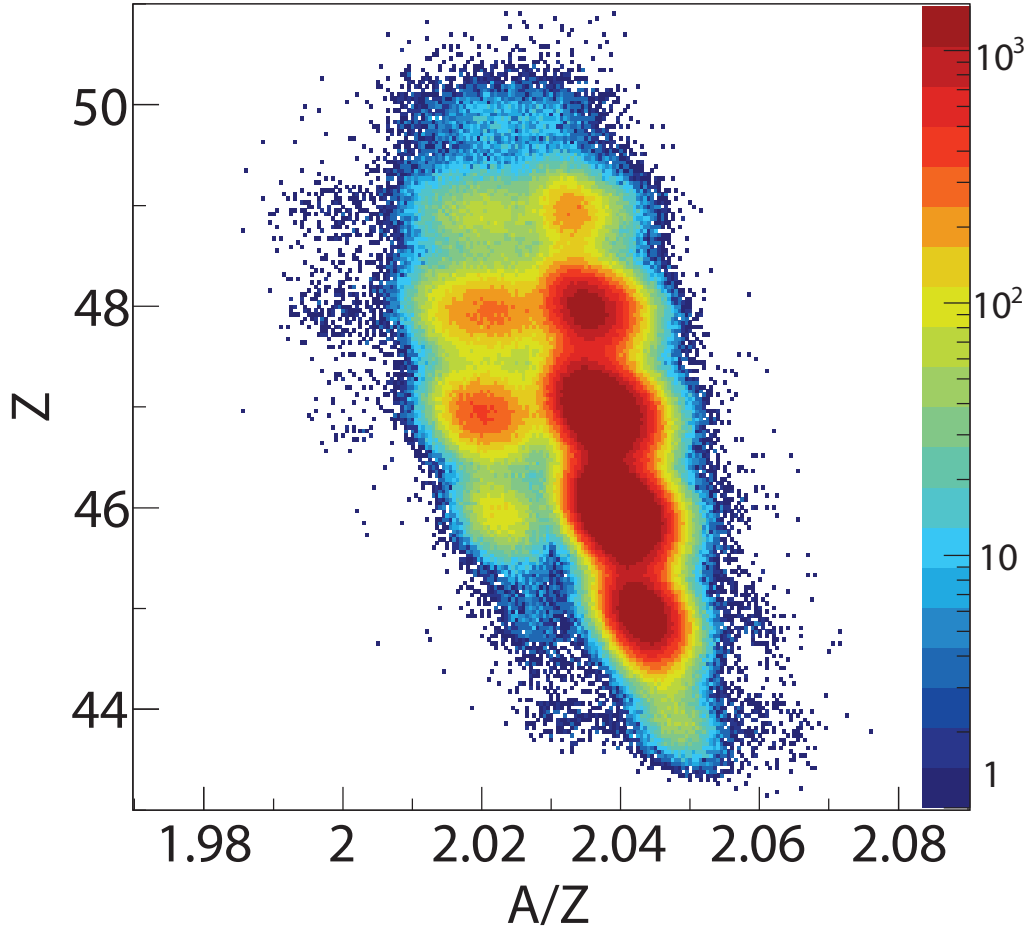
Figure 4.4: Particle identification spectrum of the heavy nuclei implanted in the DSSD. The low-Z contaminants are not shown in this figure. Figure adapted from [69]

of those implanted in their isomeric state. The number of nuclei implanted in the isomeric state was estimated (following the procedure outlined by Daugas *et al.* [70]) from the number of counts in the observed γ-ray transitions, after correcting for the relative γ-ray intensities inferred from the decay scheme and the photopeak efficiencies. A correction for decays occurring during the time-of-flight requires knowledge of the decay half-life. This half-life can be different from the measured isomeric decay half-life of the ions implanted in the detector as during flight ions are fully stripped and therefore decay by electron conversion cannot occur. For neutron-deficient nuclei, a correction for the suppression of electron capture and, more importantly, of electron conversion decay must therefore be applied. The following equation was used to

calculate the isomeric fractions reported in this work [70]:

$$F = \frac{N_{\text{isom}}}{N_{\text{ions}}} \exp\left[\ln(2)\frac{T_{\text{TOF}}}{\gamma T_{1/2}^{Q}}\right] \qquad (4.2)$$

where N_{isom} is the number of detected isomers and N_{ions} the number of implanted nuclei with mass A and atomic number Z, T_{TOF} is the time-of-flight of the nucleus from the target to the DSSD, $T_{1/2}^{Q}$ is the half-life of the isomer for charge state Q, and γ is the relativistic factor. For fully stripped ions:

$$T_{1/2}^{\text{Q=Z}} = T_{1/2}^{\text{Q=0}}(1 + \alpha_{\text{total}}) \qquad (4.3)$$

where α_{total} is the total internal conversion coefficient.

4.2   Fragment - Decay Correlations

All the events registered in the DSSD were classified as either an implanted fragment or a β particle based on thresholds established via software on the various detectors of the BCS. An event was classified as an implantation when it produced a signal above threshold in PIN1 (which ensured that the particle was a heavy ion in the secondary beam), and signals above threshold in the low gain channels of the front and back strips of the DSSD. The implantation pixel was therefore defined as the intersection of the front and back strips in which the low-gain signals were maximum. A β particle was identified as an event that did not produce a valid signal in PIN1, but with signals above threshold in the high gain channels of the front and back strips of the DSSD. Additionally, some light particles that may come with the secondary beam are discarded by setting an upper threshold in the signals from the SSSDs and on the planar Ge detector.

The correlation of a decay with its coresponding parent was done in software using the time and position information of each event. The specific time and position

correlation settings used in the analysis of each nuclear species varied depending on the half-life of the parent, the background rate, and the information sought. The fragment-decay correlation in position was performed with a correlation area larger than a single pixel to account for β particles that deposit only a small fraction of their energy in the implantation pixel but that pass through a neighboring pixel, and also to account for uncertainties in the determination of the implantation pixel. It will be shown below that the β-detection efficiency scales with the size of the area chosen for implant-decay correlations, but so does the amount of false implant-decay correlations (background). A study to determine the ideal efficiency-background compromise was performed, and the results are shown in Fig. 4.5. It was found that a 5-pixel correlation area consisting of the implantation pixel plus its four nearest neighbors was optimum, and such a geometry was used to determine the β-decay half-lives of the $N = Z$ nuclei ^{96}Cd, ^{98}In, and ^{100}Sn. For most other nuclei the statistics were high enough to allow the use of a single pixel for correlation, at the cost of lower β-detection efficiency in favor of a lower amount of background.

A decay and a fragment correlated in position were also correlated in time if they both occurred within a time window of about 10 (estimated) half-lives of the parent nucleus. Making the correlation time larger only adds background to the decay curve, wich however, can be useful to the fit, since by fixing the background level the number of free parameters decreases.

The production rates of the very exotic $N = Z$ nuclei was the lowest of all. Therefore, in an effort to minimize the wrong correlation of their decay products to other, more recent, implanted ions, a "Beam Off" gate was implemented, which, upon detection of an implanted ion in a predefined area of the particle identification spectrum of PIN1 vs PIN1.RF time-of-flight, dephased the cyclotron RF for 5 seconds, preventing the beam from reaching the DSSD.

4.2.1 Determination of β-decay Half-lives

The β decay half-lives of the implanted nuclei were determined using two different methods, both of which assumed Poisson statistics, but differed in the treatment of data. The methods were chosen based on the number of fragment-decay correlations observed for each particular isotope. For the cases with high statistics, the differences in time between the implantation of the fragment and its correlated decay events were binned into Δt intervals, from zero to the maximum correlation time. The resulting decay curve was then fitted with the ROOT Minuit least-square minimization procedure that determines a constant level of background and the decay constant of the parent nucleus, considering the activities of the parent, daughter, and grandaugther nuclei according to the Bateman equations for nuclear decay. In the Bateman equations the activity of the nth member of the decay chain is given in terms of the decay constants of all preceeding members [47]:

$$A_n = N_0 \sum_{i=1}^{n} c_1 e^{-\lambda_i t} \tag{4.4}$$

Necessary input parameters for the ROOT fitting routine were the desired bin size, daughter and grandaughter half-lives, and initial guess values for the parent decay constant, initial activity, and background level. The β-decay half-life curves are presented in the next chapter.

For the most exotic nuclei of this study, the statistics was too low for the above method to be effective in the half-life determination. Therefore, a Maximum Likelihood (MLH) method was applied, which used all of the information available, event by event, to find the parent decay half-life that maximized a joint probability density called the likelihood function. Inputs to the MLH are daughter and grandaughter half-lives, background rate and β-detection efficiency. The probability density function for up to three decay events within the correlation time window is calculated taking into account all possible scenarios leading to the observation, including back-

ground events [71]. The determination of the half-lives for the $N = Z$ implants was then performed by calculating the likelihood for the observed event sequences as a function of assumed parent half-life. The maximum of the likelihood function corresponded to the decay half-life. The width of the likelihood function is then used to estimate error bars.

β Detection Efficiency

The β detection efficiency of the DSSD (ϵ_β) was determined from the fit to the decay curves of isotopes with high statistics and known half-lives, such as ^{93}Pd, ^{95}Ag, ^{96}Ag, and ^{100}In. The fit allows the calculation of the total number of parent decays N_d, which, compared to the total number of implanted nuclei N_i, yields ϵ_β.

$$\epsilon_\beta = \frac{N_d}{N_i} = \frac{A_0 T_{1/2}}{N_i \Delta t \ln 2} \tag{4.5}$$

where A_0 is the number of counts in the first bin, $T_{1/2}$ the half-life determined from the fit, and Δt the bin size of the histogram. The average β efficiency of the DSSD was 37(2)%, using a 5-pixel correlation area. Since the energy loss of the β particles in the DSSD is only a few hundred keV (i.e. only a small fraction of their energy), it was assumed that the efficiency is independent of the Q_β value and therefore the same for all nuclides. This was confirmed by comparing the efficiencies obtained for ^{95}Ag, ^{97}Cd, ^{98}Cd.

β Background

A large number of decays ocurred at any given time all over the DSSD, which resulted in incorrect fragment-decay correlations. Therefore, the decays assigned to the incorrect fragment become a source of background in the implant-decay histograms. As the vertical deflection caused by the RFFS to each particular fragment depended on its time-of-flight, each nuclear species was implanted in slightly different overlap-

ping regions of the DSSD. Therefore, the resulting β-decay background was isotope-dependent.

For the exotic $N = Z$ nuclei, the background was determined from the history of implantations in each pixel of the DSSD. A background rate was then calculated by summing the background contribution from each isotope implanted in that pixel, provided their half-lives were known.

For the species observed with high statistics, the background was determined from the fits to their decay curves. By allowing a sufficiently long correlation time, it was possible to clearly observe most of the decay of the parent nucleus, until the remaining activity could be assigned to background, which was constant over the observation period.

4.3 Prompt γ Radiation Measurement

As described in section 4.1.1, our experimental setup allowed the detection of γ-rays from isomeric states within a window of around 12 μs after the implantation of the parent nucleus. We call these γ-rays prompt. For each isotope in our particle identification, a total prompt γ-ray energy spectrum was constructed in SpecTcl by combining the energy-calibrated spectra from the fifteen SeGA detectors. Such spectra were analyzed using the program Tv [65], where the γ-rays peaks were fitted with Gaussian distributions for the case of high statistics, and with Poisson distributions in the case of low statistics. Tv outputs centroids, FWHMs and peak areas, with their respective uncertainties. Relative γ-ray intensities were obtained by correcting the peak areas for the efficiency of the SeGA detectors, and normalizing them to 100 for the most intense peak.

When an isotope emits multiple cascade γ rays in its decay, additional peaks may appear in the recorded spectrum. If no isomeric states are involved, the lifetime of the intermediate state is generally so short that the two γ rays are, in effect, emitted
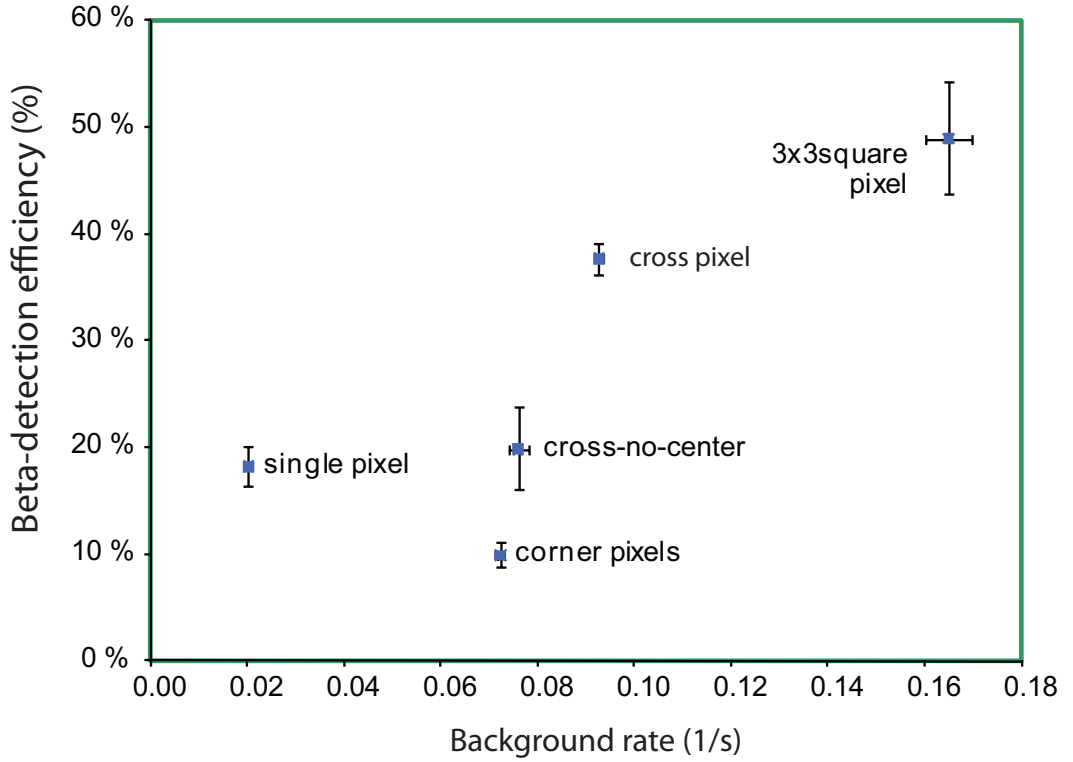
Figure 4.5: β-detection efficiency of the BCS as a function of the amount of background observed. The labels indicate the correlation pixel considered in each case: single-pixel means that both, implant and decay were detected in the same pixel; cross-pixel refers to the implantation pixel plus its four nearest neighbors; 3×3 square means a 9-pixel area centered around the implantation pixel; corner-pixels refers to the four corner pixels of the 3×3 square pixel; and cross-no-center pixel means the 4 nearest neighbors, without considering the implantation pixel.

in coincidence. It is then quite possible for both γ-ray photons from a single decay to interact with the material of the detector and deposit all their energy within a time that is short compared with the response time of the detector or the resolving time of the following electronics [72]. If enough of these events occur, a sum coincidence peak will be observable in the spectrum that occurs at a pulse height that corresponds to the sum of the two individual γ-ray energies. A continuum of sum events will also occur at lower amplitudes due to the summation of partial energy loss interactions.

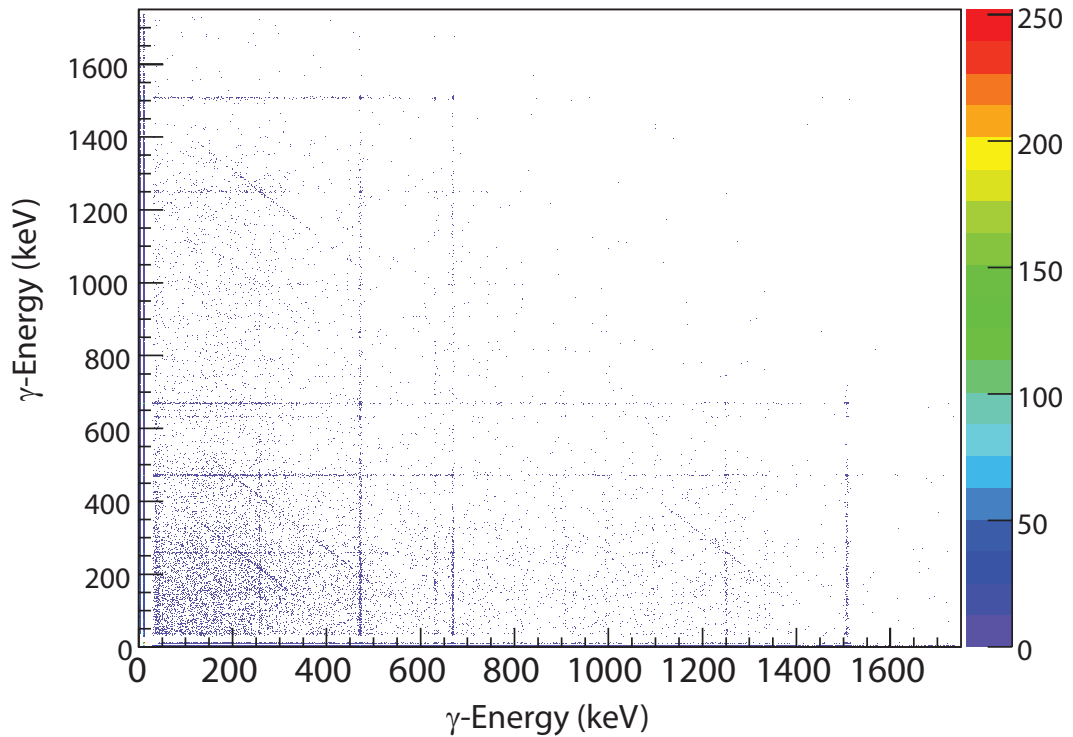Two-dimensional matrices of prompt γ-ray energies were constructed in order to

Figure 4.6: Two-dimensional matrix of prompt γ-ray energies measured with SeGA for the ^{96}Ag implants. A cut around an energy of interest in each axis is projected along the opposite one in order to extract $\gamma\gamma$ coincidence information.

study the coincidence relationships of the observed transitions. One example of such matrices is shown in Fig. 4.6 for the case of ^{96}Ag. One-dimensional projections of each matrix were done at the energies of interest in both, horizontal and vertical axes, then the pair was added in Tv to obtain a $\gamma\gamma$ spectrum for each transition. Relative intensities and coincidence relationships obtained this way are the usual method utilized in the construction of decay schemes, as will be explained in more detail in the next Chapter.

Isomeric half-lives can be determined from a two-dimensional matrix of the prompt γ-ray energies vs time, like the one presented in Fig 4.7. The time between implantation of a fragment and its subsequent γ emission was measured by a time-to-amplitude converter (TAC), started by an master gate (MG) Live signal, and stopped by an OR of all SeGA detectors. A cut around the energy of the transition of interest was pro-

jected into the time axis in order to obtain a decay curve, which was then fitted with a single exponential component and a constant background. The SeGA-TAC spectrum shows a large amount of counts at early times due to the overload of the germanium detectors from X- and γ-rays created when the heavy ions are implanted in the silicon detector, therefore all of the μs-isomeric decay curves were fitted starting at around 1.5 μs, ignoring data at earlier times.
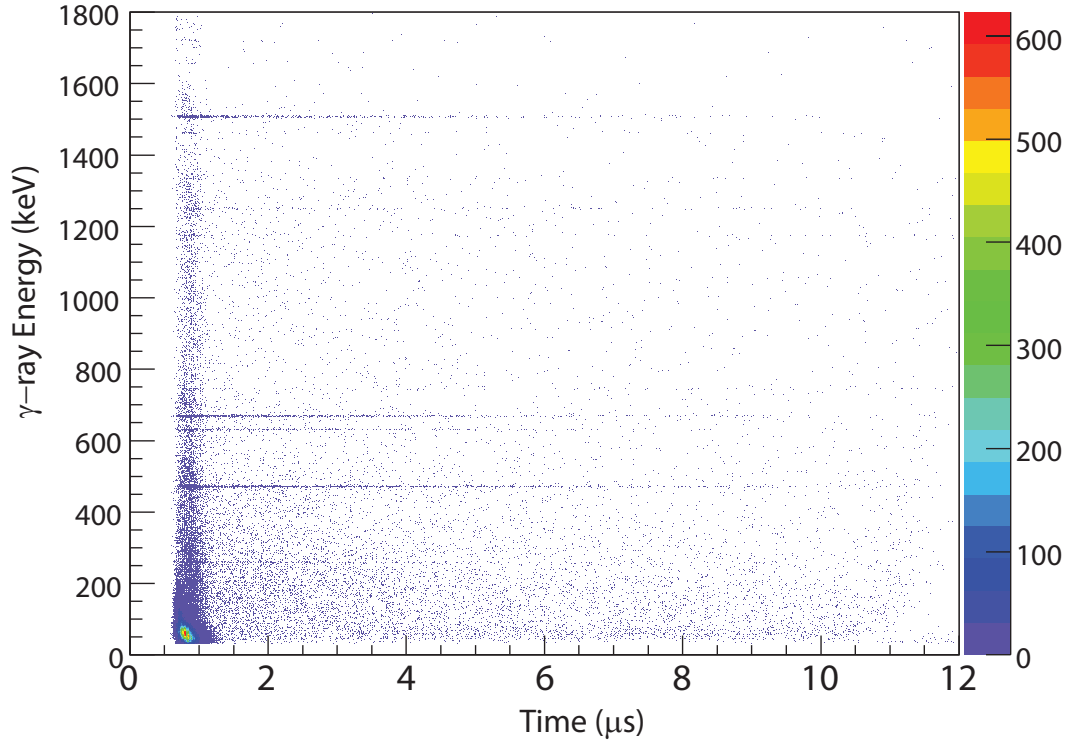
Figure 4.7: Two-dimensional matrix of prompt γ-ray energies measured with SeGA as a function of time in the SeGA TAC. This spectrum was generated for the ^{96}Ag fragments implanted in the DSSD. A cut around an energy of interest in the energy axis is projected along the time axis in order to construct a decay curve for that γ transition.

4.4 β-Delayed γ Radiation Measurement

Following β-decay, some nuclei reach an excited state of the daughter nucleus, which is quickly de-excited by the emission of γ-rays. These γ-rays are therefore referred to

as β-delayed, and are typically emitted with the half-life characteristic of the β-decay of the parent. Since these γ transitions uniquely identify a parent decay, they can be used to determine decay curves and half-lives free of contamination from random correlations with other isotopes or daughter decays, although with reduced statistics, due to the limited γ-ray detection efficiency.

Fragment-$\beta - \gamma$ coincidence spectra were obtained for all isotopes in our particle identification, and they were analyzed in the same way as the prompt γ spectra described above in order to extract $\gamma\gamma$-coincidence information.

Chapter 5

Experimental Results

Fourteen exotic neutron-deficient nuclei were studied in Experiment 07034. As described in previous chapters, the region in the chart of nuclides close to ^{100}Sn is characterized by the occurrence of high-spin isomers. Several such long-lived excited states were observed in our experiment and they are presented in the following sections. Diverse decay modes were identified in this study, namely γ, internal conversion, β or β-delayed proton emission. Results on β-decay half-lives, and prompt and β-delayed γ spectroscopy are presented in the current chapter, along with the interpretation of the results in terms of the underlying nuclear structure. The possible implications of our results on the astrophysical rp-process are discussed in Chapter 6.

5.1 $N = Z$ Nuclei

The particle identification plot presented in Fig. 4.4 represents the accumulated statistics for the most exotic nuclei produced in Experiment 07034. Experimental results are presented in this section for the $N = Z$ nuclei ^{96}Cd, ^{98}In and ^{100}Sn. The β-decay half-life of ^{96}Cd was determined in this work for the first time, and its possible consequences on the production of mass $A = 96$ in the rp-process explored. The β-decay half-lives of ^{98}In and ^{100}Sn had been measured previously, and the results obtained in

the present study are in agreement with those measurements.

5.1.1 ^{96}Cd

^{96}Cd was first observed at the NSCL during the commissioning run of the RFFS in May of 2007, produced by fragmentation of a primary beam of ^{124}Xe impinging on a 188 mg/cm^2 ^{9}Be target at an energy of 140 MeV/u. The particle identification spectrum is presented in Fig. 5.1, with ^{96}Cd marked in the upper right corner. The particle identification was confirmed through observation of known γ transitions from the de-excitation of a microsecond (μs)-isomer in ^{94}Pd. The experimental setup during the RFFS commissioning was not suited for β-decay studies. The measurement, nevertheless, allowed us to unambiguously identify eighteen ^{96}Cd events and to determine the production rate of ^{96}Cd as $2.03 \pm 0.48 \times 10^{-4}$ pps/pnA for these production settings. A lower limit for the half-life of ^{96}Cd was estimated at around 475 ns, based on the time-of-flight of the fragments from the target position to a Si PIN detector installed at the RFFS focal plane.

During Experiment 07034, 274 (24) implantation events of ^{96}Cd were registered at the DSSD. β-decays occurring within the implantation pixel and its nearest neighbors within 10 seconds of a ^{96}Cd implantation were correlated to the fragments. The time distribution of observed decay events within the 10 seconds of correlation time is shown in Fig. 5.2. The time axis was plotted on a logarithmic scale with the intention to improve the visualization of different decay components, in case more than one was present. The event rates of decays plotted on a logarithmic time scale show a bell-shaped distribution peaked around the mean life time [73]. Thus, when two or more decay components are present and their half-lives differ by at least an order of magnitude, such logarithmic plot will show the corresponding decay curves clearly separated.

There is a long-standing shell model prediction of a β-decaying 16$^+$ spin-gap isomeric state in ^{96}Cd with a half-life of 0.5 s [1, 42]. The time distribution of ^{96}Cd
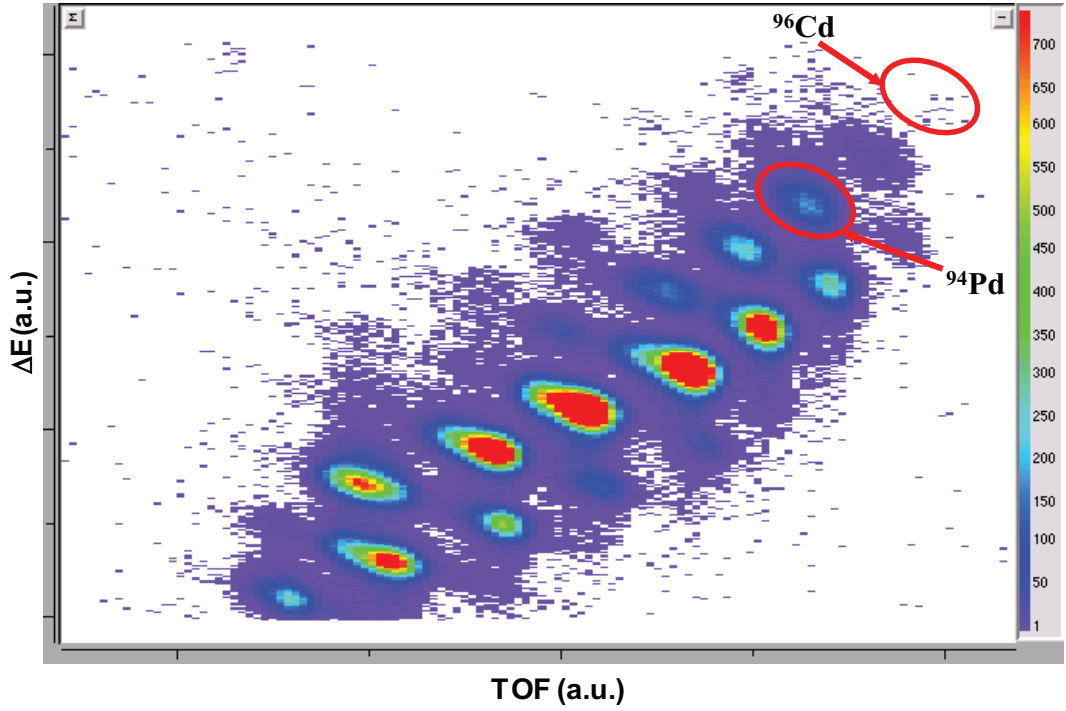
Figure 5.1: Particle identification spectrum from the RFFS commissioning run. Nuclei in this plot were produced by fragmentation of a primary beam of ^{124}Xe at 140 MeV impinging on a beryllium target. Shown are ion energy-loss in a silicon detector versus time-of-flight. The particle identification was confirmed by the observation of known isomeric γ-rays, such as those of ^{94}Pd.

decays, however, does not show an indication for more than one component (Fig. 5.2). A maximum likelihood analysis was implemented in order to estimate the decay constant of the ^{96}Cd data. The resulting likelihood function is also displayed in Fig. 5.2, and it reaches its maximum at the value corresponding to a half-life of $1.03^{+0.24}_{-0.21}$ s. For this analysis, the time distribution and intensity of the expected background for each individual ^{96}Cd event was predicted from the implantation history in each pixel and the known half-lives of the implanted nuclei and their decay daughters, resulting in an average rate of 0.1 s^{-1} over the 10 seconds of correlation time (see Section 4.2.1 for a description of the determination of β-decay half-lives).

As a cross check, a binned decay curve of ^{96}Cd was fitted based on the maximization of a Poisson probability log-likelihood function. The fit is presented in Fig. 5.3, and considered the decay of the parent and daughter plus a constant background. The half-life of ^{96}Cd obtained with this method is 0.8 ± 0.36 s, consistent with that
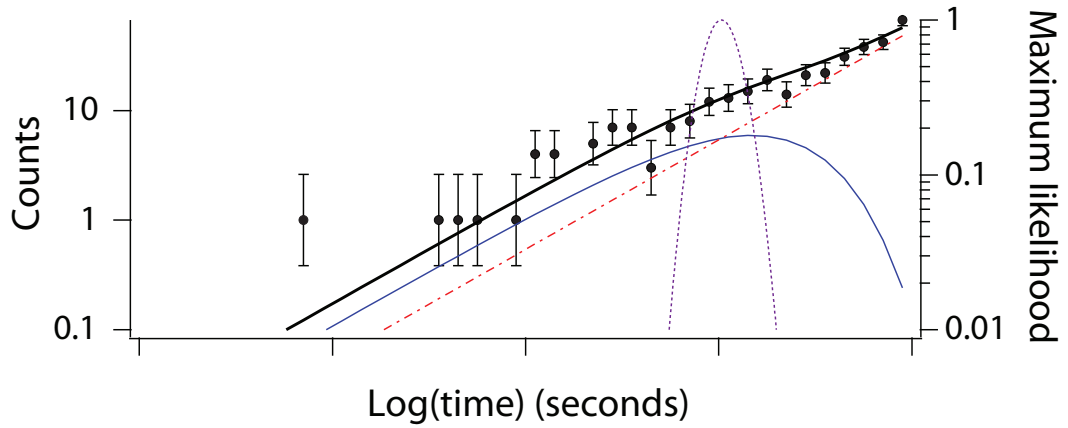
Figure 5.2: Number of decays observed for ^{96}Cd as a function of logarithmic time. The fit shown was obtained through a MLH analysis, and includes the contributions from the decay of the daughter and contaminant nuclei. The blue curve peaks around zero, which corresponds to a half-life of 1 second. The background is observed as a straight line (dot dashed red line), and was calculated as a function of time and pixel position. The likelihood function is also shown (dotted curve), with its scale on the right-hand side. Figure reproduced from [69].

Figure 5.3: β-decay curve of ^{96}Cd, obtained within a correlation time of 10 seconds. The fit is the result of the maximization of a Poisson distribution log-likelihood function. The curve labeled "Total" is the result of the sum of the Bateman equations corresponding to contributions from the parent and daughter decay, in addition to a constant background.

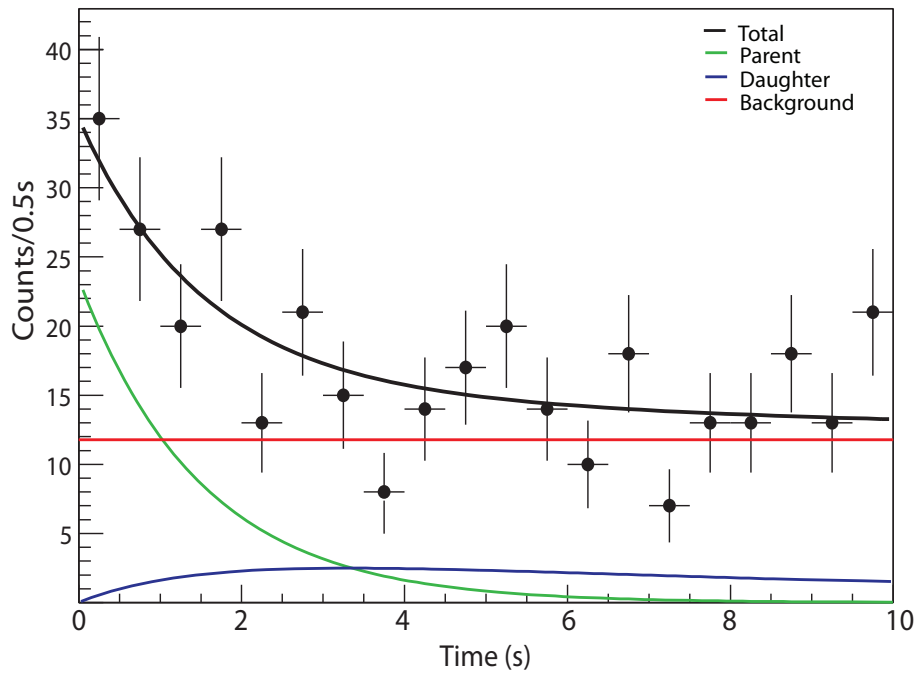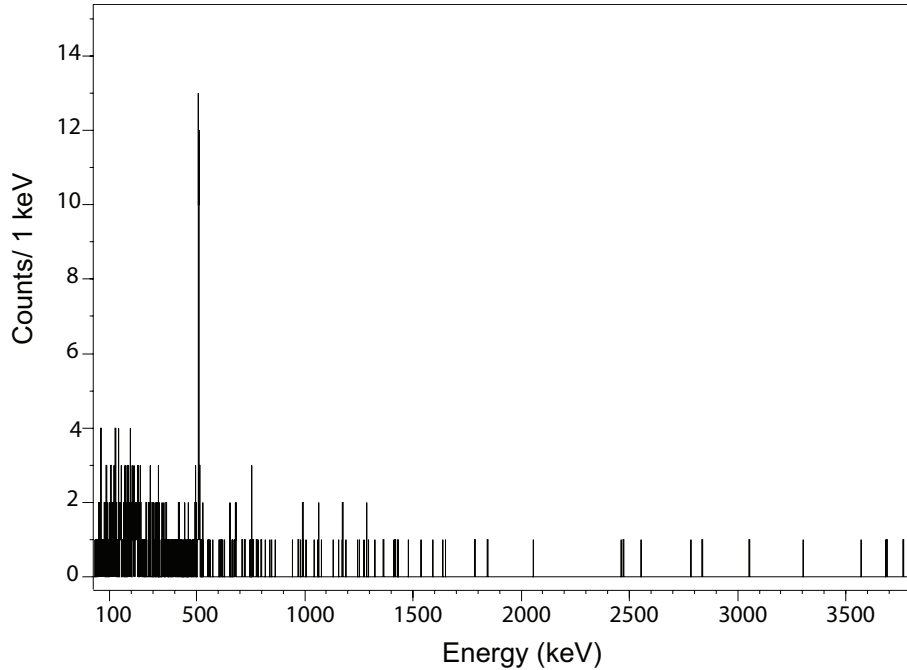Figure 5.4: γ-ray spectrum in coincidence with β-decay events of ^{96}Cd, ocurring in the same and the four nearest neighbor pixels within 10 seconds of a fragment implantation. The 511 keV peak from positrion annihilation is clearly distinguished. No γ transitions could be identified and assigned to the β-decay of ^{96}Cd.

obtained with the MLH analysis. It was found that the best fit corresponded to the assumption of a single component in the decay.

As noted in the previous chapter, β-delayed γ transitions can provide a way to isolate different parent β-decay components. The β-delayed γ spectrum of ^{96}Cd is shown in Fig. 5.4. As can be seen, the statistics of $\beta-\gamma$ coincidences was not sufficient; no clear γ-ray peaks are visible appart from the positron annihilation peak at 511 keV. Therefore, it is not possible to draw a conclusion about the existence of a β-decaying 16^+ spin-gap isomer as predicted by Ogawa in [1] (see Section 2.1), with a half-life of 0.5 s. Our statistics were not sufficient to exclude the possibility that the β-decay half-life determined in this work is a mixed half-life from ground and isomeric states.

To investigate the possibility of a γ-decaying isomer, the prompt γ spectrum of ^{96}Cd is presented in Fig. 5.5. This spectrum was obtained within 12 μs of a ^{96}Cd implantation. There is no indication of a γ-decaying isomer. However, we cannot exclude the possibility of a γ-decaying μs isomer with a production fraction smaller
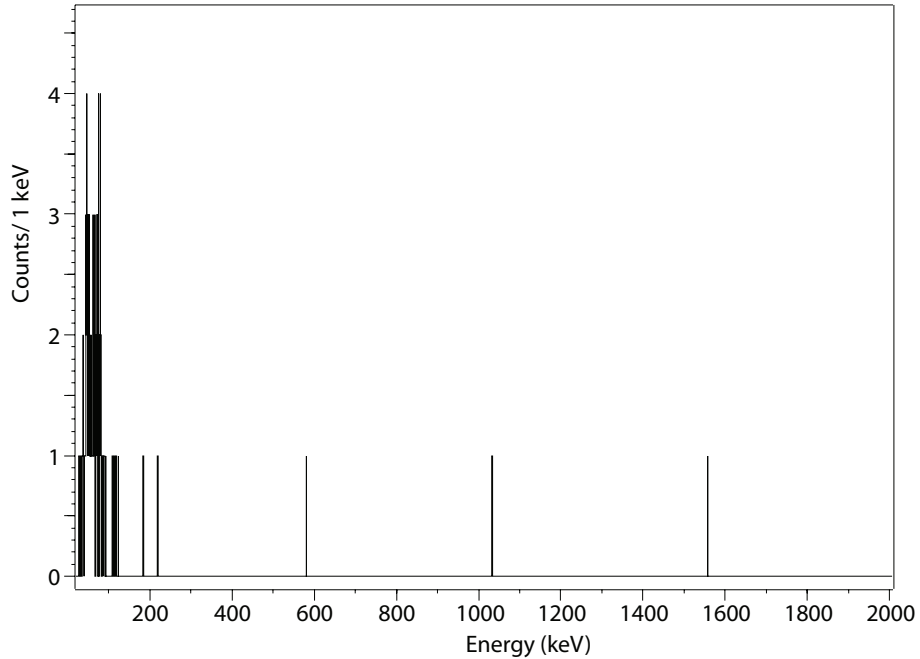
Figure 5.5: Prompt γ-ray spectrum in coincidence with ^{96}Cd implantation events. No γ transitions could be identified and assigned to the decay of excited states in ^{96}Cd.

than about 7%, assuming a typical isomeric γ transition energy of 100 keV. Such a decay would have been below the sensitivity of our experiment.

Figure 5.6 shows the comparison of the half-life of ^{96}Cd determined in this work to the predicted half-lives in references [74–77]. Our measurement agrees, within error bars, with the prediction by Möller, wich used a QRPA global model [76].

5.1.2 ^{98}In

The odd-odd ^{98}In nucleus was previously investigated by Faestermann *et al.* [78]. The nuclei in that experiment were produced by fragmentation of a ^{112}Sn primary beam, accelerated to 1 GeV/u, impinging on a Be target. Two β-decaying states were observed: a short-lived component, with a half-life of 32^{+32}_{-11} ms, assigned to the $0^+ \rightarrow 0^+$ superallowed Fermi decay of the ground state, and a longer component with a half-life of $1.2^{+1.2}_{-0.4}$ s, attributed to an isomeric state, possibly with a high spin.

In this work, 216 (21) fragments of ^{98}In were implanted in the DSSD. The distribution of observed β-decay events that followed ^{98}In implantations is presented

71
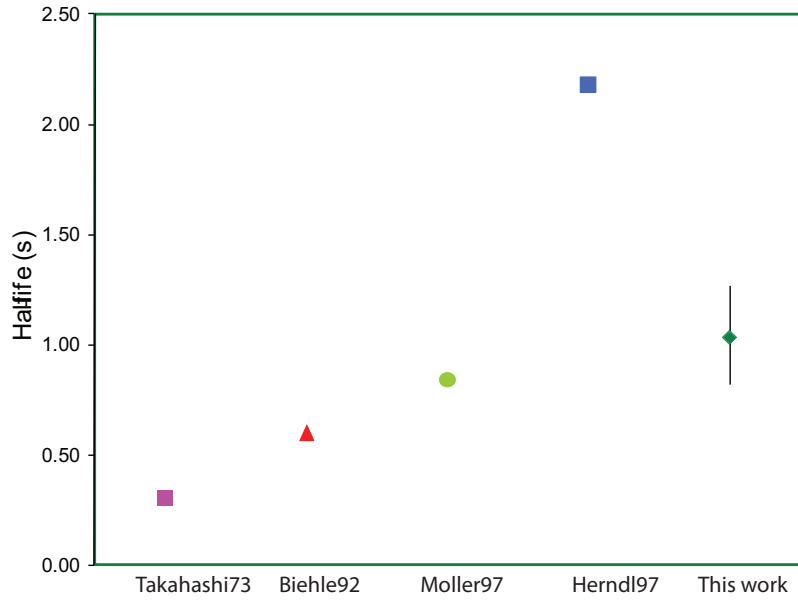
Figure 5.6: Comparison of the half-life of ^{96}Cd measured in this work to the theoretical predictions by [74–77].
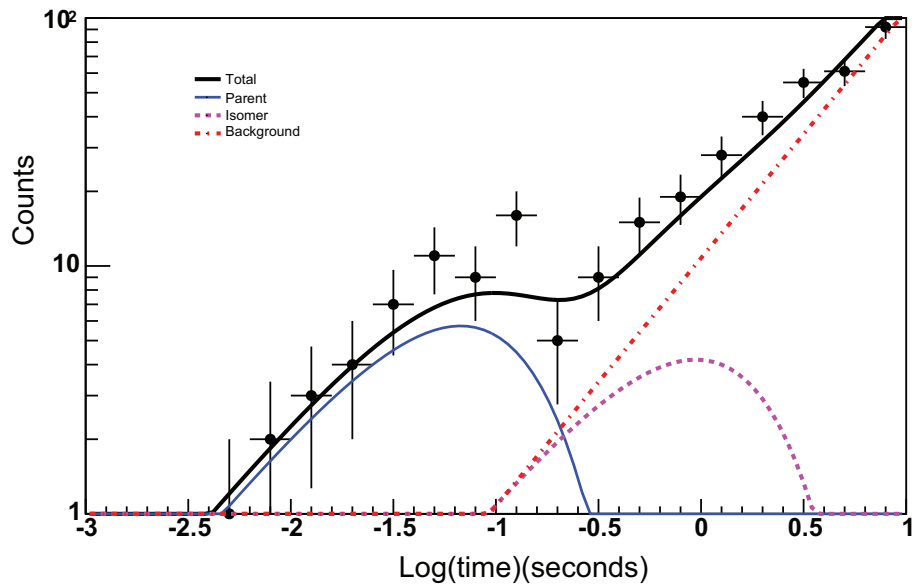
Figure 5.7: Number of decays observed for ^{98}In as a function of logarithmic time. The blue curve peaks around -1.3, which corresponds to a half-life of 47 ms. The dashed curve yields a half-life value of 0.66 s. The fit considers the decay of two components, and includes the daughter decay and a predicted constant background, which is observed as a straight line in the plot (dot-dashed). The total is indicated by a thick black solid line.

as a function of the logarithmic time in Fig. 5.7. We confirm the existence of two

β-decay components, with half-lives of 47 (13) ms, and 0.66 (40) s, which presum-

ably correspond to the ground and isomeric states, respectively. The contribution to the observed decay from the isomeric state was deduced as 42 (20)% from the two-component fit. The β-delayed γ spectrum of ^{98}In is shown in Fig. 5.8. No transitions associated with the ^{98}In β-decay were found. The prompt γ spectrum of ^{98}In does not show any lines either.
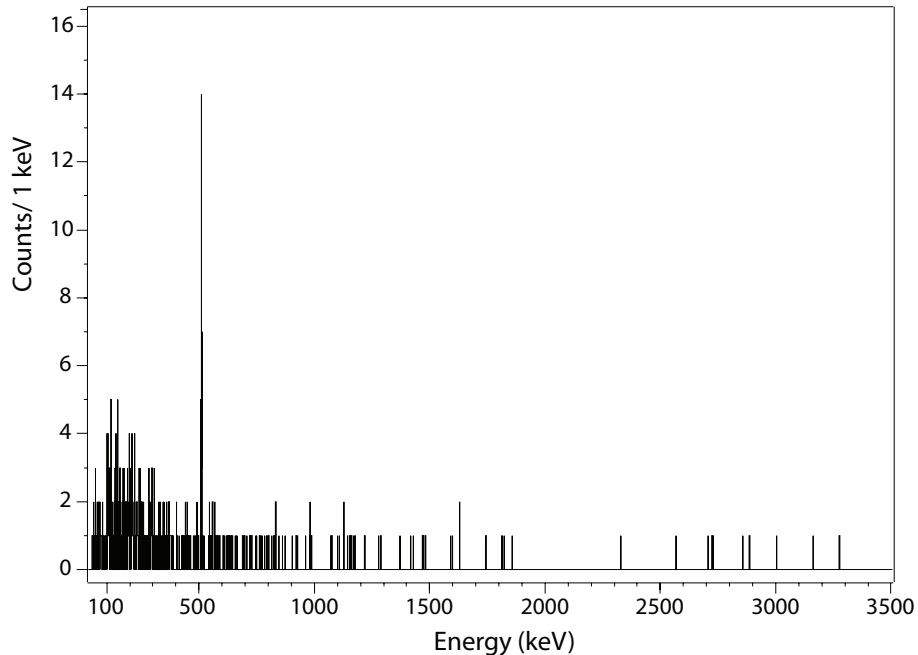
Figure 5.8: γ-ray spectrum in coincidence with β-decay events of ^{98}In, ocurring within a 5-pixel correlation area, and within 10 s of a fragment implantation. Apart from the 511 keV, no γ transitions were identified.

5.1.3 ^{100}Sn

As was described in previous chapters, production and separation of ^{100}Sn has been a major experimental challenge for the field. At the NSCL, a production study was done in order to determine the production settings that would maximize production of ^{100}Sn. Based on production cross sections reported by previous experiments, primary beams of ^{124}Xe and ^{112}Sn were tested on ^{9}Be and ^{9}Be+^{nat}Ni targets of various thickeness and an estimate of the yield (in particles per second) was made in each case. An overwiew of previous experiments that successfully produced ^{100}Sn, together

Reference	Production	Primary beam energy	σ (pb)
NSCL [69]	^{112}Sn + Be	120 MeV/u	0.25(12)
GSI [80]	^{124}Xe + Be	1 GeV/u	$11^{+5.5}_{-3.7}$
GSI [68]	^{112}Sn + Be	1 GeV/u	$1.8^{+2.9}_{-1.1}$
GANIL [79]	^{112}Sn + Ni	63 MeV/u	≥ 120

Table 5.1: ^{100}Sn cross section values determined in the various fragmentation experiments dedicated to its production and identification. The acronyms GSI and GANIL stand for "Gesellschaft fur Schwerionenforschung" and "Grand Accelerateur National d'Ions Lourds", respectively.

with a brief summary of the tests performed at NSCL was presented in Section 3.4.

In Experiment 07034, fourteen events were identified as ^{100}Sn during 11.5 days of measurement. This yielded a production cross section of 0.25 (15) pb. Our result, together with those from other measurements utilizing fragmentation as production mechanism, is reported in Table 5.1. Our value is in sharp constrast with the 120 pb lower limit established at an incident energy of 63 MeV/nucleon of the same primary beam [79].

The LISE++ predictions of the fragment yields of $N = Z$ nuclei for Experiment 07034 were between a factor of 10 and 30 higher than the actual measured rates. The reported cross sections measured at relativistic energies do not show such discrepancy [71, 80].

The time distribution of the ^{100}Sn β decay events observed in Experiment 07034 is shown in Fig. 5.9. Using an MLH analysis, a β-decay half-life was determined as $0.55^{+0.70}_{-0.31}$ s. With such low statistics it was impossible to detect either prompt or β-delayed γ radiation.

5.2 Other neutron-deficient nuclei produced in Experiment 07034

Besides the $N = Z$ nuclei presented in the previous section, we studied several $N = Z + 1$ and $N = Z + 2$ nuclei. Results on β-decay half-lives and prompt and β-delayed
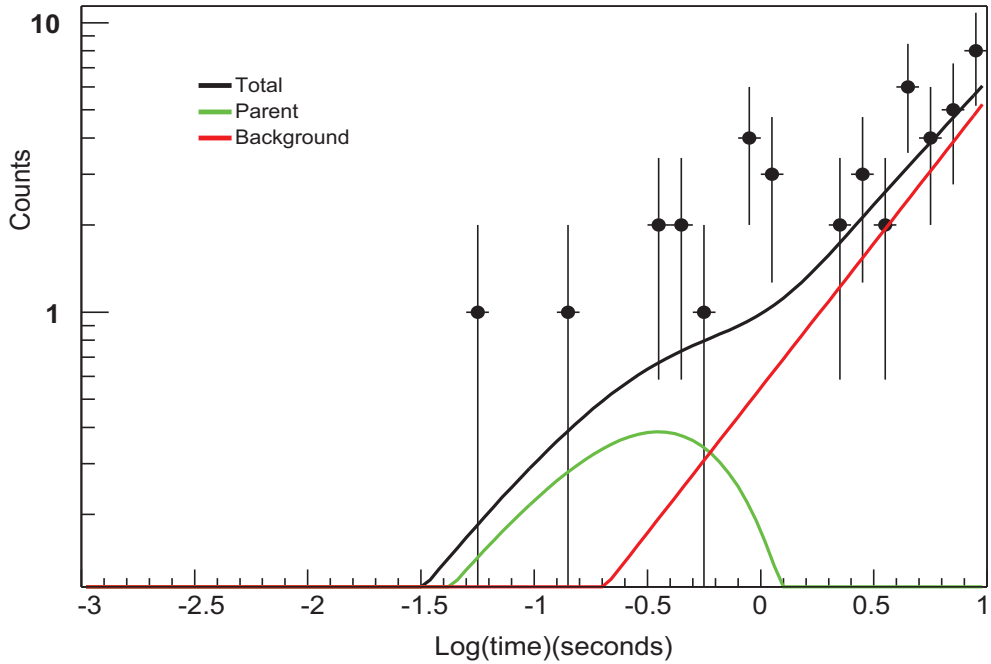
Figure 5.9: Number of decays observed for ^{100}Sn as a function of logarithmic time. The fit is the result of an MLH analysis that, as in the case of ^{96}Cd, considered a calculated background, and the information of the known half-lives of the implanted nuclei and their decay daughters.

γ spectroscopy will be presented in the following sections for some of these nuclei.

5.2.1 Isomeric decay of ^{96}Ag

^{96}Ag is a $T_z = 1$ nucleus (i.e. $(A - 2Z)/2 = 1$), with three proton holes and one neutron hole relative to ^{100}Sn. It was first identified by Kurcewicz *et al.* [81] using the ^{60}Ni(^{40}Ca,p3n)^{96}Ag reaction. A half-life of 5.1(4) s was deduced for this nucleus from the analysis of β-delayed protons, and spin and parity of 8^+ or 9^+ was suggested for its ground state. Later, Batist *et al.* [39] identified two β-decaying states in ^{96}Ag with half-lives of 4.40(6) and 6.9(6) s and tentative spins and parities of 8^+ and 2^+, respectively; however, none of them was assigned as the ground-state. Evidence for additional excited states in ^{96}Ag was reported by Grzywacz *et al.* [38], who discovered the existence of an isomeric state with a half-life of 0.7 (2) μs and observed two γ transitions with energies of 470 keV and 667 keV originating from the γ decay of the

Figure 5.10: Prompt γ-ray spectrum and isomeric decay curve (inset) of ^{96}Ag observed by Grzywacz *et al.* [38]. Figure reproduced from Ref. [38].
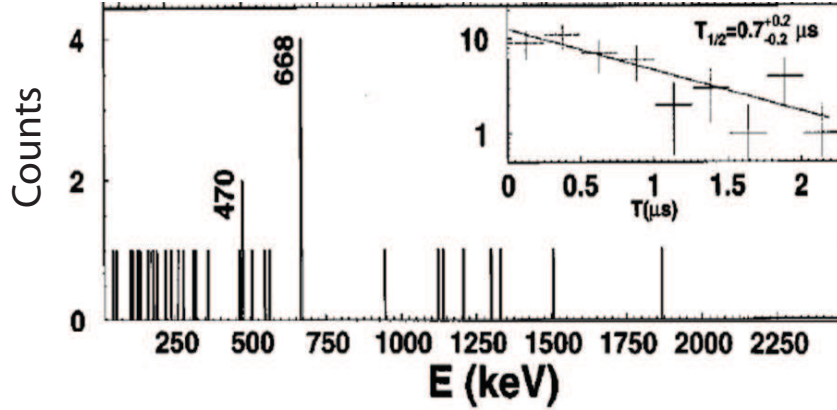
isomer (see Fig. **??**); however, statistics were not sufficient to construct a level scheme. Based on a shell model prediction in the proton-neutron ($p_{1/2}$, $g_{9/2}$) model space using an empirical interaction [82], Grzywacz *et al.* suggested the decay of a 15^+ or 13^- isomer followed by a few γ transitions. In this work, we report a new measurement of the lifetime of this isomer, and the observation of several new γ transitions, one of which indicates the existence of a second, longer-lived μs isomeric state in ^{96}Ag.

The spectrum of γ rays observed between 1.2 and 12 μs after implantation of a ^{96}Ag ion is shown in Fig. 5.11. The lower time limit of 1.2 μs was chosen to eliminate prompt X-rays and low-energy γ-rays produced by beam fragments interacting with the silicon detectors. Apart from the 470-keV and 667-keV transitions, which were previously reported by Grzywacz *et al.* [38], all of the γ transitions in Fig. 5.11 were observed in the present experiment for the first time.

The time distribution of each of the γ lines of interest was analyzed to assign them to the decay of a specific isomer and to determine isomeric half-lives. The 257-, 630-, 667-, and 1506-keV transitions decay with the same half-life. An OR of these energies was used to obtain the isomeric decay curve shown in Fig. 5.12(a). A fit to the decay curve taking into account a single exponential decay plus a constant background resulted in a half-life of 1.45(7) μs, more than two times longer than the
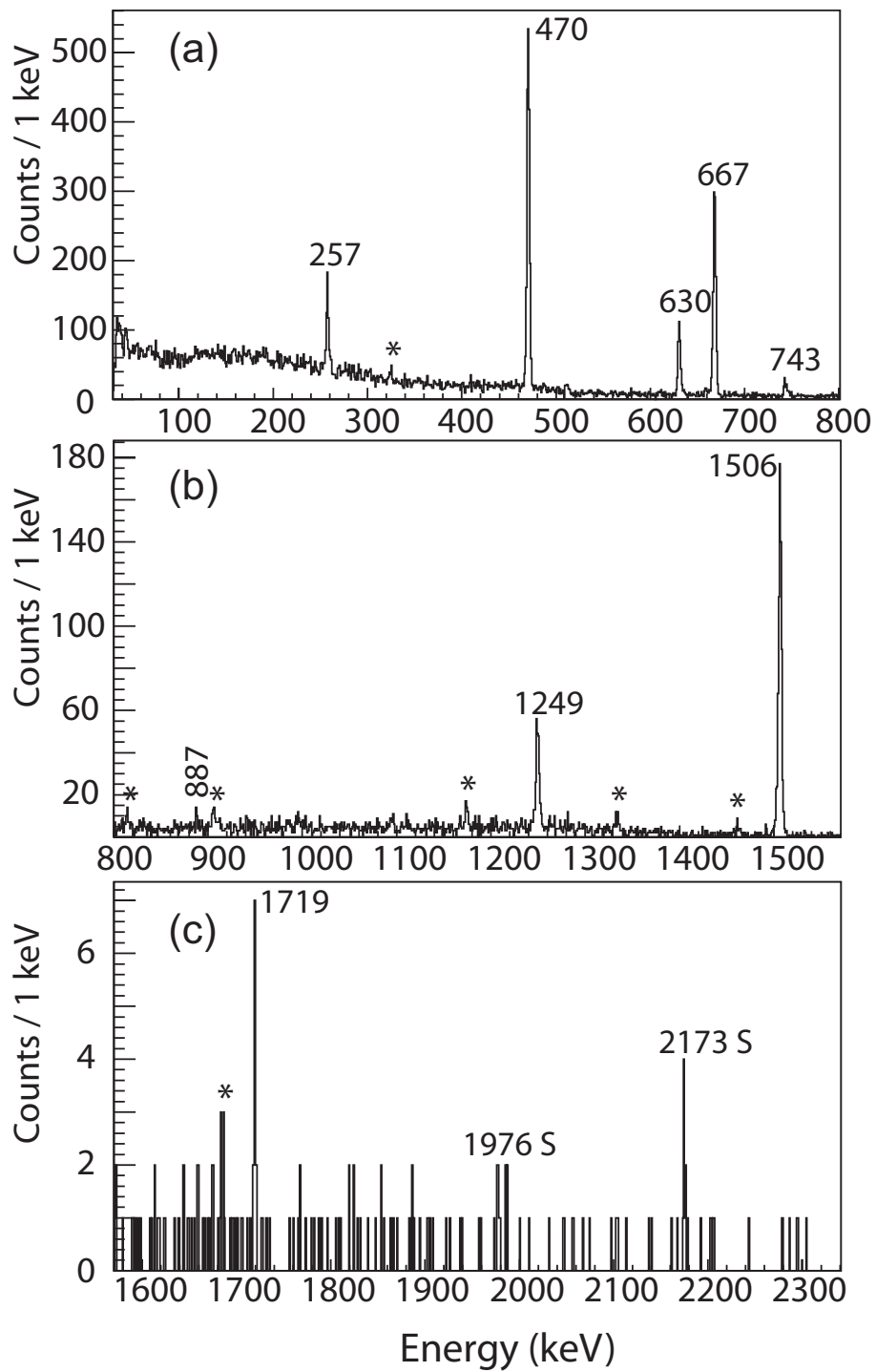
76

Figure 5.11: γ-ray spectrum collected between 1.2 and 12 μs after an ^{96}Ag implantation. Transitions belonging to the isomeric decay of ^{96}Ag are labeled by their energies in keV. Lines marked with an asterisk are known background from neighboring ^{94}Pd. Summing peaks are marked by the letter S.

previously-reported value of 0.7(2) μs [38]. The 743-keV transition, however, appears to decay with a longer half-life (see Fig. 5.12(b)). The fit to this decay curve needed to consider the time dependence of the background attributed to the contribution from the decay of the shorter-lived isomer. The low intensity of the 743-keV transition and the short 12 μs collection time results in large error bars in the half-life determination: $8.6 \pm 6.3 \mu$s. Nonetheless, we interpret this as an indication that the 743-keV transition corresponds to the decay of an additional, longer-lived microsecond isomer in ^{96}Ag.

The isomeric fractions were calculated following the procedure outlined by Daugas *et al.* [70], considering the number of counts in the 630-keV and 667-keV peaks, the total number of implanted ^{96}Ag ions, and the 475 ns flight time of the fragments from the target to the DSSD. An isomeric production fraction of 10.8 (12) % was estimated for the short-lived isomer in the fragmentation process. Similarly, by comparing the number of counts in the 743-keV peak to the total number of ^{96}Ag implants, a 0.59 (9) % production of the long-lived isomer was estimated.

A 2-dimensional $\gamma\gamma$ coincidence matrix was constructed for γ rays which occurred within the first 12 μs after a ^{96}Ag implantation. 1-dimensional coincidence spectra were then obtained by setting energy gates on the lines of interest in the $\gamma\gamma$ matrix (Figs. 5.13 and 5.14). Table 5.2 summarizes the observed $\gamma\gamma$ coincidence relationships, as well as the intensities of all transitions, normalized to the transition with an energy of 470 keV. A total of 1.1×10^4 counts were detected in the 470-keV peak, several orders of magnitude higher than in the previous measurement. Based on these coincidences, their relative intensities, and energy-sum relationships, the decay scheme for ^{96}Ag presented in Fig. 5.15 (a) is proposed. The 470-keV line was placed at the bottom of the level scheme based on two observations: it was the most intense transition and it was in coincidence with nearly all other transitions (with exception of the transition with energy 1718 keV). Energy-sum relationships were used to place the 1506-keV transition that is proposed to connect the levels with energies 1976 and 470 keV; and the 1718-keV ground-state transition. The 630-keV and 667-keV γ-rays are not in
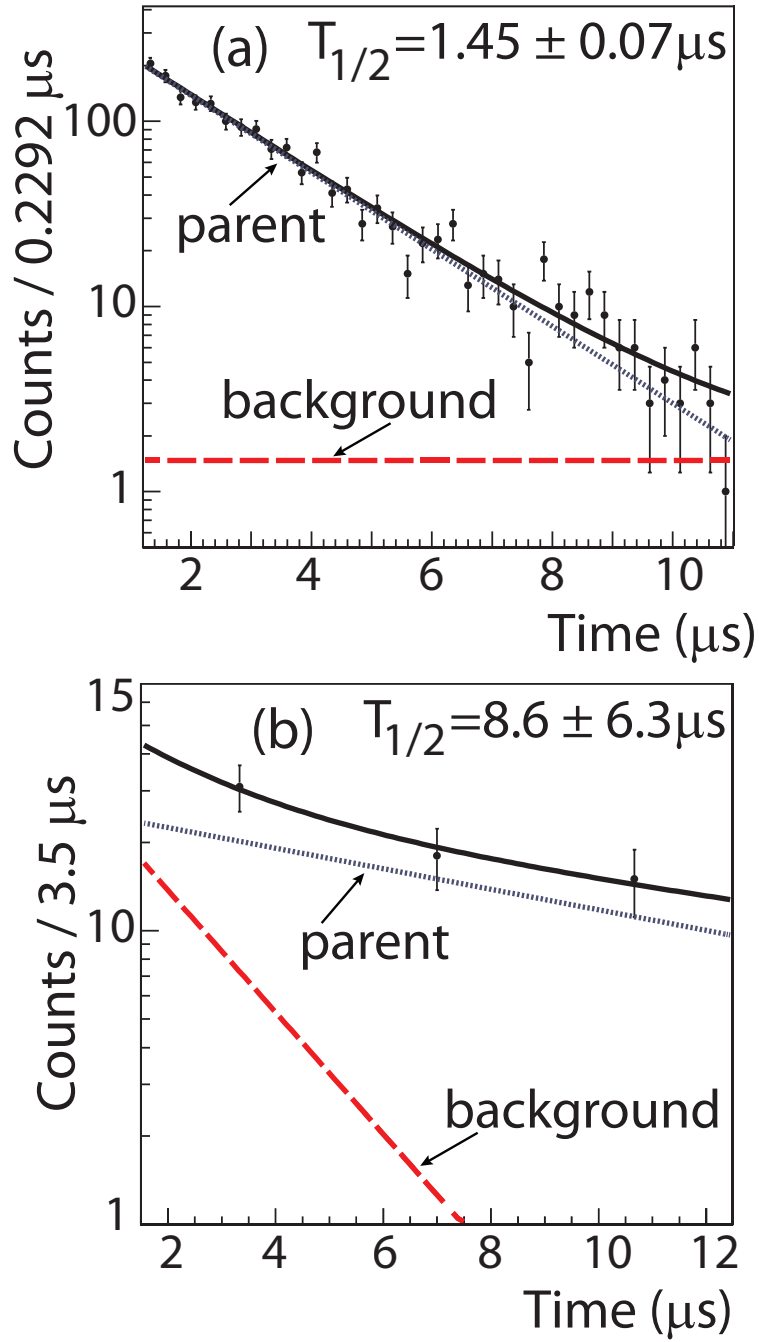
Figure 5.12: Decay curves and fits of the microsecond isomers in ^{96}Ag. (a) Decay curve obtained by gating on the 257, 630, 667, and 1506-keV γ-ray transitions. The curve was fitted with a single exponential and constant background. (b) Decay curve obtained by gating on the 743-keV γ-ray transition, fitted with a single exponential decay and a time-dependent background.

Table 5.2: Energies, intensities, and coincidence relationships of γ rays assigned to the isomeric decay of ^{96}Ag.

E_γ (keV)	$I\gamma$(%)	Coincident transitions (keV)
257.2 (2)	17.3 (16)	470, 630, 667, 1249, 1719
470.0 (2)	100.0 (67)	257, 630, 667, 743, 1249, 1506
630.1 (2)	21.8 (20)	257, 470, 1249, 1506
667.4 (2)	71.1 (51)	257, 470, 1249, 1506
742.7 (3)	4.5 (9)	470, 1249, 1719
887.4 (6)	1.0 (4)	
1248.8 (2)	21.9 (23)	257, 470, 630, 667, 743
1505.9 (2)	81.4 (63)	470, 630, 667
1718.9 (3)	1.8 (4)	257, 743

coincidence with each other, or with the 743-keV line, so they were placed on top of the cascade, both feeding the 1976 keV level.

The β decay of two low-lying states in ^{96}Ag with proposed spins and parities 2^+ and 8^+, and half-lives of 6.9(6) and 4.40(6) s, respectively, was reported by Batist *et al.* [39]. Implanted nuclei correlated with the 470-keV line were tagged to determine which of these two β-decaying states was populated following the decay of the microsecond isomers. The β-decay curve of the tagged nuclei is shown in Fig. 5.16. The deduced half-life of 4.74(95) s is consistent with that reported by Batist *et al.* for the 8^+ β-decaying level [4.40(6) s]. Furthermore, the β-delayed γ spectrum of the tagged nuclei was compared to that of all the ^{96}Ag implanted nuclei. A considerable decrease of more than 30% was observed in the relative intensity of the 1415-keV γ-ray transition in the daughter ^{96}Pd. The 1415-keV transition, according to Batist *et al.*, is mostly fed by the β decay of the 2^+ level (see Fig. 3 in Ref. [39]). Therefore, the 1.45 μs isomer most likely populates the 8^+ β-decaying state.

To gain a better understanding of the nature of the isomeric states observed, and to tentatively assign spins and parities to the inferred energy levels of ^{96}Ag, two different shell-model calculations were performed, hereafter referred to as the SLGT, and the jj44b calculations, respectively. In Fig. 5.15 the level scheme of ^{96}Ag as inferred from our experiment is compared with the predictions of both shell-model calculations.
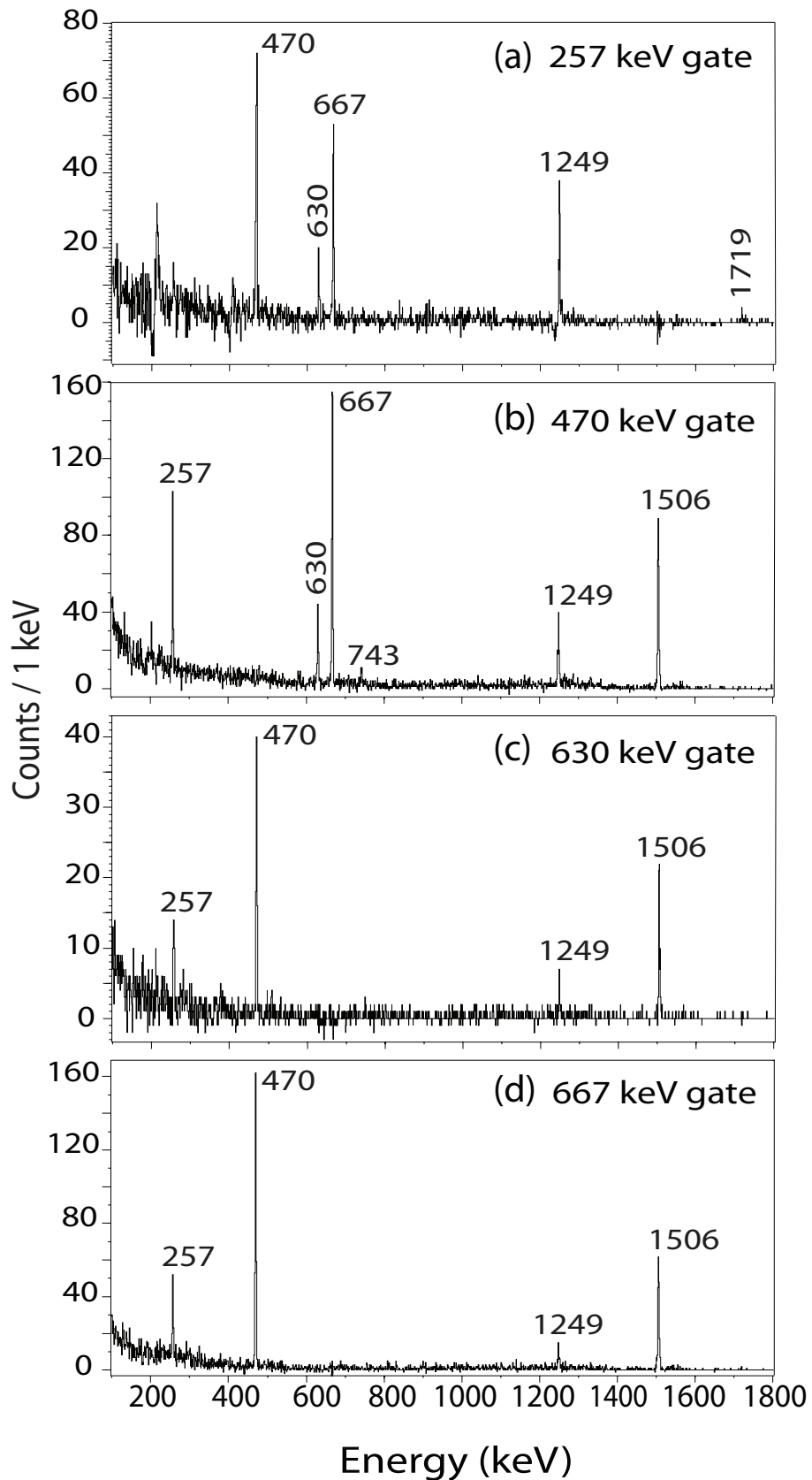
Figure 5.13: Background-corrected fragment-$\gamma\gamma$ coincidence spectra obtained by applying gates on the (a) 257-keV, (b) 470-keV, (c) 630-keV, (d) 667-keV γ rays. These coincidences together with those shown in Fig. 5.14 were used to deduce the ^{96}Ag level scheme.
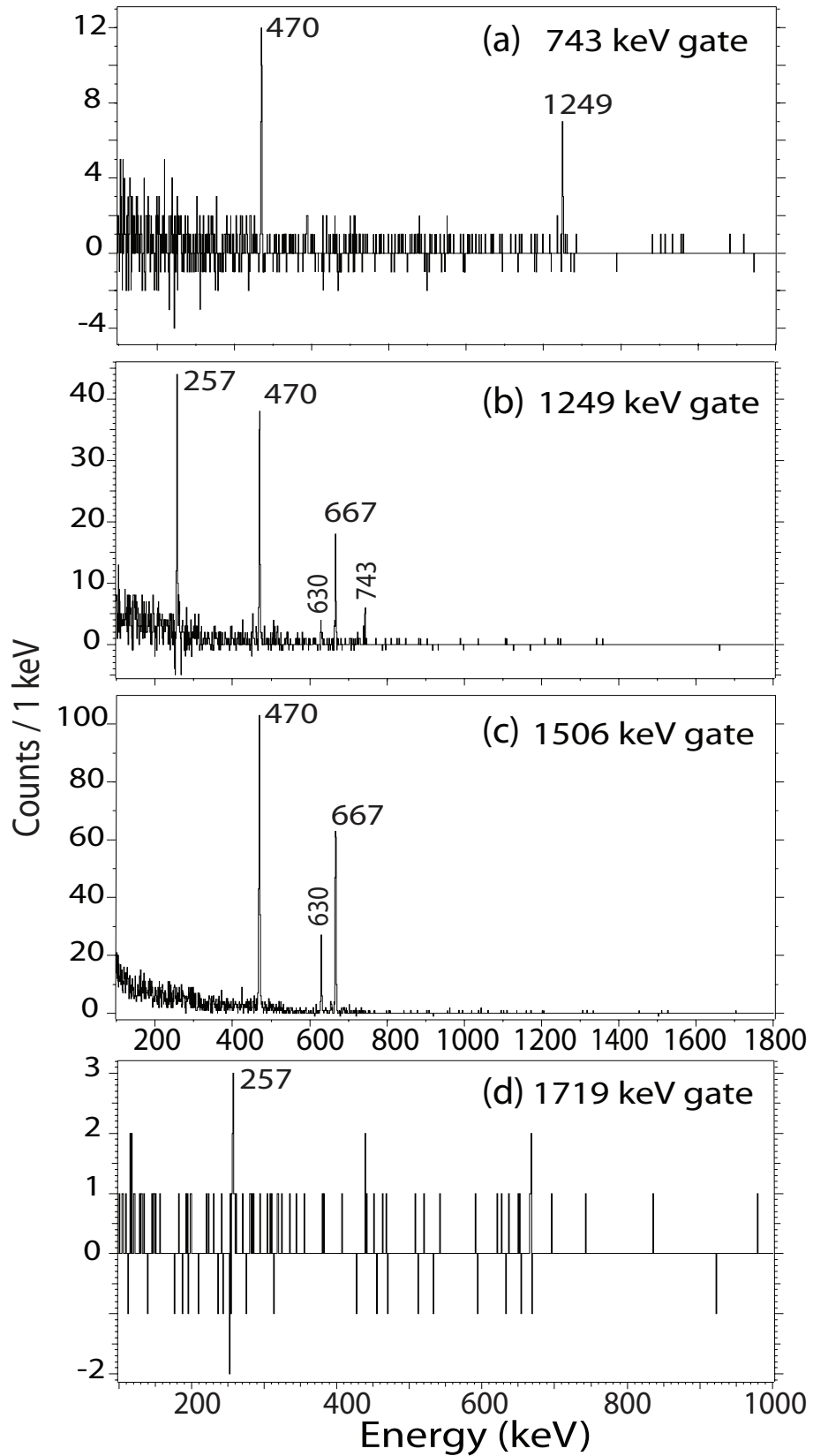
Figure 5.14: Background-corrected fragment-$\gamma\gamma$ coincidence spectra obtained by applying gates on the (a) 743-keV, (b) 1249-keV, (c) 1506-keV and (d) 1719-keV γ rays. These coincidences were used to deduce the ^{96}Ag level scheme.
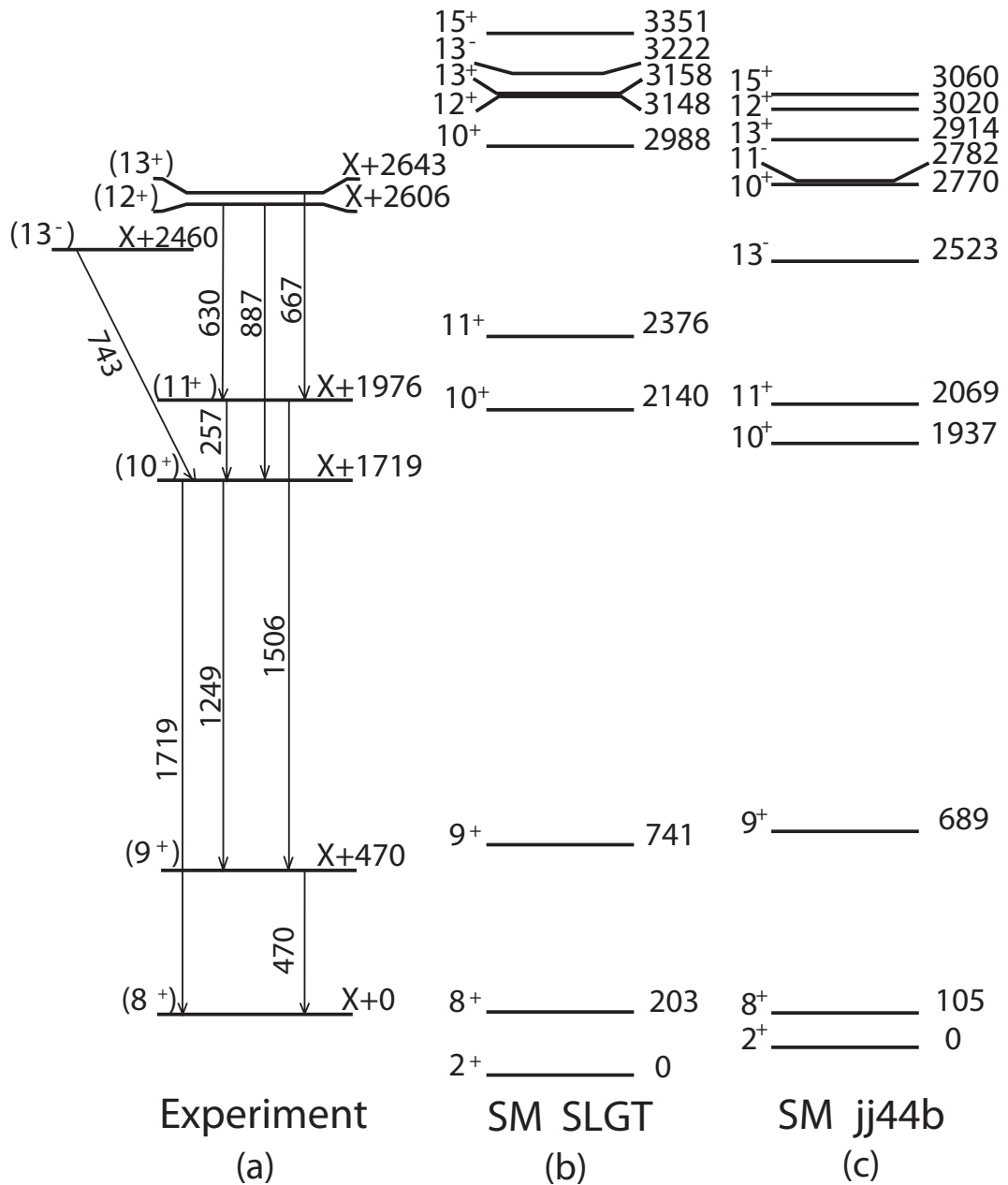
Figure 5.15: (a) Proposed level scheme of ^{96}Ag, compared to the results of shell-model calculations made with the SLGT interaction (b) and the jj44b interaction (c). Tentative spins and parities were adopted from the results of the jj44b calculation. Deduced level energies are relative since the energy of the 8^+ state is unknown. The newly-identified 15^+ isomeric level is not drawn in the experimental level scheme. See text for details.

Both shell-model calculations were performed by B. Alex Brown and reported in [83].

The SLGT calculation was performed with the code OXBASH, within the $g_{9/2}, p_{1/2}$ model space using the SLGT effective interaction [77], and assuming a ^{100}Sn core. This calculation predicts one potentially isomeric state located at 3148 keV above the 8^+ state (3351 keV above the 2^+ state), with spin and parity 15^+ [see Fig. 5.15 (b)]. The predicted half-life of the E2 $15^+ \rightarrow 13^+$ transition is around 15 ns, much shorter than the half-life of 1.5 μs reported here. Using the B(E2) strength from the SLGT calculation and our measured half-life of 1.5 μs, the energy of the isomeric transition can be estimated as 77 keV; this energy is 116 keV smaller than predicted by the shell model, but well within typical shell model uncertainties. Such a 77-keV transition is predicted to be highly converted [α=3.67(6)]. No evidence of a 77 keV γ-ray was found in our data, which is consistent with the expected small statistics and signal to background ratio in that energy range. Our experimental setup was also not sensitive to the low-energy electrons expected from this transition.
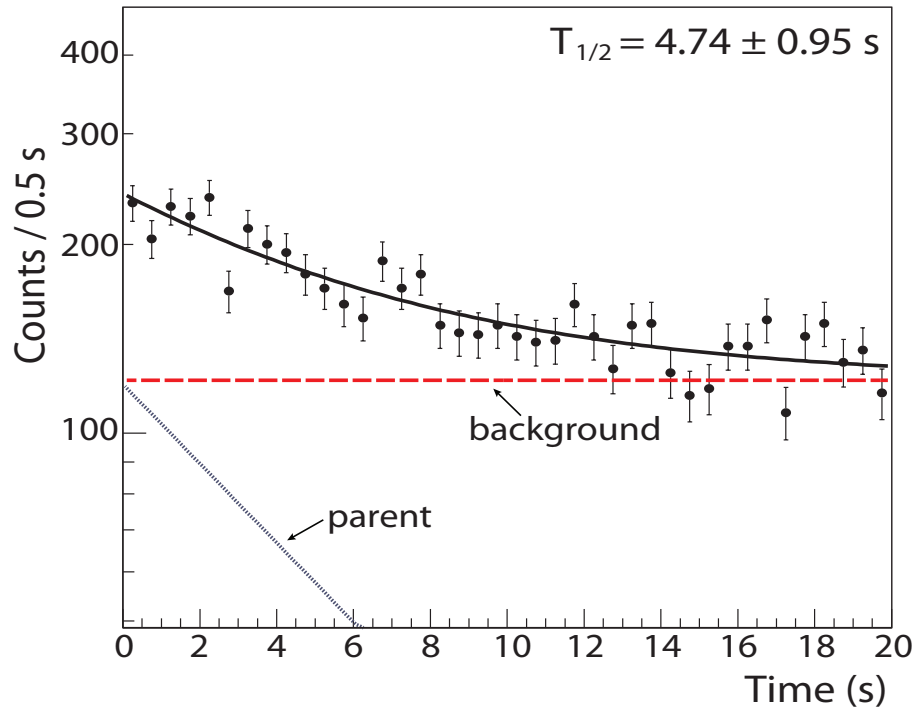

Figure 5.16: β-decay curve of the ^{96}Ag implants which were correlated with the 470-keV transition. The resulting half-life of 4.74 (95) s agrees with the known half-life of the β-decaying state in ^{96}Ag with tentative spin and parity 8^+.

The second shell-model calculation was carried out in the $(p_{3/2}p_{1/2}f_{5/2}g_{9/2})$ model space considering a ^{56}Ni core and using the jj44b Hamiltonian. The jj44b Hamiltonian was obtained from a fit to about 600 binding energies and excitation energies with a method similar to that used for the JUN45 Hamiltonian [84]. Most of the energy data for the fit came from nuclei with $28 \leq Z \leq 30$ and $48 \leq N \leq 50$. Using a fit with 30 linear combinations of the $J - T$ two-body matrix elements, which conserve isospin, varied, the rms deviation between experiment and theory for the energies in the fit was about 250 keV. Proton and neutron effective charges of e_p=1.5 and e_n=0.5 were used. Predictions obtained with the jj44b Hamiltonian have been compared to experimental data for Ga [84,85] and Cu [86,87] isotopes, showing remarkable agreement. The jj44b calculation predicts a 0.99 μs (partial) half-life for a 146 keV $15^+ \rightarrow 13^+$ E2 transition [see Fig. 5.15 (c)] that feeds a cascade to the 8^+ level. Again, given the experimental conditions, a 146-keV transition of the expected intensity would not be observed. Additionally, the jj44b calculation predicts a low-lying 13^- state, which could explain the longer-lived isomer as a slow E3 transition. Since most of the E3 strength comes from orbitals outside the model space, the reduced E3 transition strength measured in a nearby nucleus was used as reference to estimate the expected lifetime. The closest nucleus to ^{96}Ag for which a measured E3 value is available is ^{93}Tc [88], with B(E3) = 540 e^2fm^6, resulting in a $13^- \rightarrow 10^+$ half-life of 18 μs. The $13^- \rightarrow 11^+$ transition is expected to have mixed M2/E3 character, with a partial half-life of a few hundred microseconds, as calculated using the values of the B(M2) and B(E3) obtained in ^{93}Tc. The small branching ratio for this transition would not have been detected in the present experiment. The resulting half-life of the 13^- state of 18 μs is within a factor of two of the deduced value of $8.6 \pm 6.3 \mu$s reported here.

Overall, both shell model calculations reproduce the observed level sequence and γ-ray cascades for the short-lived isomer. The jj44b calculation, with its larger model space, predicts excitation energies better than the SLGT one, and reduces the excitation energy of the 13^- state sufficiently to provide an explanation for the longer-lived

isomer identified in the present work. The jj44b results were used to tentatively assign spins and parities to the experimental levels presented in Fig. 5.15 (a).

5.2.2   Isomeric decay of ^{94}Pd

^{94}Pd is also a $T_z = 1$ nucleus, and, similarly to ^{96}Ag, it also exhibits high-spin isomeric states. Excited states in ^{94}Pd were investigated by La Commara *et al.* [52], Marginean *et al.* [51], and by Plettner *et al.* [43] through analysis of the β-decay of ^{94}Ag. A microsecond isomer with spin and parity of 14^+ was established, de-exciting through a cascade of γ-transitions with energies of 95, 324, 660, 814, 905, 994 and 1092 keV. The isomeric half-life had been measured in previous experiments as 0.8 ± 0.2 μs by Gorska *et al.* [89] and 0.530(10) μs by Grzywacz *et al.* [38]. Five new γ transitions with energies of 267, 408, 597, 979 and 1545 keV were reported in [52] as prompt lines, not in delayed coincidence with the cascade de-exciting the 14^+ isomer, and placed tentatively in the level scheme. This placement was later confirmed by Plettner *et al.*

In Experiment 07034, ^{94}Pd nuclei were produced in the fragmentation process in their excited states in sufficient quantities to perform γ spectroscopy. Fig. 5.17 shows the γ-ray spectrum collected within 12 μs of a ^{94}Pd implantation event. Table 5.3 summarizes the observed $\gamma\gamma$ coincidence relationships, as well as the intensities of the γ transitions observed in ^{94}Pd. Additionally, the inset of Fig. 5.17 shows a 1651-keV transition, which had not been seen before, and that suggests the existence of a second high-spin isomeric state (see below).

The time distribution of each of these γ lines of interest was analyzed to assign them to the decay of a specific isomer and to determine isomeric half-lives. The 96, 324, 347, 660, 745, 814, 906, 994 and 1092-keV transitions decay with the same half-life. An OR of the 324, 660, 814, 905, 994 and 1092 keV-transitions was used to obtain the isomeric decay curve shown in Fig. 5.18. A fit to the decay curve taking into account a single exponential decay plus a constant background resulted in a half-life of 482 (14) ns, which is within the range of values reported before [38, 90].
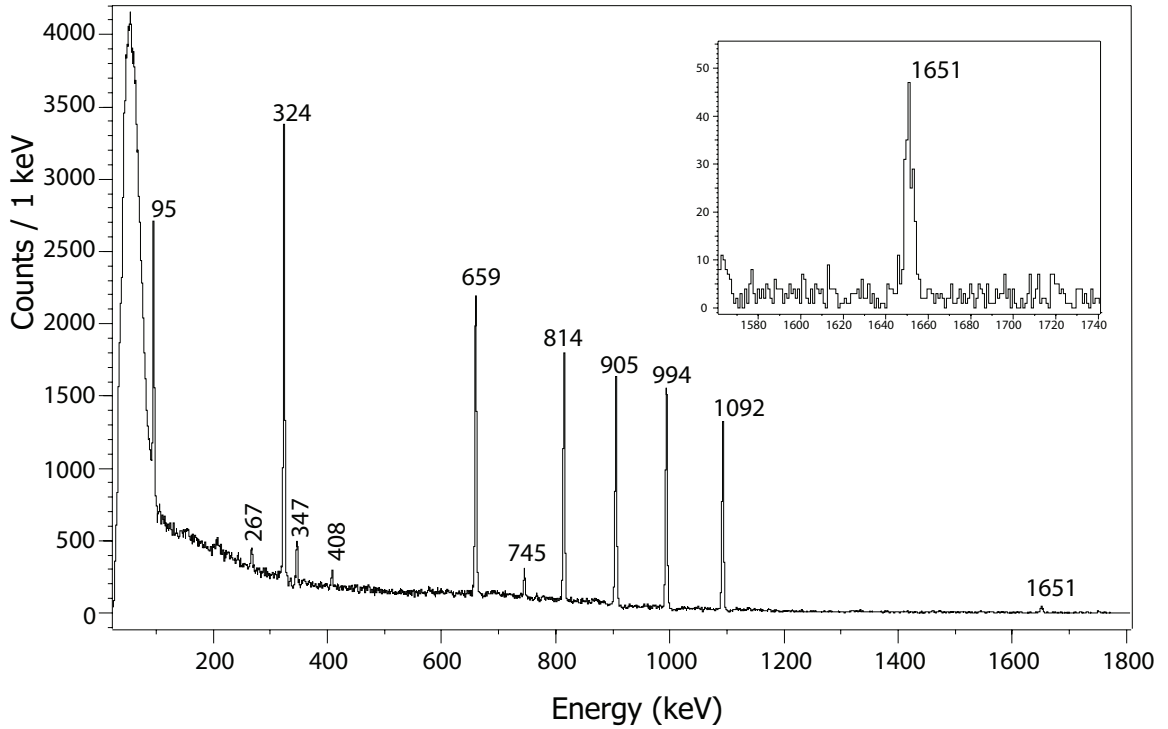
Figure 5.17: γ-ray spectrum collected within 12 μs of a ^{94}Pd implantation. Transitions belonging to the isomeric decay of ^{94}Pd are labeled by their energies in keV.

Table 5.3: Energies, intensities, and coincidence relationships of gamma rays assigned to the isomeric decay of ^{94}Pd.

E_γ (keV)	$I_\gamma(\%)$	Coincident transitions (keV)
95.4 (2)	21.0 (16)	324, 659, 814, 905, 994, 1092, 1651
267.7 (3)	3.3 (4)	95, 324, 347, 408, 659, 814, 905, 994, 1092, 1651
324.1 (2)	97.5 (70)	95, 268, 347, 659, 745, 814, 905, 994, 1092, 1651
347.2 (2)	7.8 (7)	95, 324, 659, 745, 814, 905, 994, 1092
408.3 (3)	3.0 (4)	95, 267, 324, 659, 814, 905, 994, 1092, 1651
659.5 (2)	95.7 (69)	95, 325, 659, 745, 814, 905, 994 1092, 1651
745.2 (2)	7.7 (7)	324, 347, 659, 814, 905
814.3 (2)	96.3 (7)	95, 324, 347, 659, 745, 905, 994, 1092, 1651
905.5 (2)	96.6 (7)	95, 324, 347, 659, 745, 814, 994, 1092, 1651
994.2 (2)	100.0 (73)	95, 324, 347, 659, 814, 905, 1092, 1651
1092.4 (2)	93.6 (68)	95, 324, 659, 814, 905, 994, 1092, 1651
1544.7 (5)	0.7 (2)	95, 268, 324, 408, 659, 814, 905, 994, 1092
1651.1 (16)	4.0 (4)	95, 268, 324, 408, 659, 814, 905, 994, 1092

Figure 5.18: Decay time spectrum obtained by gating on the 324, 660, 814, 905, 994, and 1092 keV transitions of ^{94}Pd. The resulting decay curve was fitted with a single exponential and a constant background.
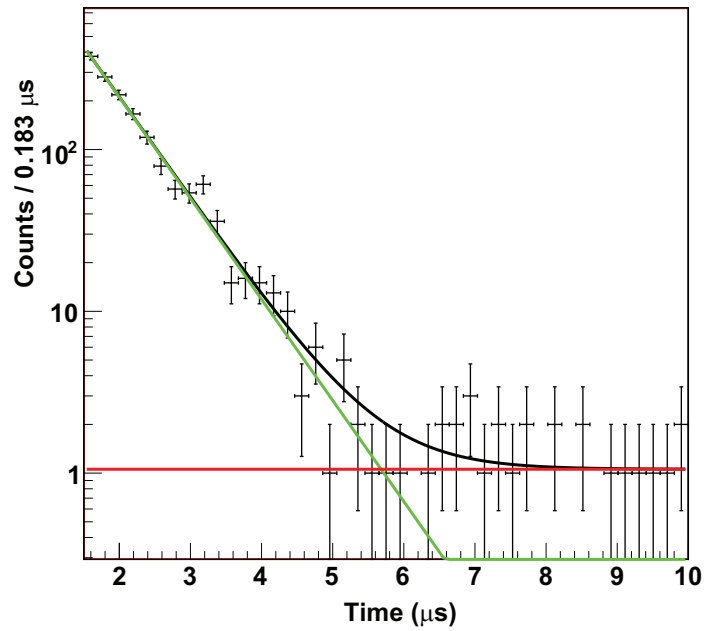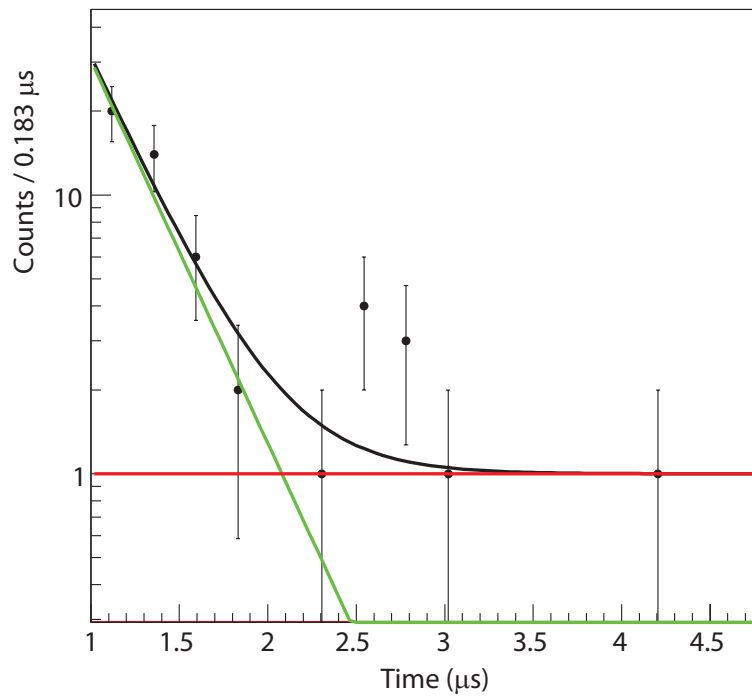

Figure 5.19: Decay time spectrum obtained by gating on the 1651 keV transition of ^{94}Pd. The resulting decay curve was fitted with a single exponential and constant background.

The 1651-keV transition has a half-life shorter than that of the known 14^+ isomer, its decay curve and fit are presented in Fig. 5.19. The fit to the decay curve of the 1651 keV transition yields a half-life value of 219 ± 55 ns. We therefore conclude that there exists another isomeric state in ^{94}Pd, not observed before through the β-decay of ^{94}Ag, and located above the known 14^+ isomer. The 267-keV, 347-keV and 408-keV lines, which were previously reported as prompt in fusion-evaporation experiments studying the β decay of ^{94}Ag, are present in the γ spectrum of Fig. 5.17, i.e. approximately 475 ns after fragmentation. Their low intensities and the contribution to Compton background from higher energy lines de-exciting the known 14^+ state make it hard to extract a half-life for these lines. However, their intensities are very similar and also consistent with that of the 1651-keV line, thus leading to the conclusion that they originate from the same cascade, above the known $14^+ \rightarrow 0^+$ one.

Following the same procedure as in the case of the ^{96}Ag isomer, coincidences, relative intensities and energy-sum relationships were deduced for the isomeric γ transitions of ^{94}Pd, and the resulting level scheme is presented in Fig. 5.20, which is in agreement with previous works. Placement of the 1651-keV transition in the level scheme is suggested, as part of the γ cascade de-exciting a high-spin μs isomer, located at 7210 keV.
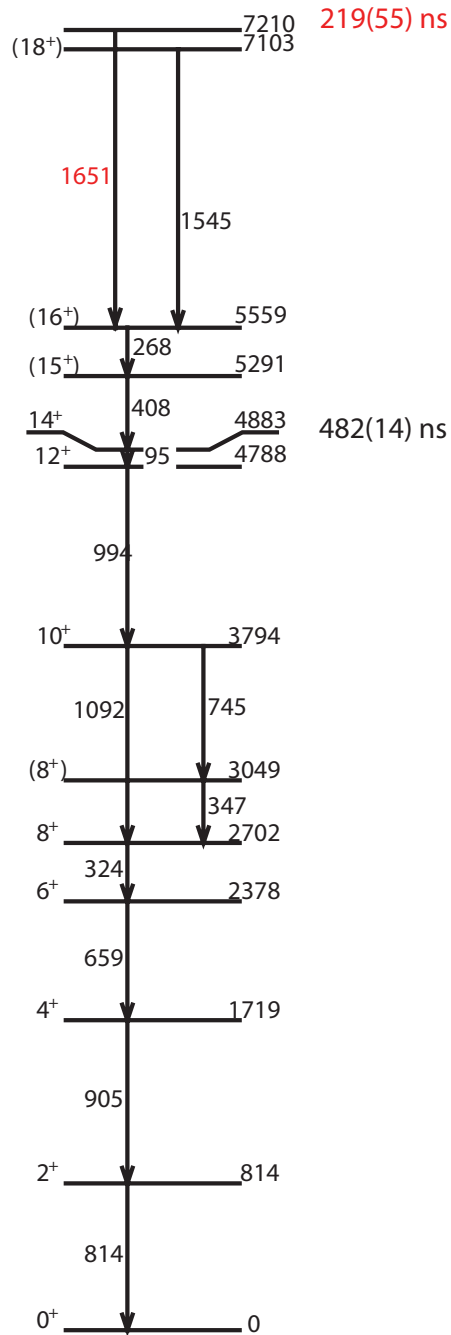
Figure 5.20: Experimental level scheme of ^{94}Pd obtained in this work (only observed transitions are included). Level spin and parity assignments are based on previous results. The 1651-keV transition is new and its placement is suggested, de-exciting a high-spin isomeric state, at 7210 keV, and with a half-life of 219(55) ns.

Chapter 6

Astrophysical Impact

The neutron-deficient nuclei studied in this work are in the path of the astrophysical rp-process. Possible implications of our measurements on the isotopic abundances produced in an rp-process that reaches the ^{100}Sn region were therefore explored by incorporating the new results into a one-zone X-ray burst model. A brief introduction to the reaction network used is presented in this chapter, followed by the results of the calculations performed.

6.1   rp-process reaction network

A single zone X-ray burst model was used to study the impact of our measurements on an rp-process that reaches the $A \approx 100$ region. This model has been used before to explore the mass processing beyond tin to determine for the first time the endpoint of the rp-process [19], and it is based on the physics outlined in Ref. [91]. The network includes 690 proton-rich nuclei, from hydrogen to xenon. The reaction rates used are from ReaclibV1, provided by JINA Reaclib online database [27].

6.2 Impact of our measurements on the rp-process

Presented in figure 6.1 is the rp-process reaction path calculated with our code. The nuclei produced in this experiment are indicated. The goal of this study was to find out whether or not the rp-process could be a viable production mechanism for ^{96}Ru, a p-nuclei observed with high abundance in the solar system (see Sections 1.1 and 1.2.1). Thus, the following discussion focuses on the impact of the measured half-life of ^{96}Cd.

Nuclei with $A = 96$ produced in the rp-process decay into ^{96}Ru at freezeout. Therefore, our calculations were done under the most favorable conditions for production of $A = 96$ nuclei, which were the same used in Ref. [19]. The initial conditions corresponded to a high accretion rate and low metallicity of the accreted matter, which minimizes hydrogen burning in the neutron star prior to burst ignition, and leaves about 66% of the hydrogen for burning during the X-ray burst. During freezeout, the $A = 96$ nuclei produced during the burst as ^{96}Cd are destroyed through proton capture on ^{96}Rh. This destruction rate depends in turn on the freezeout timescale. An instant freezeout was therefore chosen at the time of maximum $A = 96$ production.

6.2.1 The half-life of ^{96}Cd

Nuclei with $A = 96$ are produced during the rp-process due to the accumulation of mass at ^{96}Cd, which is a waiting point [5]. Previous rp-process calculations which included ^{96}Cd had to use a theoretically predicted half-life (ranging from 0.30 [74] to 2.18 seconds [77]). The experimental determination of its half-life was therefore crucial in order to reliably calculate the final composition of the ashes of an X-ray burst that reaches this mass region. The half-life of ^{96}Cd was determined in this work as $1.03^{+0.24}_{-0.21}$ s.

The final rp-process abundance pattern reflects the composition of the ashes of the X-ray burst after the proton captures have ended and the newly formed proton-rich
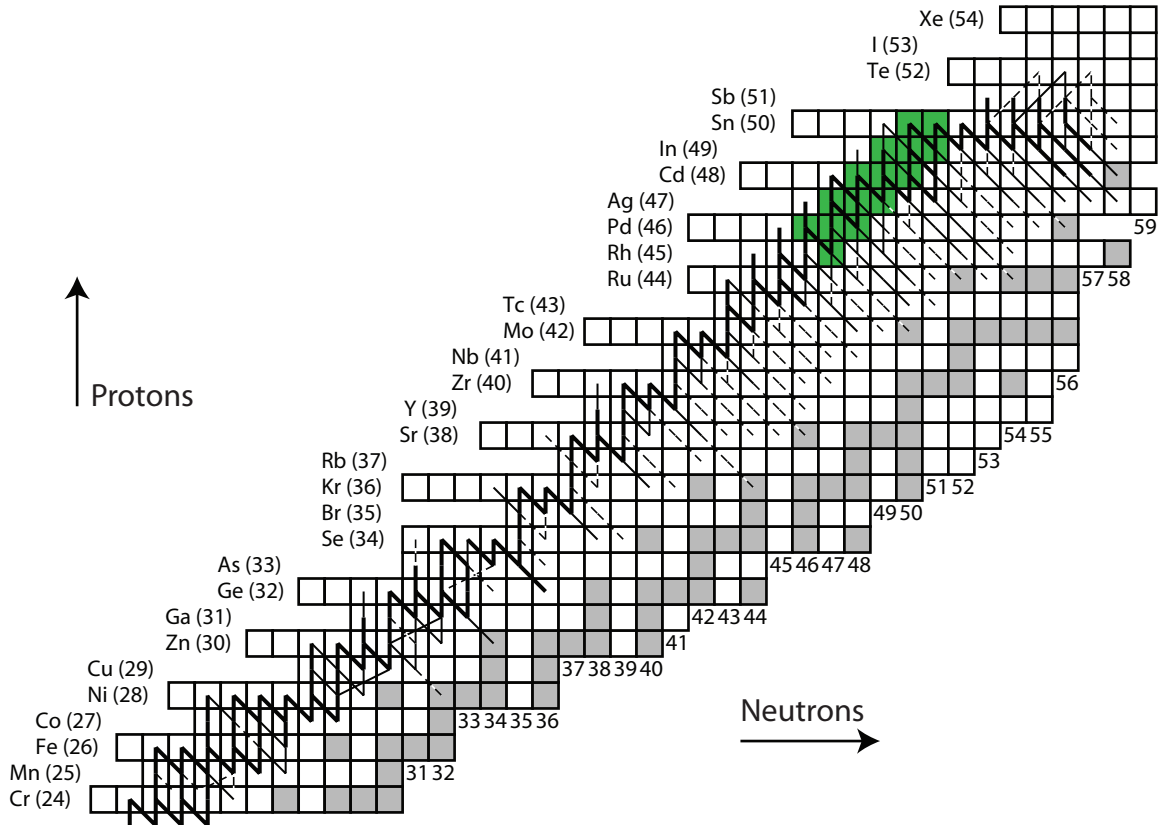
Figure 6.1: The nuclei produced in the present experiment are marked in green.

nuclei had time to decay towards stability. As the most proton-rich stable $A = 96$ isobar, ^{96}Ru is the only one that can be produced by β^+ decays of heavier isobars. Thus, the final abundance of mass $A = 96$ in the rp-process will correspond to that of ^{96}Ru. Fig. 6.2 shows the overproduction factors, defined as the ratio of the mass fraction of an isotope produced in a particular process to its mass fraction in the solar system. The two curves correspond to the minimum and maximum predicted values of the half-life of ^{96}Cd. For the rp-process to be the mechanism responsible for the origin of ^{96}Ru, a large overproduction factor is required for $A = 96$, of the order of 10^{10} [69]. Such a large overproduction factor would be necessary in order to compensate for the small amount of ashes that could be ejected, and the relatively small amount of mass processed by X-ray bursts in our Galaxy [20, 69]. In addition, the overproduction factor must peak significantly higher than for isotopes that are known to be produced in the s-process, such as $A = 97$. Fig. 6.2 shows that with our

Figure 6.2: Predicted overabundances relative to solar as a function of mass number, from rp-process calculations using a ^{96}Cd half-l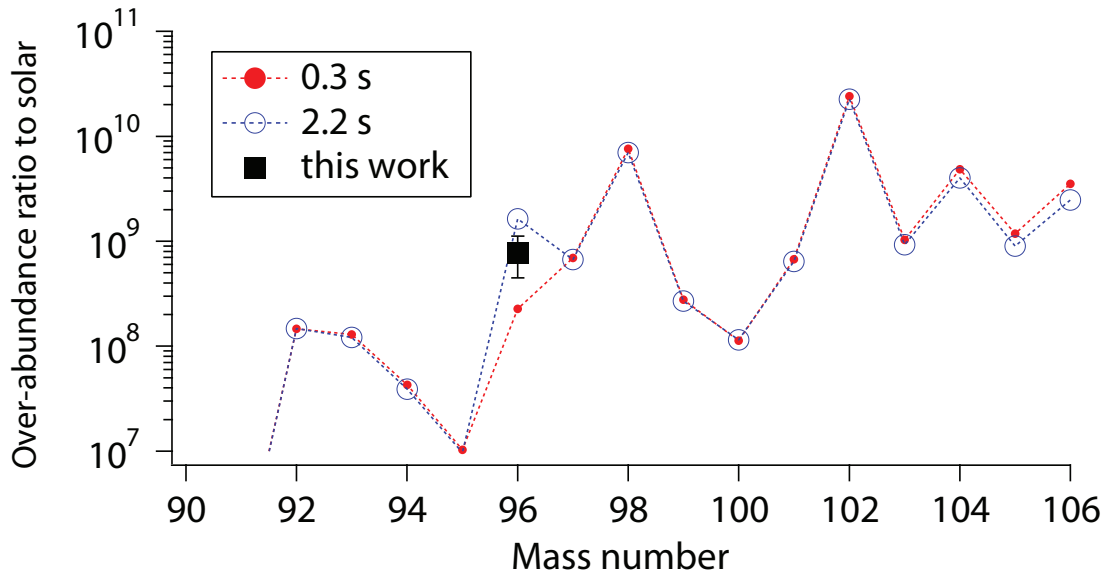ife ranging from 0.3 to 2.2 s, and our measured vale. A pronunced peak at mass 96 would indicate that ^{96}Cd plays a significant role as a waiting point. Figure adapted from [69].

new data such conditions are not met. Therefore, the rp-process can be ruled out as the scenario responsible for production of ^{96}Ru.

Additionally, Fig. 6.3 shows the energy generation as a function of time during an X-ray burst. The two curves correspond to the shortest (0.3 s) and longest (2.2 s) predicted half-lives of ^{96}Cd, respectively. The effect of varying this value is rather small, differences can only be noticed during the cooling phase, the inset shows a zoom-in of the time range where the two calculations differ the most.

6.2.2 The microsecond isomers in ^{96}Ag

During the rp-process freezeout, ^{96}Cd β^+ decays to ^{96}Ag, where the ^{96}Ag(p, γ) reaction rate then governs how many $A = 96$ nuclei survive and how many are converted into heavier nuclei. Isomers may affect proton capture rates significantly by creating a non-thermal population of levels, thus the importance of their identification and characterization. Experimental data on isomers in ^{96}Ag can therefore shed light on the question of the production of mass $A = 96$ in the rp-process.
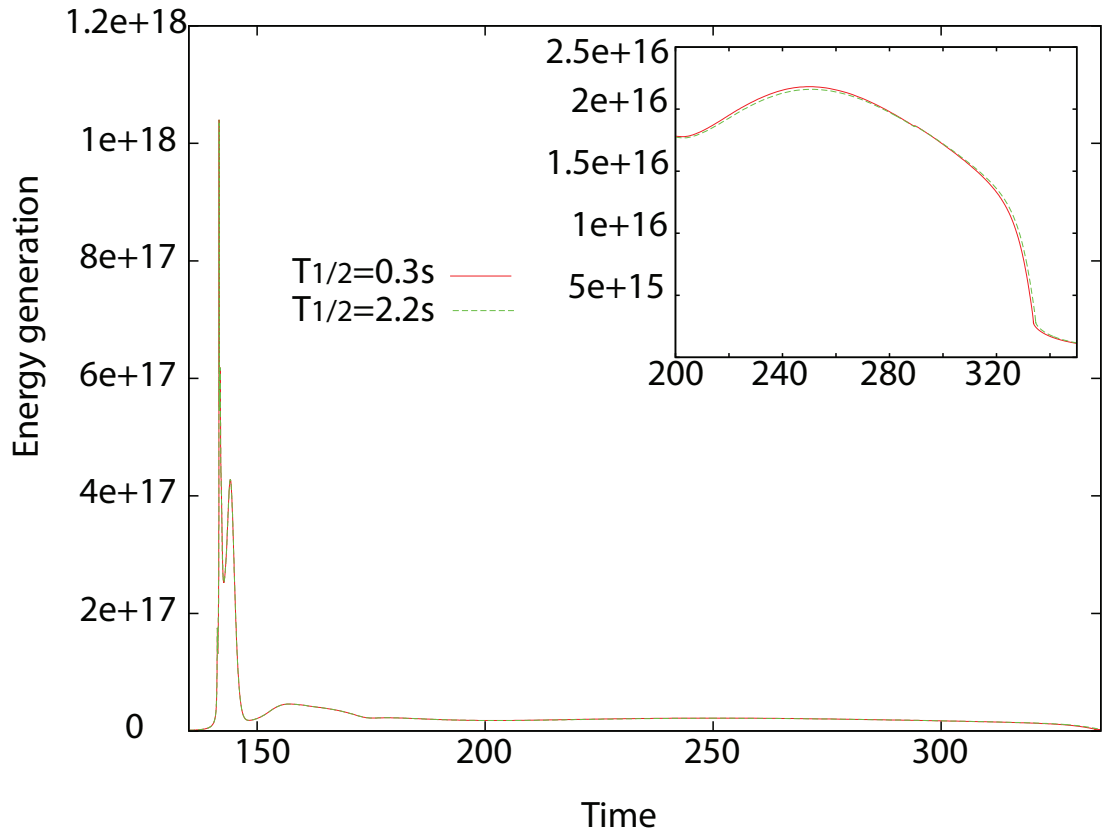
Figure 6.3: Effect of ^{96}Cd half-life in rp-process predicted energy generation as a function of time. The two curves correspond to the shortest and longest half-lives predicted for ^{96}Cd. The inset shows a zoom of the region where the two cureves differ the most.

In this work, a γ-ray cascade was identified from the decay of a 1.45(7) μs isomeric state in ^{96}Ag. Evidence for a second μs isomer, along with the γ-ray transitions associated with its decay, was also found. Its half-life was determined as 8.6(63) μs. The new data show that the microsecond isomers in ^{96}Ag are at excitation energies of at least 2.5 MeV and likely have spins and parities of 15^+ and 13^-, respectively. At such high excitation energies, these states are unlikely to be populated in astrophysical environments by thermal excitation of lower-lying states in ^{96}Ag. The high spin makes population by proton capture on ^{95}Pd (expected ground state $9/2^+$) or by β decay from ^{96}Cd (ground state 0^+) also unlikely. The 15^+ state in ^{96}Ag could be populated by the β decay of the predicted 16^+ isomer in ^{96}Cd, though the existence of this state has not been confirmed by experiment. However, population of that isomer by

proton capture is, again, unlikely because of its high spin. The microsecond isomers characterized in this work are therefore unlikely to play a role in the rp-process.

6.3 Conclusions and Outlook

The development of science and technology over the 20th century to the present day has been vertiginous. We have come to the realization that the elements that make up everything in our planet, including ourselves, are the result of billions of years of nucleosynthesis, taking place in a variety of scenarios, some of them still to be understood, or even, discovered.

One of such nucleosynthesis scenarios was explored in this work: that of the rp-process in Type I X-Ray Bursts occurring in accreting neutron stars. It was proposed as a possible production mechanism of some of the stable nuclides on the proton-rich side of the valley of β stability, such as ^{96}Ru. Our new data ruled out this possibility, indicating that X-ray bursts are not the main source of ^{96}Ru, found so abundantly in the solar system [69]. The mystery therefore remains, and new models will have to be developed in order to explain the nucleosynthesis of ^{96}Ru. Several works on νp-process in Type II Supernovae show that an important contribution to the abundances of light p-nuclei can come from this process. However, the νp-process is very sensitive to the details of the explosion mechanism and mass of the proto-neutron star. The variuos model uncertainties together with nuclear physics uncertainties result in different nucleosynthesis from event to event, and therefore to a lack of consensus between the different studies [8–10] (see also [92] and references therein). In a recent work by Travaglio et $al.$ [93] different models of Type Ia supernovae were analyzed and the different s-process distributions, and their consequences for the p-process explored. They found that a flat s-seed distribution directly translates into a flat p-process distribution with average production factors directly proportional to the adopted level of s-seeds. This demonstrated that p-nuclei can be produced with similar enhancement

factors relative to ^{56}Fe, including the light-p nuclei ^{92,94}Mo and ^{96,98}Ru.

There are still plenty of open questions regarding accreting neutron stars. New and improved nuclear physics measurements will play a crucial role in gaining a better understanding of these phenomena. Our work showed an example of the sensitivity of the X-ray burst energy generation and mass processing to nuclear physics uncertainties. Besides half-lives, masses and particle induced reaction rates of the neutron-deficient nuclei in the rp-process nuclei are needed.

On the nuclear structure side, our measurement contributes to the understanding of the shell structure of $N \approx Z$ nuclei very far from stability. For instance, the comparison of the level scheme determined for ^{96}Ag from our experiment to the shell model predictions indicated that a larger model space was needed in order to correctly reproduce observations. The calculation within the larger $(p_{3/2}p_{1/2}f_{5/2}g_{9/2})$ model space reproduced excitation energies and half-lives of the isomeric states better than the one performed in the limited $(p_{1/2}g_{9/2})$ model space. These results will in turn serve as reference for future experimental and theoretical work.

Bibliography

[1] K. Ogawa. Shell-model calculations of high-spin isomers in neutron-deficient 1g9/2-shell nuclei. *Phys. Rev. C Rapid Communications*, **28**:958, 1983.

[2] T. Rauscher. Origin of the p-nuclei in explosive nucleosynthesis. In *Proceedings of Science. 11th Symposium on Nuclei in the Cosmos*, 2010.

[3] J. Bork, H. Schatz, T. Kappeler, and T. Rauscher. Proton capture cross sections of the ruthenium isotopes. *Phys. Rev. C*, 58:524–535, 1998.

[4] W. Rapp, J. Gorres, M. Wiescher, H. Schatz, and F. Kappeler. Sensitivity of p-process nucleosynthesis to nuclear reaction rates in a 25 solar mass supernova model. *ArXiv*, astro-ph/0608341, 2006.

[5] H. Schatz et al. *Phys. Rep.*, **294**:167, 1998.

[6] M. Hencheck, R. N. Boyd, M. Hellström, D. J. Morrissey, M. J. Balbes, F. R. Chloupek, M. Fauerbach, C. A. Mitchell, R. Pfaff, C. F. Powell, G. Raimann, B. M. Sherrill, M. Steiner, J. Vandegriff, and S. J. Yennello. Identification of new nuclei near the proton drip line. *Phys. Rev. C*, 50(4):2219–2221, Oct 1994.

[7] H. Schatz. Rare isotopes in thermonuclear explosions on neutron stars. *Progress in Particle and Nuclear Physics*, 66:277–282, 2011.

[8] C. Fröhlich, G. Martínez-Pinedo, M. Liebendörfer, F.-K. Thielemann, E. Bravo, W. R. Hix, K. Langanke, and N. T. Zinner. Neutrino-induced nucleosynthesis of a>64 nuclei: The νp process. *Phys. Rev. Lett.*, 96(14):142502, Apr 2006.

[9] J. Pruet et al. Nucleosynthesis in the early supernova winds ii. the role of neutrinos. *The Astrophysical Journal*, 644:1028, 2006.

[10] S. Wanajo. The rp-process in neutrino-driven winds. *The Astrophysical Journal*, 647:1323, 2006.

[11] J. Grindlay et al. *Astrophysical Journal*, 205:L127, 1976.

[12] R. D. Belian, J. P. Conner, and W. D. Evans. *Astrophysical Journal*, 206:L135, 1976.

[13] H. Schatz and K. E. Rehm. X-ray binaries. *Nucl. Phys. A*, 777:601, 2006.

[14] A. Steiner, J. Lattimer, and E. Brown. The equation of state from observed masses and radii of neutron stars. *The Astrophysical Journal*, 722:33–54, 2010.

[15] C. Iliadis. *Nuclear Physics of Stars*. WILEY-VCH, 2007.

[16] H. Schatz. The importance of nuclear masses in the astrophysical rp-process. *International Journal of Mass Spectrometry*, 251:293–299, 2006.

[17] D. Galloway et al. Thermonuclear (type i) x-ray bursts observed by the rossi x-ray timing explorer. *The Astrophysical Journal Supplement Series*, 179:360–422, 2008.

[18] H. Schatz. Radioactive nuclei on accreting neutron stars. *Nucl. Phys. A*, 746:347c–353c, 2004.

[19] H. Schatz et al. End point of the rp-process on accreting neutron stars. *Phys. Rev. Lett.*, **86**:3471, 2001.

[20] N. Weinberg, L. Bildsten, and H. Schatz. Exposing the nuclear burning ashes of radius expansion type i x-ray bursts. *The Astrophysical Journal*, 639:1018–1032, 2006.

[21] R. Wallace and S. Woosley. *Astrophysical Journal Suppl.*, 45:389, 1981.

[22] M.Y. Fujimoto, M. Sztajno, W. H. G. Lewin, and J. van Paradijs. *Astrophysical Journal*, 319:902, 1987.

[23] T. Hanawa, D. Sugimoto, and M.-A. Hashimoto. *Publ. Astron. Soc. Jpn.*, 35:491, 1983.

[24] L. Van Wormer et al. *Astrophysical Journal*, 432:326, 1994.

[25] O. Koike, M. Hashimoto, K. Arai, and S. Wanajo. *Astron. Astrophys.*, 342:464, 1999.

[26] R. Wallace and S. Woosley. *High Energy Transients in Astrophysics*. Number 115. AIP Conference Proceedngs, 1984.

[27] R. Cyburt et al. The jina reaclib database: its recent updates and impact on type-i x-ray bursts. *The Astrophysical Journal Supplement Series*, 189:240–252, 2010.

[28] V. Elomaa et al. Quenching of the snsbte cycle in the rp-process. *Phys. Rev. Lett.*, 102:252501, 2009.

[29] S. Gupta, S. Brown, H. Schatz, P. Moller, and K.L. Kratz. Heating in the accreted neutron star ocean: implications for superburst ignition. *Ap.J.*, 662:1188, 2007.

[30] E. Brown. Nuclear heating and melted layers in the inner crust of an accreting neutron star. *Ap. J.*, 531:998, 2000.

[31] E. F Brown, Bildsten L., and R. E. Rutledge. *Astrophysical Journal*, 504:L95, 1998.

[32] F. zel. Soft equations of state for neutron-star matter ruled out by exo 0748 - 676. *Nature*, 441:1115–1117, 2006.

[33] F. zel and D. Psaltis. Reconstructing the neutron-star equation of state from astrophysical measurements. *arXiv*, arXiv:0905.1959v2, 2010.

[34] J. J. M. in 't Zand and N. Weinberg. Evidence of heavy-element ashes in thermonuclear x-ray bursts with photospheric superexpansion. *Astronomy & Astrophysics*, page 13952, 2010.

[35] B. A. Brown. *International School of Heavy-Ion Physics, 4th Course: Exotic Nuclei.* (World Scientific, Singapore), 1998. edited by R. A. Broglia and P. G. Hansen.

[36] B. A. Brown. The nuclear shell model towards the drip lines. *Progress in Particle and Nuclear Physics*, 47:517, 2001.

[37] S. Harissopulos et al. β decay of ^{95}ag. *Phys. Rev. C*, 72:024303, 2005.

[38] R. Grzywacz, R. Anne, G. Auger, C. Borcea, J. M. Corre, T. Dörfler, A. Fomichov, S. Grevy, H. Grawe, D. Guillemaud-Mueller, M. Huyse, Z. Janas, H. Keller, M. Lewitowicz, S. Lukyanov, A. C. Mueller, N. Orr, A. Ostrowski, Yu. Penionzhkevich, A. Piechaczek, F. Pougheon, K. Rykaczewski, M.G. Saint-Laurent, W. D. Schmidt-Ott, O. Sorlin, J. Szerypo, O. Tarasov, J. Wauters, and J. Żylicz. New μs isomers in t_z=1 nuclei produced in the ^{112}sn(63a mev)+^{nat}ni reaction. *Phys. Rev. C*, 55(3):1126–1129, Mar 1997.

[39] L. Batist et al. Isomerism in 96ag and non-yrast levels in 96pd and 95rh, studied in beta decay. *Nuclear Physics A*, 720:245–273, 2003.

[40] J. Doring et al. *Phys. Rev. C*, 68:034306, 2003.

[41] A. Blazhev et al. Observation of a core-excited e4 isomer in 98cd. *Phys. Rev. C*, 69:064304, 2004.

[42] K. Kaneko et al. Structure of upper-$g_{9/2}$-shell nuclei and shape effect in the ^{94}ag isomeric states. *Phys. Rev. C*, 77(6):064304, Jun 2008.

[43] C. Plettner et al. *Nucl. Phys. A*, 733:20–36, 2004.

[44] I. Mukha et al. β-delayed proton decay of a high-spin isomer in ^{94}ag. *Phys. Rev. C*, 70(4):044311, Oct 2004.

[45] K. Schmidt et al. *Z. Phys. A*, 350:99, 1994.

[46] T. S. Brock, B. S. Nara Singh, P. Boutachkov, N. Braun, A. Blazhev, Z. Liu, R. Wadsworth, M. Górska, H. Grawe, S. Pietri, C. Domingo-Pardo, D. Rudolph, S. J. Steer, A. Ataç, L. Bettermann, L. Cáceres, T. Engert, K. Eppinger, T. Faestermann, F. Farinon, F. Finke, K. Geibel, J. Gerl, R. Gernhäuser, N. Goel, A. Gottardo, J. Grebosz, C. Hinke, R. Hoischen, G. Ilie, H. Iwasaki, J. Jolie, A. Kaşkaş, I. Kojuharov, R. Krücken, N. Kurz, E. Merchán, C. Nociforo, J. Nyberg, M. Pfützner, A. Prochazka, Zs. Podolyák, P. H. Regan, P. Reiter, S. Rinta-Antila, H. Schaffner, C. Scholl, P.-A. Söderström, N. Warr, H. Weick, H.-J. Wollersheim, and P. J. Woods. Observation of a new high-spin isomer in ^{94}pd. *Phys. Rev. C*, 82(6):061309, Dec 2010.

[47] Kenneth S. Krane. *Introductory Nuclear Physics*. John Wiley & Sons, Inc., New York, 1988.

[48] S. S. M. Wong. *Introductory Nuclear Physics*. John Wiley & Sons, Inc., New York, 1998.

[49] P. M. Walker and G.D. Dracoulis. *Nature*, 399:35, 1999.

[50] K. Schmidt et al. Decay properties of very neutron-deficient isotopes of silver and cadmium. *Nucl. Phys. A*, 624:185–209, 1997.

[51] N. Mărginean et al. Yrast isomers in ^{95}ag, ^{95}pd, and ^{94}pd. *Phys. Rev. C*, 67(6):061301, Jun 2003.

[52] M. La Commara et al. Beta decay of medium and high spin isomers in ^{94}ag. *Nuclear Physics A*, 708(3-4):167 – 180, 2002.

[53] G. Lorusso, A. Becerril, A. Amthor, et al. Half-lives of ground and isomeric states in 97cd and the astrophysical origin of 96ru. *Physics Letters B*, 699:141–144, 2011.

[54] D. J. Morrissey, B. M. Sherrill, M. Steiner, A. Stolz, and I. Wiedenhoever. Commissioning the a1900 projectile fragment separator. *Nuclear Instruments and Methods in Physics Research Section B: Beam Interactions with Materials and Atoms*, 204:90 – 96, 2003. 14th International Conference on Electromagnetic Isotope Separators and Techniques Related to their Applications.

[55] D. Bazin et al. *Nuclear Instruments and Methods A*, **606**:314, 2009.

[56] D. Morrissey and B. M. Sherrill. Radioactive nuclear beam facilities based on projectile fragmentation. *Phil. Trans. R. Soc. Lon. A*, 356:1985–2006, 1998.

[57] John W. Wilson, Lawrence W. Townsend, and F.F. Badavi. A semiempirical nuclear fragmentation model. *Nuclear Instruments and Methods in Physics Research Section B: Beam Interactions with Materials and Atoms*, 18(1-6):225 – 231, 1986.

[58] G. Loveland, W. Morrissey D. W. Seaborg. *Modern Nuclear Chemistry*. Wiley, 2006.

[59] A. Stolz, T. Baumann, T.N. Ginter, D.J. Morrissey, M. Portillo, B.M. Sherrill, M. Steiner, and J.W. Stetson. Production of rare isotope beams with the nscl fragment separator. *Nuclear Instruments and Methods in Physics Research Section B: Beam Interactions with Materials and Atoms*, 241(1-4):858 – 861, 2005. The Application of Accelerators in Research and Industry - Proceedings of the Eighteenth International Conference on the Application of Accelerators in Research and Industry (CAARI 2004).

[60] O.B. Tarasov and D. Bazin. Lise++ : design your own spectrometer. *Nuclear Physics A*, 746:411 – 414, 2004. Proceedings of the Sixth International Conference on Radioactive Nuclear Beams (RNB6).

[61] K. Yamada, T. Motobayashi, and I. Tanihata. Rf deflector system for proton-rich ri beams in riken. *Nuclear Physics A*, 746:156 – 160, 2004. Proceedings of the Sixth International Conference on Radioactive Nuclear Beams (RNB6).

[62] *Status Report on the NSCL RFFS*, 2007.

[63] J. I. Prisciandaro, A. C. Morton, and P. F. Mantica. Beta counting system for fast fragmentation beams. *Nuclear Instruments and Methods in Physics Research Section A: Accelerators, Spectrometers, Detectors and Associated Equipment*, 505(1-2):140 – 143, 2003. Proceedings of the tenth Symposium on Radiation Measurements and Applications.

[64] W. F. Mueller, T. Glasmacher, D. Gutknecht, G. Hackman, P. G. Hansen, Z. Hu, K. L. Miller, and P. Quirin. *Nucl. Instr. and Meth. A*, **466**:492, 2001.

[65] Jurgen Theuerkauf. *Die Analyse von zwei- und mehrdimensionalen gamma-gamma Koinzidenzspektren an Beispielen aus Hochspinexperimenten in der Massengegend um 146Gd*. PhD thesis, Universitat zu Koln, 1994.

[66] J. Schneider, J. Friese, J. Reinhold, K. Zeitelhack, Faestermann T., R. Gernhäuser, H. Gilg, G. Heine, J. Homolka, P. Kienle, H. Korner, H. Geissel, G. Munzenberg, and K. Summerer. Production and identification of ^{100}sn. *Z. Phys. A*, 348:241–242, 1994.

[67] M. Lewitowicz et al. *Nucl. Phys. A*, 583:857, 1995.

[68] A. Stolz et al. Projectile fragmentation of 112sn at elab=1 a gev. *Phys. Rev. C*, 65:064603, 2002.

[69] D. Bazin, F. Montes, A. Becerril, G. Lorusso, A. Amthor, T. Baumann, H. Crawford, A. Estrade, A. Gade, T. Ginter, C. J. Guess, M. Hausmann, G. W. Hitt, P. Mantica, M. Matos, R. Meharchand, K. Minamisono, G. Perdikakis, J. Pereira, J. Pinter, M. Portillo, H. Schatz, K. Smith, J. Stoker, A. Stolz, and R. G. T. Zegers. Production and β decay of rp-process nuclei $cd96$, $in98$, and $sn100$. *Phys. Rev. Lett.*, 101(25):252501, Dec 2008.

[70] J. M. Daugas et al. Interplay between angular momentum transfer and nuclear structure in the production of isomers at intermediate energies. *Phys. Rev. C*, 63:064609, 2001.

[71] A. Stolz. A method of maximum likelihood for analyzing half-lives. 2002.

[72] G. F. Knoll. *Radiation Detection and Measurement.* John Wiley & Sons, Inc., New York, 2000.

[73] P. Kienle et al. Synthesis and halflives of heavy nuclei relevant for the rp-process. *Progress in Particle and Nuclear Physics*, 46:73–78, 2001.

[74] K. Takahashi et al. *At. Data and Nucl. Data Tables*, **12**:101, 1973.

[75] G. T. Biehle and P. Vogel. *Phys. Rev. C*, 46:1555, 1992.

[76] P. Moller et al. *At. Dat. Nucl. Dat. Tables*, 66:131, 1997.

[77] H. Herndl and B. A. Brown. Shell-model calculations for the properties of nuclei with a = 86-100 near the proton drip line. *Nuclear Physics A*, 627(1):35 – 52, 1997.

[78] T. Faestermann et al. *Eur. Phys. J. A*, 15:185, 2002.

[79] M. Lewitowicz et al. *Phys. Lett. B*, 332:20, 1994.

[80] K. Summerer et al. *Nucl. Phys. A*, 616:641, 1997.

[81] Kurcewicz et al. *Z. Phys. A*, **308**:21, 1982.

[82] R. Gross and A. Frenkel. Effective interaction of protons and neutrons in the 2p1/2 - 1g9/2 subshells. *Nuclear Physics A*, 267:85–108, 1976.

[83] A. Becerril et al. *Submitted to Phys. Rev. C*, 2011.

[84] B. Cheal et al. *Phys. Rev. Lett.*, 104:252502, 2010.

[85] D. Verney et al. *Phys. Rev. C*, 76:054312, 2007.

[86] K. T. Flanagan et al. *Phys. Rev. C*, 82:041302 (R), 2010.

[87] Vingerhoets et al. *Phys. Rev. C*, 82:064311, 2010.

[88] B. A. Brown et al. Search for parity mixing in the $^{(93)}$tc 17/2- isomer: Measurements of partial gamma decay widths. *Nucl. Phys. A*, 306:242, 1978.

[89] M. Gorska et al. *Z. Phys. A.*, 353:233, 1995.

[90] A. B. Garnsworthy et al. *Phys. Rev. C*, 80:064303, 2009.

[91] L. Bildsten. Thermonuclear burning on rapidly accreting neutron stars. In R. Buccheri et al., editors, *The Many Faces of Neutron Stars*, pages 419–449. Kluwer Academic Publishers, 1998.

[92] J. Jose and C. Iliadis. Nuclear astrophysics: the unfinished quest for the origin of the elements. *arXiv*, 1107.2234v1, 2011.

[93] C. Travaglio, F. Ropke, R. Gallino, and W. Hillebrandt. Type ia supernovae as sites of p-process: two-dimensional models coupled to nucleosynthesis. *arXiv*, 1106.0582v1, 2011.